

# Off-Yrast low-spin structure of deformed nuclei at mass number $A \approx 150$



Vom Fachbereich Physik  
der Technischen Universität Darmstadt

zur Erlangung des Grades  
eines Doktors der Naturwissenschaften  
(Dr. rer. nat.)

genehmigte

## **D i s s e r t a t i o n**

angefertigt von

Andreas Krugmann, M. Sc.  
aus Heppenheim a.d. Bergstraße

Referent: Professor Dr. Dr. h.c. Norbert Pietralla  
Korreferent: Professor Dr. Peter von Neumann-Cosel

Tag der Einreichung: 17.06.2014  
Tag der Prüfung: 14.07.2014

Darmstadt 2014  
D 17



---

# Off-Yrast low-spin structure of deformed nuclei at mass number $A \approx 150$

---

**Off-Yrast niedrig-Spin Struktur deformierter Atomkerne mit Massenzahl  $A \approx 150$**   
Zur Erlangung des Grades eines Doktors der Naturwissenschaften (Dr. rer. nat.)  
genehmigte Dissertation von Andreas Krugmann, M. Sc. aus Heppenheim a. d. Bergstraße  
Dezember 2014 – Darmstadt – D 17



TECHNISCHE  
UNIVERSITÄT  
DARMSTADT

Fachbereich Physik  
Institut für Kernphysik



Supported by the DFG through SFB 634 and NE 679/3-1.

---

Off-Yrast low-spin structure of deformed nuclei at mass number  $A \approx 150$   
Off-Yrast niedrig-Spin Struktur deformierter Atomkerne mit Massenzahl  $A \approx 150$

Genehmigte Dissertation von Andreas Krugmann, M. Sc. aus Heppenheim a. d. Bergstraße

1. Gutachten: Professor Dr. Dr. h.c. Norbert Pietralla
2. Gutachten: Professor Dr. Peter von Neumann-Cosel

Tag der Einreichung: 17. Juni 2014

Tag der Prüfung: 14. Juli 2014

Darmstadt – D 17

Bitte zitieren Sie dieses Dokument als:

URN: urn:nbn:de:tuda-tuprints-42393

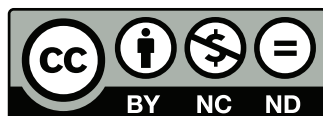
URL: <http://tuprints.ulb.tu-darmstadt.de/4239>

Dieses Dokument wird bereitgestellt von tuprints,

E-Publishing-Service der TU Darmstadt

<http://tuprints.ulb.tu-darmstadt.de>

[tuprints@ulb.tu-darmstadt.de](mailto:tuprints@ulb.tu-darmstadt.de)



Die Veröffentlichung steht unter folgender Creative Commons Lizenz:

Namensnennung – Keine kommerzielle Nutzung – Keine Bearbeitung 2.0 Deutschland

<http://creativecommons.org/licenses/by-nc-nd/2.0/de/>

---

*It doesn't matter how beautiful your theory is,  
it doesn't matter how smart you are.  
If it doesn't agree with experiment,  
it's wrong.*

Richard Feynman

*Viel Gerede bringt es nicht,  
nur das Messen bringt's ans Licht!*

Achim Richter

---



---

## Zusammenfassung

---

Die vorliegende Arbeit gliedert sich in zwei Teile. Der erste Teil behandelt die Untersuchung des  $0_1^+ \rightarrow 0_2^+$  Übergangs in  $^{150}\text{Nd}$  in einem Elektronenstreuexperiment und der zweite Teil beschäftigt sich mit einem Protonenstreuexperiment am  $^{154}\text{Sm}$ , wo Dipolanregungen studiert wurden.

Im ersten Teil wird ein Pionierexperiment der Elektronenstreuung vorgestellt. Bei einer Einschussenergie von 75 MeV wurden am hochauflösenden  $169^\circ$  Spektrometer des S-DALINAC, Anregungsspektren bei unterschiedlichen Winkeln aufgenommen. Ziel dieser Untersuchung war die Bestimmung der  $\rho^2(E0; 0_1^+ \rightarrow 0_2^+)$  Übergangsstärke des schweren deformierten Kerns  $^{150}\text{Nd}$ . Der experimentell ermittelte Formfaktor dieses Übergangs wurde mit einem theoretischen Formfaktor verglichen, der aus einem effektiven Dichteoperator auf mikroskopischem Level mit Hilfe der Generator-Coordinate-Methode konstruiert wurde. Die kollektiven Wellenfunktionen, die dazu benötigt wurden, wurden aus dem Confined  $\beta$ -soft Rotor Modell entnommen. In dieser modellabhängigen Analyse wurde zum ersten mal die  $E0$ -Übergangsstärke des  $0_1^+ \rightarrow 0_2^+$  Übergangs in  $^{150}\text{Nd}$  bestimmt.

Des weiteren wurde der Verlauf der  $E0$  Übergangsstärke als Funktion der Potentialsteifigkeit auf dem Weg vom X(5) Phasenübergangspunkt zum Limit des starren Rotors untersucht. Hierbei wurde gezeigt, dass die  $E0$  Stärke am Phasenübergangspunkt sehr hoch ist und mit steigender Potenzialsteifigkeit immer mehr abnimmt und schließlich im Grenzfall des starren Rotors verschwindet. In einer abschließenden theoretischen Betrachtung wurden die Wellenfunktionen des makroskopisch kollektiven Confined  $\beta$ -soft Rotor Modells mit denen aus einem mikroskopischen relativistischen Meanfield Modell verglichen und eine starke Übereinstimmung gefunden.

Der zweite Teil der Arbeit behandelt ein Protonenstreuexperiment mit polarisierten Protonen am ebenfalls schweren deformierten Kern  $^{154}\text{Sm}$ , welches am RCNP in Osaka (Japan) durchgeführt wurde. Mittels der Methode der Polarisationstransferobservablen konnte eine Trennung des Spin-Flip Anteils und des Nicht-Spinflip Anteils vom gesamten Wirkungsquerschnitt vorgenommen werden. Im Falle der elektrischen Dipolstärke konnte zum ersten Mal die Pygmy Dipol Resonanz im schweren deformierten Kern  $^{154}\text{Sm}$  identifiziert werden. Eine Doppelstruktur wurde beobachtet. Als mögliche Interpretation wird eine Deformationsaufspaltung analog zur Dipol Riesenresonanz gegeben. Im Falle der magnetischen Stärke wurde eine breite Verteilung im Anregungsenergiebereich zwischen 6 und 12 MeV gefunden. Die Verteilung und auch die extrahierte Summenstärke sind in sehr guter Übereinstimmung mit vorherigen Experimenten.





---

## Abstract

---

The present work consists of two independent parts. The first part deals with the investigation of the  $0_1^+ \rightarrow 0_2^+$  transition in  $^{150}\text{Nd}$  with inelastic electron scattering and in the second part a proton scattering experiment for the investigation of dipole excitations is presented.

In the first part of this thesis a pioneer experiment in inelastic electron scattering is introduced. At an electron energy of 75 MeV, excitation energy spectra have been measured at the high resolution  $169^\circ$  spectrometer at the S-DALINAC. The aim of this investigation was the determination of the  $\rho^2(E0; 0_1^+ \rightarrow 0_2^+)$  transition strength in the heavy deformed nucleus  $^{150}\text{Nd}$ . The experimental form factor of this particular transition has been compared to a theoretical form factor that has been constructed by an effective density operator on a microscopic level with the help of the generator coordinate method. The required collective wave functions have been calculated in the Confined  $\beta$  soft rotor model. In this model-dependent analysis the  $E0$  transition strength has been determined for the first time. Furthermore the evolution of the  $E0$  transition strength as a function of the potential stiffness has been investigated from the X(5) phase shape transitional point to the Rigid Rotor limit. It has been shown, that the  $E0$  strength is relatively high at the shape-phase transitional point and starts to decrease with increasing stiffness and vanishes completely at the Rigid Rotor limit. Additionally the wave functions of the macroscopic collective Confined  $\beta$ -soft rotor model have been compared to those from a microscopic mean field Hamiltonian. Good agreement has been found.

The second part of this thesis covers a polarized-proton scattering experiment on the heavy deformed nucleus  $^{154}\text{Sm}$ , that has been performed at the RCNP in Osaka, Japan. Utilizing the method of polarization transfer observables, a separation of spinflip and non-spinflip parts of the cross section has been done. Here, for the first time, the Pygmy Dipole Resonance (PDR) has been identified in the heavy deformed nucleus  $^{154}\text{Sm}$  that appears as a double-hump structure in the  $E1$  response. A possible interpretation of this double-hump structure in terms of a deformation splitting analogously to the Giant Dipole Resonance (GDR) has been given. In case of the spinflip cross section, a broad distribution in the excitation energy range between 6 and 12 MeV has been observed. The distribution and the extracted sum strength are in good accordance with previous experiments.



---

## Contents

---

<b>Preface - Off Yrast excitations in scattering experiments with charged particles</b>	<b>1</b>
<b>I. Electric monopole strength of the <math>0_1^+ \rightarrow 0_2^+</math> transition in <math>^{150}\text{Nd}</math></b>	<b>3</b>
<b>1. Introduction</b>	<b>5</b>
<b>2. Theoretical background</b>	<b>11</b>
2.1. Collective coordinates . . . . .	11
2.2. The collective Bohr Hamiltonian . . . . .	13
2.2.1. E0 transitions in quadrupole collective models . . . . .	13
2.2.2. Derivation of $\rho^2(E0)$ transition strength as a function of potential stiffness	15
2.3. The confined $\beta$ -soft rotor model . . . . .	15
2.3.1. E0 transition strengths in the CBS model . . . . .	18
2.4. Microscopic relativistic mean-field approach . . . . .	19
<b>3. Inelastic electron scattering at low momentum transfer</b>	<b>23</b>
3.1. Electron scattering formalism . . . . .	23
3.2. Model predictions for the $0_1^+ \rightarrow 0_2^+$ E0 transition in $^{150}\text{Nd}$ . . . . .	25
3.2.1. Effective operator for the E0 transition density . . . . .	25
3.2.2. Neutron and proton transition densities . . . . .	26
3.2.3. Predicted DWBA form factors for the electron scattering experiment . . . . .	27
<b>4. Inelastic electron scattering experiments at the S-DALINAC</b>	<b>29</b>
4.1. S-DALINAC and experimental facilities . . . . .	29
4.2. High resolution electron scattering . . . . .	31
4.3. Focal plane detector system . . . . .	32
4.4. Modes of operation . . . . .	34
4.4.1. Dispersive mode . . . . .	34
4.4.2. Energy-loss mode . . . . .	34
4.5. $^{150}\text{Nd}(e,e')$ experiment . . . . .	35
<b>5. Data analysis of the electron scattering data</b>	<b>37</b>
5.1. Line shapes . . . . .	37
5.2. Energy calibration of the excitation spectra . . . . .	37

5.3. Experimental cross sections . . . . .	38
5.3.1. Radiative corrections . . . . .	39
5.3.2. Dead time correction . . . . .	40
5.4. Estimation of uncertainties . . . . .	41
5.5. Experimental Data . . . . .	41
<b>6. Discussion of the electron scattering data</b>	<b>43</b>
6.1. Elastic scattering . . . . .	43
6.2. Electric monopole strength of the $0_1^+ \rightarrow 0_2^+$ transition in $^{150}\text{Nd}$ . . . . .	43
6.3. Evolution of absolute E0 strengths . . . . .	44
6.3.1. Stiffness dependence of the $\rho^2(E0)$ transition strengths . . . . .	46
<b>7. Comparison of the CBS rotor model with a macroscopic collective mean field Hamiltonian for <math>^{150,152}\text{Nd}</math></b>	<b>49</b>
7.1. Description of K=0 bands and their centrifugal stretching . . . . .	49
7.2. Comparison of the collective wave functions . . . . .	51
<b>8. Conclusion and Outlook</b>	<b>55</b>
<b>II. Low-energy dipole strength in <math>^{154}\text{Sm}</math></b>	<b>57</b>
<b>9. Introduction</b>	<b>59</b>
9.1. Electric Resonances . . . . .	59
9.2. Magnetic Resonances . . . . .	61
9.3. Separation of $E1$ and $M1$ : New experimental approaches . . . . .	63
9.4. Outline . . . . .	63
<b>10. Theoretical background for polarized proton scattering at <math>0^\circ</math></b>	<b>65</b>
10.1. Inelastic proton scattering . . . . .	65
10.2. Lippmann-Schwinger equation . . . . .	65
10.3. Distorted waves . . . . .	66
10.4. Optical potential . . . . .	67
10.5. Effective nucleon-nucleus interaction . . . . .	67
10.6. Coulomb excitation . . . . .	69
10.6.1. Classical Coulomb excitations . . . . .	69
10.6.2. Semiclassical coulomb excitations . . . . .	70
10.6.3. Equivalent virtual photon method . . . . .	72
10.6.4. Eikonal description of Coulomb excitation . . . . .	73

10.7. Magnetic dipole transitions and $B(M1_{\sigma\tau})$ from (p,p') cross section data . . . . .	75
10.8. Polarization transfer observables (PT observables) . . . . .	77
<b>11. Polarized proton scattering experiment at RCNP</b>	<b>81</b>
11.1. Beam line polarimeters (BLPs) . . . . .	82
11.2. The setup for $0^\circ$ measurements . . . . .	82
11.2.1. The Grand Raiden spectrometer . . . . .	82
11.3. The Large Acceptance Spectrometer (LAS) . . . . .	84
11.4. Detector systems at the $0^\circ$ scattering facility . . . . .	85
11.4.1. The Focal Plane Detector System . . . . .	85
11.4.2. The Focal Plane Polarimeter (FPP) . . . . .	86
11.5. Experimental conditions . . . . .	87
11.6. Used targets . . . . .	88
11.6.1. The under-focus mode . . . . .	89
11.6.2. The Faraday cups . . . . .	90
11.6.3. The sieve-slit measurements . . . . .	90
<b>12. Data analysis for proton scattering</b>	<b>93</b>
12.1. Data reduction . . . . .	93
12.1.1. Drift time to distance conversion . . . . .	93
12.1.2. Efficiency determination of the VDCs . . . . .	94
12.1.3. Sieve slit analysis . . . . .	96
12.1.4. Higher order aberration corrections . . . . .	97
12.1.5. Excitation energy calibration . . . . .	99
12.1.6. Background subtraction . . . . .	101
12.1.7. Double differential cross sections . . . . .	104
12.2. Polarization transfer analysis . . . . .	106
12.2.1. Method for extracting PT observables: The Estimator Method . . . . .	107
12.3. Results of the polarization transfer analysis . . . . .	109
12.3.1. Results for $^{26}\text{Mg}$ . . . . .	109
12.3.2. Results for $^{154}\text{Sm}$ . . . . .	110
12.4. Electric dipole response in $^{154}\text{Sm}$ . . . . .	112
12.4.1. Photoabsorption Cross section . . . . .	113
12.4.2. $B(E1)$ strength distribution . . . . .	114
12.4.3. Deformation splitting . . . . .	114
12.5. Discussion of angular distributions . . . . .	115
12.6. Determination of the spinflip-M1 strength distribution with the unit-cross section method . . . . .	117

---

<b>13. Conclusion and Outlook</b>	<b>121</b>
<b>A. Derivation of <math>\rho^2(E0)</math> transition strength as a function of potential stiffness</b>	<b>123</b>
<b>B. List of <math>\rho^2(E0)</math> transition strengths compared in figure 6.5</b>	<b>127</b>
<b>Bibliography</b>	<b>138</b>
<b>Danksagung</b>	<b>140</b>
<b>Lebenslauf</b>	<b>141</b>
<b>Eigene Publikationen</b>	<b>144</b>
<b>Eigenständigkeitserklärung</b>	<b>145</b>

---

## List of Figures

---

0.1.	Characteristic response of an atomic nucleus as a function of the excitation energy $E_x$ and the momentum transfer $q$ . . . . .	2
1.1.	Evolution of the potential as a function of the deformation variable $\beta$ in the shape phase transitional area. . . . .	5
1.2.	CBS square well potentials compared to relativistic mean field potentials for $^{150}\text{Nd}$ and $^{152}\text{Nd}$ , respectively. . . . .	6
1.3.	Empirical $\rho^2(E0; 0_2^+ \rightarrow 0_1^+)$ values for nuclei in the A=100 and 150 transition regions. . . . .	7
1.4.	Calculated monopole transition strength $\rho^2(E0; 0_2^+ \rightarrow 0_1^+)$ as a function of neutron number N in the Nd isotopes within the framework of the relativistic mean field. . . . .	8
2.1.	Shape of a spherical nucleus with $\beta=0$ and $\gamma=0$ . . . . .	12
2.2.	Shape of an axial prolate deformed nucleus with $\beta=0.3$ and $\gamma=0$ . . . . .	12
2.3.	Shape of a triaxial deformed nucleus with $\beta=0.3$ and $\gamma=\pi/3$ . . . . .	12
2.4.	X(5) potential as a function of the deformation parameter $\beta$ . . . . .	17
2.5.	CBS potential as a function of the deformation parameter $\beta$ . . . . .	17
3.1.	Calculated proton and neutron transition densities for the $0_1^+ \rightarrow 0_2^+$ transition in $^{150}\text{Nd}$ from [Shi09]. . . . .	27
3.2.	Correlation between the minimum in the form factor of the $0_2^+$ state and the node in the wave function of the $\beta$ band. . . . .	28
4.1.	Overview of the S-DALINAC with its experimental facilities. . . . .	30
4.2.	Photo of the high energy resolution $169^\circ$ spectrometer. . . . .	31
4.3.	Beam line to the high resolution electron scattering facility with the $169^\circ$ spectrometer. . . . .	32
4.4.	Focal plane detector system of the $169^\circ$ spectrometer. . . . .	33
4.5.	Dispersion matching technique. . . . .	35
4.6.	Spectrum of the $^{150}\text{Nd}(e,e')$ reaction at 73.8 MeV, taken at a scattering angle of $93^\circ$ . . . . .	36
5.1.	Spectra of the $^{150}\text{Nd}(e,e')$ reaction with an electron energy of 73.8 MeV at the scattering angles of $69^\circ$ , $93^\circ$ , $117^\circ$ , $129^\circ$ and $141^\circ$ . . . . .	42

6.1.	Experimental elastic form factor of the $^{150}\text{Nd}(e,e')$ reaction at $E_0=73.8$ MeV as a function of the scattering angle compared to the results of the phase shift analysis codes DREPHA and PHASHI. . . . .	43
6.2.	Excitation energy spectrum at an scattering angle of $69^\circ$ where the contribution of the elastic line is subtracted. . . . .	44
6.3.	Form factor of the $0_2^+$ excitation in the $^{150}\text{Nd}(e,e')$ reaction at 73.8 MeV. . . . .	45
6.4.	Absolute E0 transition rates predicted in the CBS model. . . . .	45
6.5.	Various $\rho^2(E0)$ values in the shape-phase transitional region as a function of the CBS parameter $r_\beta$ indicating the potential stiffness. . . . .	46
6.6.	Behaviour of $\rho^2(E0)$ transition strengths for the $0_2^+ \rightarrow 0_1^+$ transition for different values of $r_\beta$ . . . . .	47
7.1.	Low lying energy levels in $^{150}\text{Nd}$ for the relativistic mean field Hamiltonian, the CBS rotor model and experimental values. . . . .	50
7.2.	Low lying energy levels in $^{152}\text{Nd}$ for the relativistic mean field Hamiltonian, the CBS rotor model and experimental values. . . . .	50
7.3.	Experimental Moments of Inertia and their theoretical predictions and a comparison of the centrifugal stretching parameter $S(J)$ for the ground state band in the nuclei $^{150,152}\text{Nd}$ . . . . .	52
7.4.	Wave functions of the ground state band in $^{150,152}\text{Nd}$ for the CBS rotor model and the relativistic mean field model. . . . .	53
7.5.	Wave functions of the band heads of the $\beta$ -band in $^{150,152}\text{Nd}$ . . . . .	54
9.1.	Schematic picture of the electric dipole excitations for typical spherical nuclei and typical deformed nuclei. . . . .	60
9.2.	Systematics of the spin- $M1$ resonance in heavy deformed nuclei measured at TRIUMF [Hey10] . . . . .	62
9.3.	Double-differential cross section of the $^{154}\text{Sm}(\vec{p}, \vec{p}')$ reaction measured at $\theta = 2.8^\circ$ at TRIUMF [Hey10, Wör94] . A decomposition of the spectrum into contributions of the IVGDR (horizontally hatched) spin- $M1$ resonance (black, low $E_x$ ) and the IVGQR (black, high $E_x$ ) and a background from quasi-free scattering (lower smooth line) is shown. From Ref. [Hey10]. . . . .	62
10.1.	Energy dependence of the central parts of the nucleon-nucleon scattering in the $q \approx 0$ limit [Lov81]. . . . .	69
10.2.	Classical picture of a projectile trajectory in the coulomb scattering process. . . . .	70
10.3.	Virtual photon numbers per unit solid angle for E1 transitions in Coulomb excitation induced by 295 MeV protons on a $^{154}\text{Sm}$ target at $E_\gamma=3$ MeV and 16 MeV. . . . .	74



10.4.	Coordinate system in the projectile frame. . . . .	79
11.1.	Schematic overview of the RCNP facility in Osaka. . . . .	81
11.2.	Schematic view of one beam line polarimeter (BLP). . . . .	83
11.3.	Arrangement of the two beam line polarimeters for the determination of the beam polarization at the target position. . . . .	83
11.4.	Setup for $0^\circ$ experiments. . . . .	84
11.5.	Schematic view of the GR detector system . . . . .	87
11.6.	Targetladder which was used during the experiment. . . . .	89
11.7.	Examples of vertical beam envelopes in the y-z plane with three different focus modes of the Grand Raiden optics. . . . .	90
11.8.	Schematic view of the brass plate that has been used for the sieveslit measurements. . . . .	91
12.1.	Vertical drift chamber as a schematic view. . . . .	94
12.2.	Example of the track reconstruction. . . . .	95
12.3.	Drift time to drift length conversion. . . . .	95
12.4.	Extraction of $y_{LAS}$ , $\theta_{fp}$ , $y_{fp}$ and $\phi_{fp}$ from the sieve slit analysis . . . . .	97
12.5.	Two-dimensional $y - \theta$ histograms before and after correction . . . . .	99
12.6.	Two-dimensional histograms of the $x_{fp} - \theta_{fp}$ plane . . . . .	100
12.7.	Excitation energy calibration with the $^{26}\text{Mg}(p, p')$ reaction . . . . .	101
12.8.	Correlation between the vertical scattering angle $\phi_{fp}$ and the vertical position in the 'conventional method' for the background subtraction. On the left hand side, the untransformed data is shown and on the right hand side the transformation in equation 12.8 has been utilized. . . . .	103
12.9.	Background subtraction with the 'extended method'. . . . .	104
12.10.	Excitation energy spectrum and background spectrum of the $^{154}\text{Sm}(p, p')$ reaction at $E_p = 295$ MeV, and $\theta_{GR}=0^\circ$ , using the full acceptance of the GR. . .	104
12.11.	Background-subtracted spectrum $^{154}\text{Sm}(p, p')$ reaction at $E_p = 295$ MeV, and $\theta_{GR}=0^\circ$ , using the full acceptance of the GR. . . . .	105
12.12.	Background subtracted spectra for the $^{154}\text{Sm}(p, p')$ reaction for the $0^\circ$ and for the $3^\circ$ setting, respectively. . . . .	106
12.13.	Polarization transfer observables for $^{26}\text{Mg}$ . . . . .	110
12.14.	Polarization transfer observables for $^{154}\text{Sm}$ . . . . .	111
12.15.	Extraction of total cross section, spinflip cross section and non-spinflip cross section. . . . .	112
12.16.	Experimentally obtained photoabsorption cross section $\sigma_{abs}$ in comparison with $\gamma(x)$ data measured in Saclay [Car74] . . . . .	113

---

12.17.	Photoabsorption cross section $\sigma_{abs}$ deduced from this experiment in the lower energy region. . . . .	114
12.18.	$B(E1)$ strength distribution, obtained in this experiment. . . . .	115
12.19.	Sketch of the $B(E1)$ response in heavy deformed nuclei. . . . .	116
12.20.	Different angle cuts obtained from the finite angle measurements, using the $0^\circ$ and the $3^\circ$ setting in combination. . . . .	116
12.21.	Experimental angular distributions at different excitations energies. Energy bins with a width of 200 keV have been used. . . . .	117
12.22.	Spinflip-M1 strength distribution obtained with the unit-cross section method.	119

---

## List of Tables

---

4.1. Some technical details of the high resolution $169^\circ$ spectrometer. . . . .	33
4.2. Isotopic enrichment of the $^{150}\text{Nd}$ target which has been used in this experiment. .	36
10.1. Variables entering the Franey-Love interaction . . . . .	68
11.1. Specifications of GR and LAS spectrometer . . . . .	85
11.2. Technical details of the VDCs in the Grand Raiden and the Large Acceptance Spectrometers . . . . .	86
11.3. Technical details of the MWPCs in the Focal Plane Polarimeter . . . . .	87
11.4. Summary of the experimental conditions during this experiment . . . . .	88
11.5. Summary of the experimental conditions in each measurement . . . . .	88
12.1. Table of coefficients for the reconstruction of scattering angles . . . . .	98
12.2. Table of coefficients for the correction of $x_{fp}$ . . . . .	100
12.3. Transitions used for the energy calibration . . . . .	101
12.4. Coefficients for the correction of $y_{fp}$ . . . . .	102
12.5. Variables used for the calculation of the differential cross section . . . . .	105
B.1. List of $\rho^2(E0)$ values compared in figure 6.5. . . . .	127



---

## Preface - Off-Yrast excitations in scattering experiments with charged particles

---

The atomic nucleus is a very tiny object! What people usually do when they want to study very little objects is putting them in front of a microscope, switching the light on, looking into the eyepiece and start their investigations. The limiting factor in the resolving power is only the wavelength of the probe, in that case, the wavelength of visible light. The size of an atomic nucleus is in the order of 1-10 fm (1 fm =  $10^{-15}$  m) whereas the wavelength of the visible light is only in the 380-780 nm range. Here, the discovery of Louis de Broglie (1892-1987) improved the situation, since he found out that also particles can be associated with a wavelength and one can decrease the wavelength of particle waves by increasing their momentum. This concept is now known as 'wave-particle duality' and de Broglie won the Nobel Prize for Physics in 1929 for this groundbreaking contributions to understanding nature. Now when studying the behavior of atomic nuclei, the easiest thing is to shoot at it with an appropriate particle beam and detect reaction products.

An excitation energy spectrum already can tell a lot about the nature of the corresponding nucleus. Various excitation modes at different excitation energy ranges can be observed. Figure 0.1 shows in the upper graph a schematical picture of the typical response of a nucleus to a scattering experiment with charged particles. The excitation energy ranges taken at a finite scattering angle can be divided basically into five regions. At 0 excitation energy elastic scattering takes place. At low excitation energies (typically between 0 and 10 MeV) discrete peaks appear, originating in inelastic excitations from the ground state. These excitations are mostly due to rotational motion or surface vibrations. In the energy range above, giant resonances can be observed, where many nucleons participate in coherent motions. At even higher energies, a broad peak corresponds to the quasi-elastic scattering of the projectile off an individual nucleon in the nucleus. In the case of the Delta resonance the energy is already so high, that the substructure of the nucleon itself can be resolved and this peak results from the excitation of a nucleon.

'Switching the light on' and having a closer look into the structure of an atomic nucleus with a charged particle beam with an energy of several 10 to 100 MeV (corresponding to a wavelength in the fm-range) can provide already a quick overview about some features of the nucleus. As a very simple but significant observable, the  $R_{4/2}$  ratio (ratio of the energies of the  $4_1^+$  and the  $2_1^+$  states) can tell if the nucleus is a rotational nucleus where the energy of the first excited states follow the  $E \propto J(J + 1)$  law, or a vibrational nucleus having an equally spaced spectrum with  $E_n = n \cdot \hbar\omega$ .

Getting already a lot of information by looking at just one simple spectrum, the great power of scattering experiments with charged particles comes into play when varying the momentum

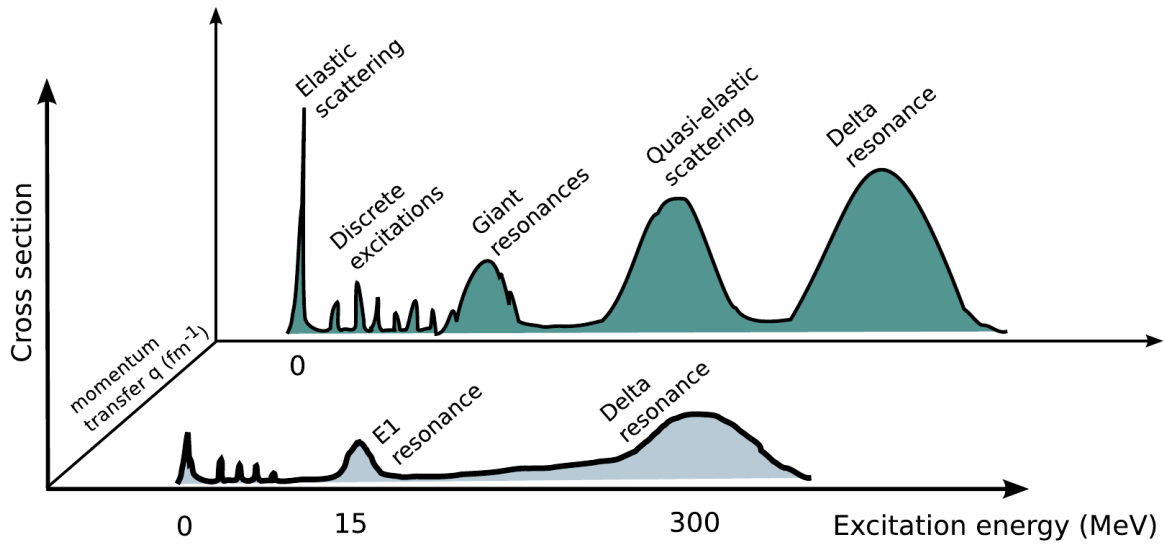


**Figure 0.1.:** Characteristic response of an atomic nucleus as a function of the excitation energy  $E_x$  and the momentum transfer  $q$ . The lower curve is for photon absorption and the upper one for charged particle scattering.

which is transferred to the nucleus. By varying the momentum transfer by either varying the scattering angle or the energy of the incoming particles, excitations can be identified by their angular momentum and even charge distributions of the ground state and excited states can be obtained.

In the framework of this PhD thesis two different types of charged-particle scattering experiments will be discussed. In the first part of this thesis, a transition from the ground state into a discrete state at very low excitation energies has been excited with electron scattering. In the second part, the spinflip  $M1$  resonance and the Giant Dipole Resonance plays a major role. Here, a polarized proton beam has been used as a probe to examine the nucleus.

The obtained scientific results demonstrate the potential of charged-particle scattering experiments for the investigation of off-Yrast low-spin excitations even for nuclei with comparatively high level density, such as deformed nuclei in the mass range of Rare Earth elements.

---

**Part I.**

**Electric monopole strength of  
the  $0_1^+ \rightarrow 0_2^+$  transition in  
 $^{150}\text{Nd}$**

---





---

## 1 Introduction

---

With increasing particle number, heavy nuclei can undergo rapid quantum phase transitions with respect to their deformation. These shape phase transitions have been studied experimentally and theoretically already in the 1960s and 1970s. Excellent reviews of the studies can be found in textbooks, e. g., [Boh75] and [Cas00]. In the early 2000s Iachello proposed analytical solutions of the geometrical Bohr Hamiltonian near the critical points of various nuclear shape phase transitions [Iac00, Iac01, Iac03] and the topic gained a new worldwide attention. Due to their predictive power and simplicity at the same time, the solutions of solving the Schrödinger equation with different forms of infinite square well potentials have attracted a great deal of interest and initiated extensive research. The solutions are named  $E(5)$  and  $X(5)$  referring to their underlying dynamical symmetries. Figure 1.1 shows the typical evolution of the potential in the quadrupole deformation coordinate  $\beta$  with increasing number of valence neutrons. The graph in the middle also includes the typical square well potential that is used in the  $X(5)$  model.

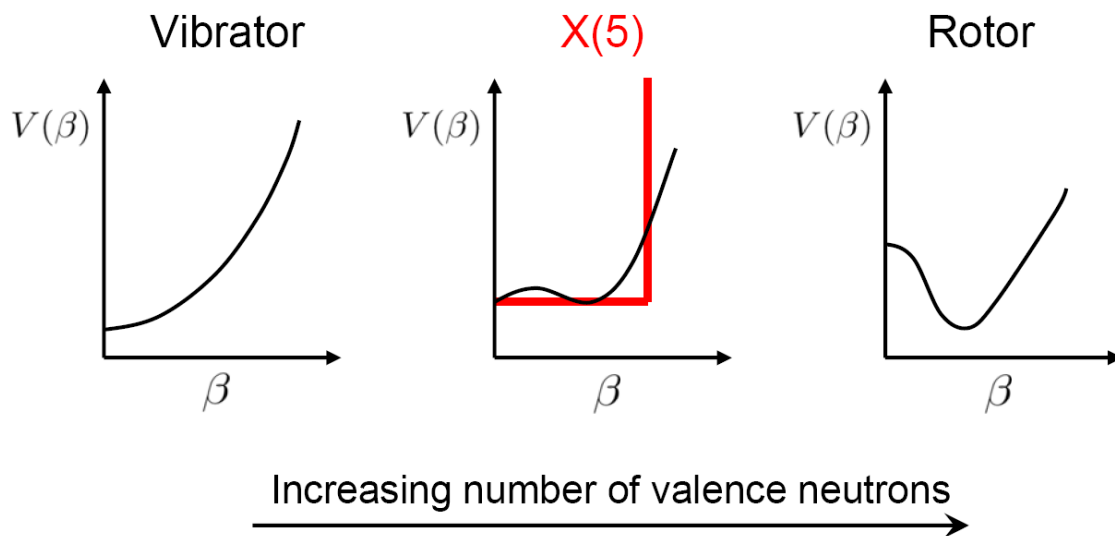


**Figure 1.1.:** Evolution of the potential as a function of the deformation variable  $\beta$  in the shape phase transitional area.

Besides the characteristic excitation energy ratios  $R_{4/2} = E(4_1^+)/E(2_1^+) = 2.20$  [for  $E(5)$ ] and  $R_{4/2} = 2.90$  [for  $X(5)$ ] or the evolution of the  $E2$  transition strengths as a function of spin along the ground state band, the properties of the quadrupole-collective, excited  $0^+$  states including its  $E2$  decays are considered as the identifying signatures of these models. Several experimental studies [Cla03, Cla04, Cas01, McC05] have dealt with these signatures.

Inspired by the success of the X(5) model that was based on the phenomenon of intrinsic excitations and centrifugal stretching in a soft potential, the X(5) model has been generalized in terms of the confined  $\beta$ -soft rotor model (CBS rotor model) [Pie04, Bon06]. Similar to the X(5) model, the CBS rotor model considers a square-well potential, however, with the inner potential boundary shifted away from  $\beta = 0$ . Alike X(5) the CBS rotor model is analytically solvable in terms of Bessel functions. It has been demonstrated to have a remarkable capability for quantitatively describing the evolution of excitation energies of rotational bands in deformed nuclei [Dus05, Dus06].

Recently, the ansatz in the CBS rotor model of an outer potential wall that stays almost constant with a varying number of valence neutrons and an inner wall that shifts to higher deformations has been microscopically justified for the given example of the isotopes  $^{150,152}\text{Nd}$  near the shape phase transitional point [Kru11]. In both compared models, the position of the outer potential wall seems to be almost independent of a transition from a spherical to an axially symmetric shape of the nucleus while the change in structure as a function of nucleon number is dominated by the change of the potential at small deformation. Figure 1.2 shows the correspondance between the CBS rotor model potential and a potential originating from a microscopic collective Hamiltonian based on the relativistic mean field model [Nik09, Li09].

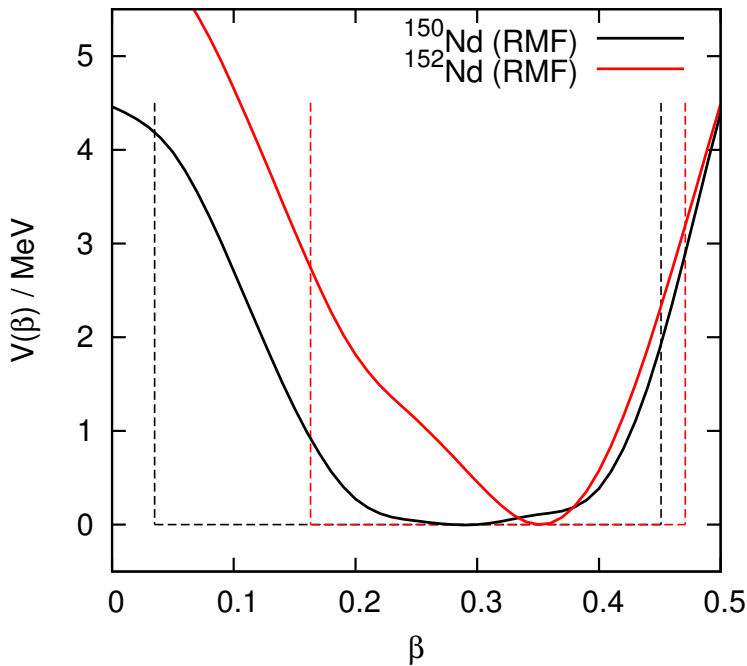


**Figure 1.2.:** CBS square well potentials (dashed lines) compared to relativistic mean field potentials (solid lines) for  $^{150}\text{Nd}$  (black) and  $^{152}\text{Nd}$  (red), respectively. The picture is taken from [Kru11].

A prominent decay mode, in particular for  $0^+$  states are  $E0$  transitions. The best general reference for  $E0$  transition strengths  $\rho^2(E0; J_i \rightarrow j_f)$  here is [Woo99]. Although the structure

of excited  $0^+$  states in the deformed even-even nuclei has been investigated extensively, their nature is still discussed controversially. Usually, the first excited  $0^+$  state is interpreted as the  $\beta$  vibrational excitation of the ground state ( $0^+_\beta$ ) and the rotational structure that is built on top of this state is called  $\beta$  band. This is due to the fact that the above mentioned solutions to the Bohr Hamiltonian show that the collective excitation modes may arise from shape oscillations parallel to the symmetry axis of the nucleus, so basically an oscillation in the  $\beta$  degree of freedom. The definition of the  $\beta$  band in terms of the collective wave functions requires the separation of the wave function  $\Psi(\beta, \gamma, \Omega) = \Psi(\beta)R(\gamma, \Omega)$ . The excitation occurs in the  $\beta$  dependent part  $\Psi(\beta)$ , resulting in a node in  $\beta$  while the ground state wave function doesn't have a node. The typical signatures of  $\beta$  vibrations are strong  $E0$  transitions to the ground state and large reduced transition probabilities  $B(E2; 0^+_\beta \rightarrow 2^+)$ .

Brentano *et al.* [Bre04] pointed out that in the interacting boson model the  $E0$  transition strengths to the ground state increase at the shape phase transitional point and continue to have large values up to the SU(3) or the O(6) dynamical symmetries. Figure 1.3 shows the IBA prediction of the  $\rho^2(E0; 0^+_2 \rightarrow 0^+_1)$  values for nuclei in the A=100 and 150 transition regions. Similarly, within the framework of the relativistic mean field, the  $\rho^2(E0; 0^+_2 \rightarrow 0^+_1)$  strength

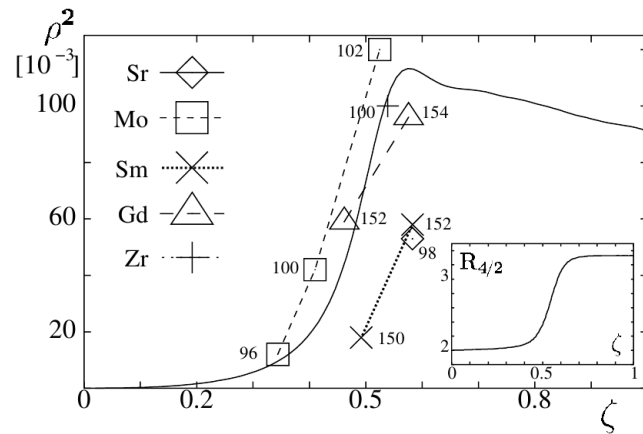


**Figure 1.3.:** Empirical  $\rho^2(E0; 0^+_2 \rightarrow 0^+_1)$  values for nuclei in the A=100 and 150 transition regions. The solid curve is the IBA prediction that shows a sudden increase of the  $\rho^2(E0)$  at the shape phase transitional point and stays at large values towards the rotor limit. The picture is taken from [Bre04].

has been investigated theoretically for the Nd-isotopes [Li09]. Figure 1.4 shows the calculated  $\rho^2(E0; 0^+_2 \rightarrow 0^+_1)$  values for the Nd-chain, where a sudden increase has been observed at the shape phase transitional point near the neutron number N=90 (corresponding to the nucleus  $^{150}\text{Nd}$  with a very high  $\rho^2(E0; 0^+_2 \rightarrow 0^+_1)$  of  $110 \cdot 10^{-3}$ ). indicating that as in the case of the IBA, the  $E0$  strength stays at a high level when approaching the rotor limit.

Measuring  $E0$  transition strengths means a challenge for experimental precision. Because of the selection rules for electromagnetic decay, the transition from  $0^+$  states to other  $0^+$  states are forbidden for  $\gamma$  rays. In terms of decay spectroscopy,  $E0$  transition strengths can be accessed

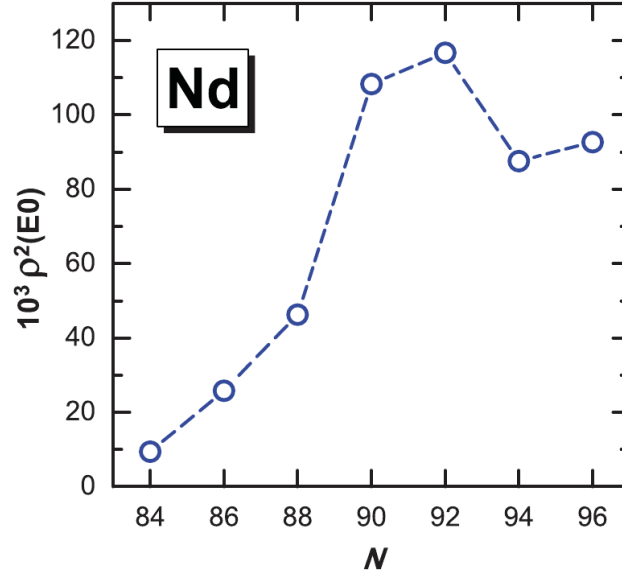


**Figure 1.4.:** Calculated monopole transition strength  $\rho^2(E0; 0_2^+ \rightarrow 0_1^+)$  as a function of neutron number  $N$  in the Nd isotopes within the framework of the relativistic mean field. Picture is taken from [Li09].

via spectroscopy of conversion electrons. Experiments with Coulomb excitation, following spectroscopy of conversion electrons in the rare earth region have only been performed for  $^{154}\text{Sm}$  and  $^{166}\text{Er}$  [Sma14, Wim09]. The large uncertainties in the measured transition strengths  $\rho^2(E0; J_i \rightarrow j_f)$  demonstrate the difficulty of such experiments. It is clear that for further discussion more data on E0 transition strengths especially in the  $N=90$  rare earth region is needed.

It has been pointed out [Shi09] that not only the E0 transition strengths provide important information about the properties for low-lying collective nuclear states [Ras60, Hey83], but non-diagonal matrix elements of the E0 operator are sensitive to the distribution of the collective wave functions along the axial deformation of the nucleus. Thus, E0 transition densities contain even more detailed information on the collective wave functions than the transition strengths and that they give a higher sensitivity to the dependence of the radial density distributions on deformation.

E0 transition strengths, transition densities and their respective electromagnetic form factors can be studied very well with electron scattering. Since inelastic electron scattering has been demonstrated to be a powerful tool to investigate form factors of E0 transitions in light and medium mass nuclei [Che10], the main purpose of this work to apply the method to a heavy deformed nucleus.  $^{150}\text{Nd}$  is a nucleus close to the shape phase transitional point around  $N \approx 90$  in the rare earth region. With increasing number of valence neutrons, a sudden shape phase transition occurs, starting from the  $N=82$  shell closure ( $^{142-148}\text{Nd}$ ) where the latter still shows vibrational character with a  $R_{4/2}$  ratio of 2.5.  $^{152}\text{Nd}$  is already a well deformed rotational nucleus

---

with a  $R_{4/2}$  ratio of 3.27, and with further increase of the neutron number, the rigid rotor limit ( $R_{4/2}$  ratio of 3.33) is approached towards midshell.

In the end 1980s an electron study has been performed at the old NIKHEF-K facility, dealing with different even-even isotopes in the Nd-chain [San91a, San91b]. Spectra have been obtained for  $^{142,146,150}\text{Nd}$  with the high-resolution electron scattering facility of NIKHEF-K and covered a momentum transfer range from 0.5 up to  $2.8 \text{ fm}^{-1}$ . In this study, excitations to the  $\beta$  band and in particular the  $0_2^+$  state has not been analyzed.

In this work, an inelastic electron scattering experiment has been performed at low momentum transfer at the high resolution  $169^\circ$  spectrometer at the S-DALINAC, in order to extract the E0 transition strength  $\rho^2(E0; 0_1 \rightarrow 0_2)$  in  $^{150}\text{Nd}$  and the radial dependence of the E0 matrix element by measuring the form factor of this transition. Part I is structured the following way. In chapter 2 the theoretical background for the geometrical collective model (CBS rotor model) will be explained. In chapter 3 the electron scattering formalism is summarized and theoretical model predictions for the transition densities are given. The experiment is described in chapter 4 and after the analysis steps which are explained in chapter 5, chapter 6 deals with the experimental results and their discussion in comparison with theory. In chapter 7 the similarity of the macroscopic CBS rotor model and a microscopic collective meanfield Hamiltonian will be investigated in terms of wave functions, energies, transition strengths and centrifugal stretching. Part I closes with some concluding remarks and an outlook on further studies in chapter 8.



---

## 2 Theoretical background

---

In this chapter the theoretical models which are used to describe and interpret the nuclear structure for the electron scattering experiments are explained. In a more general way the geometrical model with the so called Bohr Hamiltonian will be introduced and a model to solve the Bohr Hamiltonian analytically will be presented.

---

### 2.1 Collective coordinates

---

Nuclei consist in general of a large number of protons and neutrons which underlie the nuclear interaction. In order to describe nuclei in the sense of a geometrical macroscopic model, one has to go away from the picture of many single nucleons with the coordinates  $x_i$  and go to a collective description of nuclei. One usually uses a set of normal coordinates  $\alpha_{\lambda\mu}$  which can be obtained by a series expansion of the nuclear surface in terms of spherical harmonics  $Y_{\lambda\mu}(\theta, \phi)$ . The vector of the center of the nucleus (origin of the coordinate system) to the surface can be described as:

$$R(\theta, \phi) = R_0 \left[ 1 + \alpha_{00} Y_{00} + \sum_{\lambda\mu} \alpha_{\lambda\mu} Y_{\lambda\mu}(\theta, \phi) \right]. \quad (2.1)$$

$R_0$  is the mean radius of a spherical nucleus with the same volume and can be approximated by  $R_0 = 1.2 \cdot A^{1/3}$  fm. The term  $\alpha_{00} Y_{00}$  is needed for the conservation of volume which is necessary because of the incompressibility of nuclear matter. The lowest order ( $\lambda = 0$ ) simply describes the compression of the nucleus and the next order ( $\lambda = 1$ ) a shift of the whole nucleus with respect to the origin. So here the five quadrupole components with  $\lambda = 2$  built up a full set of coordinates that describes surface vibrations of lowest order. If one parameterizes this set of coordinates in a clever way such that the mass centroid axes of the nucleus coincide with the coordinate axes, the components  $a_{21}$  and  $a_{12}$  vanish and furthermore the other components equate to:

$$\alpha_{20} = \beta \cos \gamma \quad (2.2)$$

$$\alpha_{22} = \alpha_{2-2} = \frac{1}{\sqrt{2}} \beta \sin \gamma. \quad (2.3)$$

$\beta$  and  $\gamma$  are the quadrupole deformation parameters and together with the three Euler angles, they built up to a complete set of coordinates.  $\beta$  describes the axial deformation and  $\gamma$  is a measure for the triaxiality of the nucleus. The Euler angles  $\theta_1, \theta_2, \theta_3$  describe the spatial

orientation of the nucleus. Figure 2.1 shows a spherical nucleus with  $\beta = 0$ . A prolate deformed nucleus with  $\beta = 0.3$  which is a typical value for stable rare earth nuclei can be seen in 2.2 and a triaxial deformed nucleus with  $\beta = 0.3$  and  $\gamma = \pi/3$  is shown in figure 2.3.

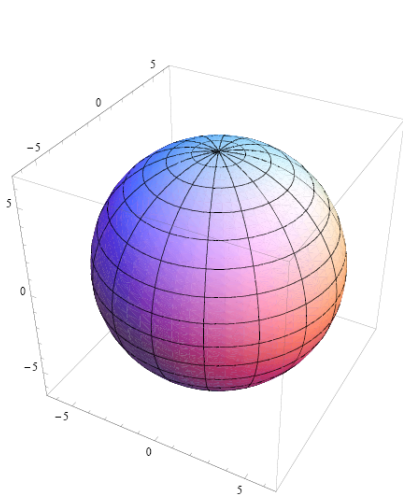


**Figure 2.1.:** Shape of a spherical nucleus with  $\beta=0$  and  $\gamma=0$ .

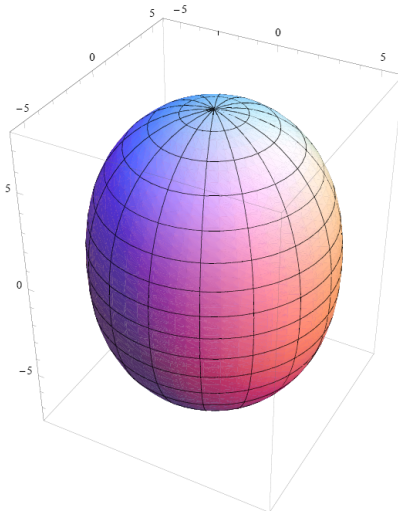


**Figure 2.2.:** Shape of an axial prolate deformed nucleus with  $\beta=0.3$  and  $\gamma=0$ .

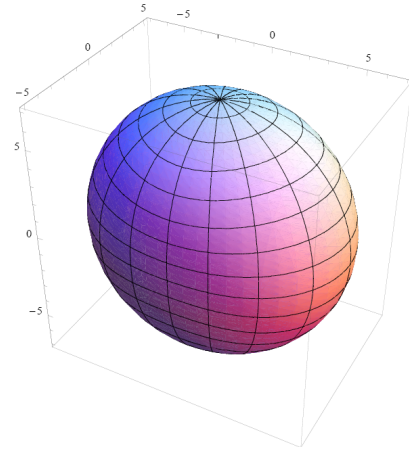


**Figure 2.3.:** Shape of a triaxial deformed nucleus with  $\beta=0.3$  and  $\gamma=\pi/3$ .



---

## 2.2 The collective Bohr Hamiltonian

---

The collective Hamiltonian in a very general form [Boh52]

$$\hat{H} = \hat{T}_{\text{vib}} + \hat{T}_{\text{rot}} + V_{\text{coll}} \quad (2.4)$$

describes the collective motion of a nucleus with a vibrational kinetic energy

$$\begin{aligned} \hat{T}_{\text{vib}} = & -\frac{\hbar^2}{2\sqrt{wr}} \left\{ \frac{1}{\beta^4} \left[ \frac{\partial}{\partial \beta} \sqrt{\frac{r}{w}} \beta^4 B_{\gamma\gamma} \frac{\partial}{\partial \beta} - \frac{\partial}{\partial \beta} \sqrt{\frac{r}{w}} \beta^3 B_{\beta\gamma} \frac{\partial}{\partial \gamma} \right] \right. \\ & \left. + \frac{1}{\beta \sin 3\gamma} \left[ -\frac{\partial}{\partial \gamma} \sqrt{\frac{r}{w}} \sin 3\gamma B_{\beta\gamma} \frac{\partial}{\partial \beta} + \frac{1}{\beta} \frac{\partial}{\partial \gamma} \sqrt{\frac{r}{w}} \sin 3\gamma B_{\beta\beta} \frac{\partial}{\partial \gamma} \right] \right\} \end{aligned} \quad (2.5)$$

and a rotational kinetic energy

$$\hat{T}_{\text{rot}} = \frac{1}{2} \sum_{k=1}^3 \frac{\hat{J}_k^2}{\mathcal{I}_k} . \quad (2.6)$$

Here,  $V_{\text{coll}}$  is the collective potential.  $\hat{J}_k$  denotes the components of the angular momentum in the body-fixed frame of a nucleus, and the mass parameters  $B_{\beta\beta}$ ,  $B_{\beta\gamma}$ ,  $B_{\gamma\gamma}$  [Jol09], as well as the moments of inertia  $\mathcal{I}_k$ , depend on the quadrupole deformation variables  $\beta$  and  $\gamma$ :

$$\mathcal{I}_k = 4B_k \beta^2 \sin^2(\gamma - 2k\pi/3) . \quad (2.7)$$

Two additional quantities that appear in the expression for the vibrational energy:  $r = B_1 B_2 B_3$ , and  $w = B_{\beta\beta} B_{\gamma\gamma} - B_{\beta\gamma}^2$ , determine the volume element in the collective space.

---

### 2.2.1 E0 transitions in quadrupole collective models

---

The  $E0$  transition strength is defined by

$$\frac{1}{\tau(E0)} = \rho_{\text{if}}^2(\Omega_K + \Omega_{L_i} + \dots + \Omega_{IP}) \quad (2.8)$$

where

$$\rho_{\text{if}}^2(E0) = \frac{|\langle \Psi_{\text{final}} | m(E0) | \Psi_{\text{initial}} \rangle|^2}{(eR^2)^2} \quad (2.9)$$

with the  $E0$  transition operator

$$m(E0) = \int \rho(\vec{r}) r^2 d^3r \quad (2.10)$$

obtained in the long wave-length approximation [Boh75]. Tabulations of the 'electronic' factors  $\Omega_i$  in equation (2.8) are given by Bell *et al.* [Bel70] or can be calculated with an online web interface [bri]. The quantity  $\rho_{if}^2$  is a dimensionless quantity and is usually given in units of  $10^{-3}$ . In the homogeneous-charge density approximation

$$\rho(\vec{r}) = \rho_0 = \frac{Ze}{\frac{4\pi}{3}R^3} \quad (2.11)$$

one obtains

$$m(E0) = \frac{3}{5}ZeR^2 \left( 1 + \frac{5}{4\pi}\alpha_{20}^2 + \frac{10}{7\pi}\sqrt{\frac{5}{16\pi}}\alpha_{20}^3 + \dots \right) \quad (2.12)$$

from the integration of equation (2.10) within the nuclear interior limited by equation (2.1).

To lowest order in  $\alpha_2$  the  $E0$  operator is in general obtained as [Woo99]

$$\hat{T}(E0) = \frac{3}{5}ZeR^2 \left( 1 + \frac{5}{4\pi}\sum_{\mu}|\hat{\alpha}_{2\mu}|^2 \right). \quad (2.13)$$

The constant term in equation (2.12) cannot induce transitions between orthogonal states. Therefore, to lowest order in the deformation parameter, nuclear  $E0$  transitions originate for axially symmetric quadrupole deformation from the part

$$\hat{T}(E0)_{tr} = \frac{3}{4\pi}ZeR^2 \hat{\beta}^2, \quad (2.14)$$

where  $\sum_{\mu}|\hat{\alpha}_{2\mu}|^2 = |\hat{\alpha}_{2,0}|^2 = \hat{\beta}^2$  for axial symmetry with  $\gamma = 0$ . Data on  $E0$  transitions have been reviewed by Wood *et al.* [Woo99] and in [Kib05]. The  $E0$  transition operator is similar in structure to the  $\beta$ -dependent part of the  $E2$  transition operator in the axially symmetric case with  $\gamma = 0$

$$\hat{T}(E2)_{\Delta K=0} = \frac{3}{4\pi}ZeR^2 \hat{\beta}. \quad (2.15)$$

---

## 2.2.2 Derivation of $\rho^2(E0)$ transition strength as a function of potential stiffness

---

A derivation of  $\rho^2(E0)$  transition strength as a function of potential stiffness has been worked out with the help of Professor Jolos [Jola] from Dubna, Russia, during the research on reference [Bon09]. In this section the most important formula are presented while the whole derivation can be found in appendix A. An expression of the  $\rho^2(E0)$  transition strength only depending on experimental nuclear structure observables can be found to be:

$$\rho^2(E0; 0_2^+ \rightarrow 0_1^+) = 2 \left( \frac{E(2_1^+) - E(0_1^+)}{E(0_2^+) - E(0_1^+)} \right) \frac{(B(E2; 0_1^+ \rightarrow 2_1^+))^2}{\left(\frac{3Z}{4\pi}\right)^2 (e^2 R^4)^2}. \quad (2.16)$$

Using the relation between  $B(E2; 0_1^+ \rightarrow 2_1^+)$  and  $\langle 0_1^+ | \beta^2 | 0_1^+ \rangle$ :

$$B(E2; 0_1^+ \rightarrow 2_1^+) = \left( \frac{3Z}{4\pi} e R^2 \right)^2 \langle 0_1^+ | \beta^2 | 0_1^+ \rangle \quad (2.17)$$

one obtains from equation 2.16:

$$\rho^2(E0; 0_2^+ \rightarrow 0_1^+) = 2 \left( \frac{E(2_1^+) - E(0_1^+)}{E(0_2^+) - E(0_1^+)} \right) \left( \frac{3Z}{4\pi} \right)^2 \langle 0_1^+ | \beta^2 | 0_1^+ \rangle^2. \quad (2.18)$$

The most important observation from equation 2.18 is that when the stiffness of the potential in  $\beta$  increases, the ratio  $\left( \frac{E(2_1^+) - E(0_1^+)}{E(0_2^+) - E(0_1^+)} \right)$  decreases. As a result  $\rho^2(E0; 0_2^+ \rightarrow 0_1^+)$  should also decrease.

---

## 2.3 The confined $\beta$ -soft rotor model

---

In this chapter the confined  $\beta$ -soft rotor model (CBS rotor model) [Pie04] will be described and a solution to the Schrödinger Equation by using a simple square well potential in the deformation variable  $\beta$  will be presented. The CBS rotor model represents an approximate analytical solution to the collective Hamiltonian in equation (2.4) proposed by Bohr and Mot-

telson [Boh52] Inserting (2.5) into equation (2.4) and assuming that  $B_k = B_{\gamma\gamma} = B_{\beta\beta} = B$  and  $B_{\beta\gamma} = 0$ , the Hamiltonian simplifies to

$$H = -\frac{\hbar^2}{2B} \left[ \frac{1}{\beta^4} \frac{\partial}{\partial \beta} \beta^4 \frac{\partial}{\partial \beta} + \frac{1}{\beta^2 \sin 3\gamma} \frac{\partial}{\partial \gamma} \sin 3\gamma \frac{\partial}{\partial \gamma} - \frac{1}{4\beta^2} \sum_k \frac{\hat{J}_k^2}{\sin^2(\gamma - \frac{2}{3}\pi k)} \right] + V(\beta, \gamma). \quad (2.19)$$

Assuming a separable potential  $V(\beta, \gamma) = u(\beta) + v(\gamma)$  the wave functions approximately separate into

$$\Psi(\phi, \theta, \psi, \beta, \gamma) = \xi_L(\beta) \eta_K(\gamma) \Phi_{MK}^I(\Omega). \quad (2.20)$$

The angular part corresponds to linear combinations of the Wigner functions [Wig71]

$$\Phi_{MK}^I(\Omega) = \sqrt{\frac{2I+1}{16\pi^2(1+\delta_{K0})}} [D_{MK}^{I*}(\Omega) + (-1)^I D_{M-K}^{I*}(\Omega)] \quad (2.21)$$

and  $\eta_K$  denotes the appropriate wave function in  $\gamma$ . For sufficiently axially symmetric prolate nuclei one might consider a steep harmonic oscillator in  $\gamma$  [Iac01].  $\xi_L(\beta)$  describes the part of the wave function depending on the deformation variable  $\beta$ . The approximate separation of variables [Iac01] leads to a differential equation for  $\xi_L(\beta)$

$$-\frac{\hbar^2}{2B} \left[ \frac{1}{\beta^4} \frac{\partial}{\partial \beta} \beta^4 \frac{\partial}{\partial \beta} - \frac{1}{3\beta^2} L(L+1) + u(\beta) \right] \xi_L(\beta) = E \xi_L(\beta). \quad (2.22)$$

It can be considered as the 'radial' equation in the space of quadrupole deformation parameters. It contains the angular momentum dependence through the centrifugal term. The CBS rotor model assumes for prolate axially symmetric nuclei an infinite square well potential  $u(\beta)$ , with boundaries at  $\beta_M > \beta_m \geq 0$  (see figure 2.5). For this potential the differential equation (2.22) is analytically solvable. The ratio

$$r_\beta = \frac{\beta_m}{\beta_M} \quad (2.23)$$

parameterizes the width of this potential, that is the stiffness of the nucleus in the  $\beta$  degree of freedom. Figure 2.5 shows the CBS potential for a value of  $r_\beta = 0.3$ . For  $r_\beta = 0$  the X(5) limit is obtained where a large range of  $\beta$  values are possible, leading to large fluctuations in  $\beta$  (see figure 2.4). The Rigid Rotor Limit without fluctuations in  $\beta$  corresponds to  $r_\beta \rightarrow 1$ .

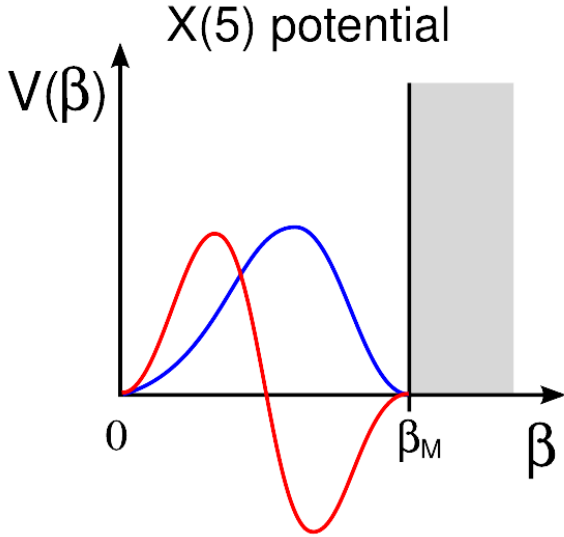


**Figure 2.4.:** X(5) potential as a function of the deformation parameter  $\beta$ . In blue, the ground state wave function is shown and in red the wave function of the  $0^+$  state of the  $\beta$  band.

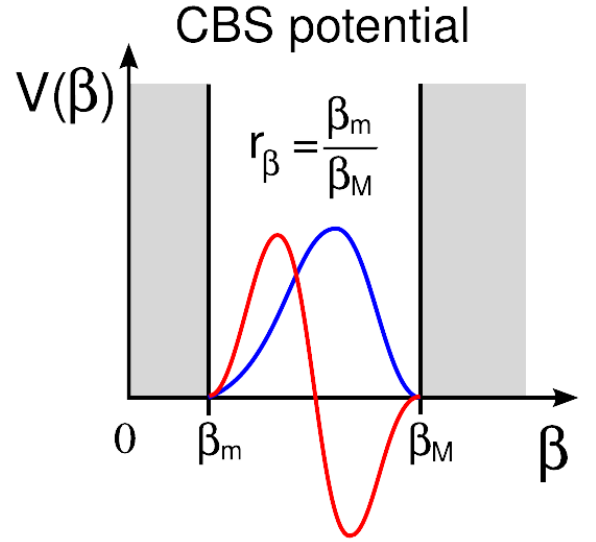


**Figure 2.5.:** CBS potential as a function of the deformation parameter  $\beta$ . In blue, the ground state wave function is shown and in red the wave function of the  $0^+$  state of the  $\beta$  band.

The quantization condition of the CBS rotor model is

$$Q_{\nu(L)}^{r\beta}(z) = J_{\nu(L)}(z)Y_{\nu(L)}(r\beta z) - J_{\nu(L)}(r\beta z)Y_{\nu(L)}(z) = 0 \quad (2.24)$$

with  $J_\nu$  and  $Y_\nu$  being Bessel functions of first and second kind of irrational order  $\nu = \sqrt{[L(L+1) - K^2]/3 + 9/4}$ . For a given structural parameter  $r_\beta$  and any spin value  $L$  the  $s$ th zero of equation (2.24) is denoted by  $z_{L,s}^{r\beta}$ . The full solution of equation(2.22) with the aforementioned choice of the CBS square-well potential is then given as

$$\xi_{L,s}(\beta) = c_{L,s}\beta^{-\frac{3}{2}} \left[ J_\nu \left( z_{L,s}^{r\beta} \frac{\beta}{\beta_M} \right) + \frac{J_\nu \left( r_\beta z_{L,s}^{r\beta} \right)}{Y_\nu \left( r_\beta z_{L,s}^{r\beta} \right)} Y_\nu \left( z_{L,s}^{r\beta} \frac{\beta}{\beta_M} \right) \right]. \quad (2.25)$$

The normalization constant  $c_{L,s}$  of the wave function (2.25) is given by the normalization condition

$$1 = \int_{\beta_m}^{\beta_M} \beta^4 [\xi_{L,s}(\beta)]^2 d\beta. \quad (2.26)$$

The eigenvalues of equation (2.22) are obtained as

$$E_{L,s} = \frac{\hbar^2}{2B\beta_M^2} \left( z_{L,s}^{r_\beta} \right)^2. \quad (2.27)$$

For convenience, the reduced deformation parameter  $b = \frac{\beta}{\beta_M} \in [r_\beta, 1]$  is used where appropriate.

The CBS rotor model well describes the evolution of low-energy  $0^+$  bands [Pie04], ground bands of strongly deformed nuclei [Dus05], and the dependence of relative moments of inertia as a function of spin in deformed transitional nuclei [Dus06]. It has also been successfully used for studying relative as well as absolute  $E0$  transitions in the region of the X(5) nuclei up to the rigid rotor limit [Bon09].

---

### 2.3.1 $E0$ transition strengths in the CBS model

---

Electromagnetic transition strengths can be calculated from the wave functions given above. For  $E0$  transitions one obtains with Eqs. (2.9,2.14)

$$\rho_{if}^2(E0) = \left( \frac{3Z}{4\pi} \right)^2 |\langle \psi_f | \hat{\beta}^2 | \psi_i \rangle|^2 \quad (2.28)$$

$$= \left( \frac{3}{4\pi} \right)^2 Z^2 \beta_M^4 |\langle \xi_f | \hat{b}^2 | \xi_i \rangle|^2 \quad (2.29)$$

between states that only differ in the  $\beta$ -dependent part of the wave function, *i.e.*,  $\langle D_f | D_i \rangle = \langle \eta_f | \eta_i \rangle = 1$ . As a function of the choice of the potential, *i.e.*, as a function of the nuclear deformation ( $\beta_M$ ) and the nuclear stiffness against centrifugal stretching ( $r_\beta$ ), the  $E0$  transition strengths can be expressed as

$$\rho_{if}^2(E0) = \left( \frac{3}{4\pi} \right)^2 Z^2 \beta_M^4 \left[ \int_{r_\beta}^1 \xi_f^*(b) b^2 \xi_i(b) b^4 db \right]^2 \quad (2.30)$$

$$= q_{E0}(\beta_M) \left[ m_{2,r_\beta}(J_i \rightarrow J_f) \right]^2, \quad (2.31)$$

with the matrix element

$$m_{k,r\beta}(J_i \rightarrow J_f) = \int_{r\beta}^1 \xi_i(\mathfrak{b}) \mathfrak{b}^k \xi_f(\mathfrak{b}) \mathfrak{b}^4 d\mathfrak{b} \quad (2.32)$$

of  $k$ th order in the reduced deformation variable  $\mathfrak{b}$  that only depends on the nuclear stiffness parameter  $r\beta$ . The magnitude of the nuclear deformation ( $\beta_M$ ) appears in the scaling constant  $q_{E0}(\beta_M)$ . The corresponding expression for  $B(E2)$  transition strengths of  $\Delta K = 0$  transitions follows as

$$B(E2; J_i \rightarrow J_f) = q_{E2}(\beta_M) \left( C_{J_i 0 2 0}^{J_f 0} \right)^2 \left[ m_{1,r\beta}(J_i \rightarrow J_f) \right]^2, \quad (2.33)$$

with the scaling constant

$$q_{E2}(\beta_M) = \left( \frac{3}{4\pi} \right)^2 \beta_M^2 Z^2 e^2 R^4. \quad (2.34)$$

$C_{J_i 0 2 0}^{J_f 0}$  denotes a Clebsch-Gordan coefficient. Deviations from the homogeneous-charge density approximation might be taken into account to lowest order by an effective charge  $Ze \rightarrow q_{E\lambda} Ze$ , with  $q_{E\lambda} \approx 1$  for electric transitions with multipolarity  $\lambda$ .

---

## 2.4 Microscopic relativistic mean-field approach

---

In this chapter a microscopic collective Hamiltonian based on the relativistic mean field model [Nik09, Li09] is introduced. In section 7 comparisons between the CBS rotor model and this microscopic mean field approach will be discussed. The kinetic energy part of the Hamiltonian is in the general form as already seen in equations (2.4) - (2.6). The seven functions, i.e. the three moments of inertia  $\mathcal{J}_k$ , the three mass parameters  $B_{\beta\beta}$ ,  $B_{\beta\gamma}$ ,  $B_{\gamma\gamma}$ , and the collective potential  $V_{\text{coll}}$ , are determined by the choice of a particular microscopic nuclear energy-density functional or effective interaction. In the particle-hole channel the relativistic functional PC-F1 (point-coupling Lagrangian) [Bür02b] has been used, as in the studies of shape transitions in the Nd-chain [Li09]. Also a density-independent  $\delta$  force in the particle-particle channel treated by the BCS approximation was used. The moments of inertia are calculated microscopically from the Inglis-Belyaev formula:

$$\mathcal{J}_k = \sum_{i,j} \frac{(u_i v_j - v_i u_j)^2}{E_i + E_j} \langle i | \hat{J}_k | j \rangle^2 \quad k = 1, 2, 3, \quad (2.35)$$

where the summation runs over the proton and neutron quasi-particle states, and  $k$  denotes the axis of rotation. The quasi-particle energies  $E_i$ , occupation probabilities  $\nu_i$ , and single-nucleon wave functions  $\psi_i$  are determined by solutions of the constrained RMF+BCS equations. The mass parameters associated with the two quadrupole collective coordinates  $q_0 = \langle \hat{Q}_{20} \rangle$  and  $q_2 = \langle \hat{Q}_{22} \rangle$  are also calculated in the cranking approximation

$$B_{\mu\nu}(q_0, q_2) = \frac{\hbar^2}{2} \left[ \mathcal{M}_{(1)}^{-1} \mathcal{M}_{(3)} \mathcal{M}_{(1)}^{-1} \right]_{\mu\nu}, \quad (2.36)$$

with

$$\mathcal{M}_{(n),\mu\nu}(q_0, q_2) = \sum_{i,j} \frac{\langle i | \hat{Q}_{2\mu} | j \rangle \langle j | \hat{Q}_{2\nu} | i \rangle}{(E_i + E_j)^n} (u_i \nu_j + \nu_i u_j)^2. \quad (2.37)$$

In contrast to the CBS Model, the potential  $V_{\text{coll}}$  in the collective Hamiltonian Equation (2.4) is obtained by subtracting the zero-point energy corrections from the total energy that corresponds to the solution of constrained RMF+BCS equations, at each point on the triaxial deformation plane.

The Hamiltonian (2.4) describes quadrupole vibrations, rotations, and the coupling of these collective modes. The corresponding eigenvalue problem is solved using an expansion of eigenfunctions in terms of a complete set of basis functions that depend on the deformation variables  $\beta$  and  $\gamma$ , and the Euler angles  $\phi$ ,  $\theta$  and  $\psi$ . The diagonalization of the Hamiltonian yields the excitation energies and collective wave functions

$$\Psi_{\alpha}^{IM}(\beta, \gamma, \Omega) = \sum_{K \in \Delta I} \psi_{\alpha K}^I(\beta, \gamma) \Phi_{MK}^I(\Omega), \quad (2.38)$$

that are used to calculate observables. The angular part corresponds to linear combinations of the Wigner functions [see equation (2.21)] and the summation in equation (2.38) is over the allowed set of  $K$  values:

$$\Delta I = \begin{cases} 0, 2, \dots, I & \text{for } I \bmod 2 = 0 \\ 2, 4, \dots, I - 1 & \text{for } I \bmod 2 = 1. \end{cases} \quad (2.39)$$

For a given collective state in equation (2.38), the probability density distribution in the  $\beta - \gamma$ -plane is defined by

$$\rho_{I\alpha}(\beta, \gamma) = \sum_{K \in \Delta I} |\psi_{\alpha K}^I(\beta, \gamma)|^2 \beta^3 |\sin 3\gamma|. \quad (2.40)$$



The normalization reads

$$\int_0^{\infty} \beta d\beta \int_0^{2\pi} d\gamma \rho_{I\alpha}(\beta, \gamma) = 1 . \quad (2.41)$$

If we integrate the wave function (2.38) along  $\gamma$ , we obtain the projection

$$\rho'_{I\alpha}(\beta) = \sum_{K \in \Delta I} \int_0^{2\pi} |\psi_{\alpha K}^I(\beta, \gamma)|^2 \beta^4 |\sin 3\gamma| d\gamma . \quad (2.42)$$

of the density distribution as a function of  $\beta$  for the desired comparison with the results from the CBS model. Its normalization reads:

$$\int_0^{\infty} \rho'_{I\alpha}(\beta) d\beta = 1 . \quad (2.43)$$



---

### 3 Inelastic electron scattering at low momentum transfer

---

In this chapter basics of the description of inelastic electron scattering at low momentum transfer will be given. It is based on [Übe71], although the notation of [Bur08, Neu97b] has been used.

---

#### 3.1 Electron scattering formalism

---

Incoming electrons with the energy  $E_0$  scatter off atomic nuclei. The ground state and excited states with discrete excitation energies will be directly visible in an energy-loss spectrum, when the scattered electrons with the energy  $E_f$  are bent at an angle of  $\theta$  in a dipole magnet and selected by their momenta in the focal plane of the spectrometer. In these scattering processes energy is conserved

$$E_0 = E_f + E_x + E_R. \quad (3.1)$$

$E_x$  is the excitation energy of the excited state and  $E_R$  the recoil energy of the nucleus. The latter is negligible and equation 3.1 simplifies to

$$E_x = E_0 - E_f. \quad (3.2)$$

Momentum conservation requires

$$\vec{q} = \vec{p}_i - \vec{p}_f, \quad (3.3)$$

where  $p_i$  and  $p_f$  are the electron momenta before and after the scattering process. The absolute value of the momentum transfer  $q$  can be written as

$$q = \frac{1}{\hbar c} \sqrt{2E_0(E_0 - E_x)(1 - \cos \theta) + E_x^2}. \quad (3.4)$$

Due to the attraction of the Coulomb force during the scattering process, especially for heavier nuclei, the effective energy of the electron is higher than its energy in the center of mass system. This leads to an increase in the momentum transfer.

$$q_{eff} = q \left( 1 + \frac{3}{2} \frac{Ze^2}{\hbar c E_0 R_{eq}} \right) \quad (3.5)$$

Here,  $\hbar c = 197 \text{ MeV fm}$ ,  $e^2 = 1,44 \text{ MeV fm}$  and  $R_{eq}$  is the radius of a homogeneously charged sphere.

The electron interacts with the charge and current density of the nucleus by exchange of a virtual photon. In the first order perturbation theory only the exchange of one photon is used. Then the differential cross section  $\left(\frac{d\sigma}{d\Omega}\right)_\theta$  at the angle  $\theta$  can be written as

$$\left(\frac{d\sigma}{d\Omega}\right)_\theta = \frac{1}{4\pi^2(\hbar c)^2} E_i E_f \left(\frac{p_f}{p_i}\right) \left(\frac{2J_f + 1}{2J_i + 1}\right) f_{rec} |\langle \Psi_f | \hat{H}_{int} | \Psi_i \rangle|^2. \quad (3.6)$$

Here,  $J_i$  and  $J_f$  the total angular momenta before and after the scattering process.  $\hat{H}_{int}$  is the Hamiltonian of the interaction and  $f_{rec}$  the recoil factor

$$f_{rec} = \left(1 + \frac{2E_i \sin^2(\theta/2)}{Mc^2}\right)^{-1} \quad (3.7)$$

The matrix element  $M(\lambda(q)) = \langle \Psi_f | \hat{H}_{int} | \Psi_i \rangle$  contains the wave function of the initial and final state and all informations about the interaction. In order to measure this matrix element, one defines the squared form factor

$$|F(E_0, q)|^2 = \frac{\left(\frac{d\sigma}{d\Omega}\right)_{exp}}{\left(\frac{d\sigma}{d\Omega}\right)_{Mott}} \quad (3.8)$$

as the ratio of the experimental differential cross section and the Mott cross section defined as

$$\left(\frac{d\sigma}{d\Omega}\right)_{Mott} = \left(\frac{Ze^2}{2E_0}\right)^2 \frac{\cos^2 \theta/2}{\sin^4 \theta/2}, \quad (3.9)$$

The squared form factor  $|F(E_0, q)|^2$  is a function of the momentum transfer  $q$ . Extracting the  $q$ -dependence of the form factor, one can obtain informations about the charge and current distributions in the nucleus.

Under electromagnetic interaction, the total angular momentum and the parity of a system are conserved. For a given angular momentum  $J$  and parity  $\pi$  the selection rules for the multipolarity  $\lambda$  and the transition from the initial state  $|\psi_i\rangle$  to the final state  $|\psi_f\rangle$  are for the angular momentum:

$$|J_i - J_f| \leq \lambda \leq J_i + J_f. \quad (3.10)$$

and for the parity:

$$\pi_i \pi_f = (-1)^\lambda \text{ for electric transitions and} \quad (3.11)$$

$$\pi_i \pi_f = (-1)^{\lambda+1} \text{ for magnetic transitions.} \quad (3.12)$$

In the case of light nuclei, the wave function of the incoming and the scattered electrons can be approximated with plane waves (Plane Wave Born Approximation, PWBA). In heavy nuclei, where the Coulomb potential plays a major role as in the case of  $^{150}\text{Nd}$ , the influence of the coulomb field is so big for the incoming electrons that they become accelerated when approaching the nucleus and slowed down after the scattering process. This results in a distortion of the outgoing electron wave. In this case we explicitly need a nuclear model for calculating  $M\lambda(q)$ . Solving numerically the Dirac equation one can extract the form factors. In order to deduce the transition strengths one has to scale the experimental data to the theory.

---

## 3.2 Model predictions for the $0_1^+ \rightarrow 0_2^+$ $E0$ transition in $^{150}\text{Nd}$

---



---

### 3.2.1 Effective operator for the $E0$ transition density

---

In a recent work [Shi09] a semi-microscopic method has been applied for the calculation of properties of shape-phase transitional nuclei. Firstly, the effective density operator has been constructed at a microscopical level. In a second step the collective wave functions obtained in the CBS rotor model (see section 2.3) have been used to calculate the matrix elements of the effective operator by integration over the collective variables.

The single particle density operator  $\hat{\rho}(\vec{r})$  can be expressed in terms of the particle creation and annihilation operators corresponding to the Nilsson single-particle basis with the deformation parameters  $\beta$  and  $\gamma$ . According to [Shi09] it is written as

$$\hat{\rho}(\vec{r}) = \sum_{s,s'} \varphi_s^*(\vec{r}, \beta) \varphi_{s'}(\vec{r}, \beta) a_s^\dagger(\beta) a_{s'}(\beta) \quad (3.13)$$

with the single-particle wave functions

$$\varphi(\vec{r}, \beta) = \sum_{n,l,j} a_{nlj}^{(s)}(\beta) R_{nlj}(r) \left( Y_l(\theta, \phi) \chi_{1/2} \right)_{j\Omega_s}, \quad (3.14)$$

where  $a_{nlj}^{(s)}(\beta)$  are the Nilsson expansion coefficients,  $R_{nlj}(r)$  is a radial wave function corresponding to the Schrödinger equation with the spherically symmetric Woods-Saxon potential. Then, the average of  $\hat{\rho}(\vec{r})$  over the quasi-particle vacuum corresponding to the equilibrium deformation  $\beta$  is given as

$$\langle \beta | \hat{\rho}(\vec{r}) | \beta \rangle = \sum_s |\varphi_s(\vec{r}, \beta)|^2 v_s^2(\beta), \quad (3.15)$$

where  $v_s^2(\beta)$  denotes the single-particle occupation probability. In order to calculate the  $E0$  transition density for the  $0_1^+ \rightarrow 0_2^+$  transition it is necessary to integrate equation (3.15) over the Euler angles, resulting in

$$\langle \beta | \hat{\rho}(r) | \beta \rangle = \int d\Omega \langle \beta | \hat{\rho}(\vec{r}) | \beta \rangle \quad (3.16)$$

$$\sum_{n,n',l,j} a_{nlj}^{(s)}(\beta) a_{n'lj}^{(s)}(\beta) R_{nlj}(r) R_{n'lj}(r) v_s^2(\beta). \quad (3.17)$$

The full expression for the effective  $E0$  transition density operator  $\rho_{\text{eff}}(r, \beta)$  has been obtained by using the Generator Coordinate Method (GCM) which is well described in [Rin80]. The result is

$$\rho_{\text{eff}}(r, \beta) = \langle \beta | \hat{\rho}(r) | \beta \rangle + F(r) + \left( \frac{1}{2Z} F(r) - G(r) \right) \frac{\partial^2}{\partial \beta^2} \quad (3.18)$$

where the radial functions  $F(r)$  and  $G(r)$  are lengthy expressions containing the spherically symmetric part of the nuclear single-particle potential  $V_{sp}(r)$ , the single-particle energies  $\epsilon_s$ , the single quasi-particle energies  $E_s$ , the energy gap  $\Delta$  and the matrix elements  $\langle s | f Y_{20} | t \rangle$  that are all functions of the deformation parameter  $\beta$ .

---

### 3.2.2 Neutron and proton transition densities

---

Using the collective wave functions obtained in the CBS rotor model, the neutron and proton transition densities for the  $0_1^+ \rightarrow 0_2^+$  transition in  $^{150}\text{Nd}$  could have been calculated according to equation (3.18) and are depicted in figure 3.1. It has been found to be useful to plot the ordinate of a transition density multiplied by  $r^2$  in order to enhance the effects on the nuclear surface. Since electron scattering is only sensitive to the charge distribution and not on the matter distribution, only the proton transition density distribution has been used.

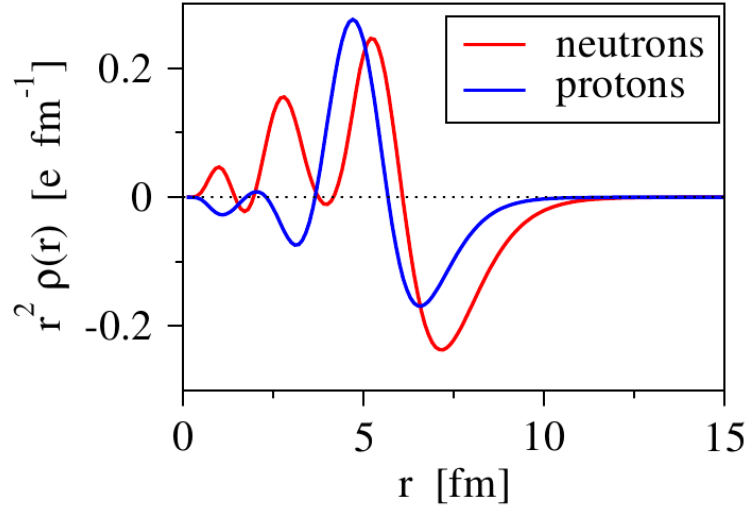
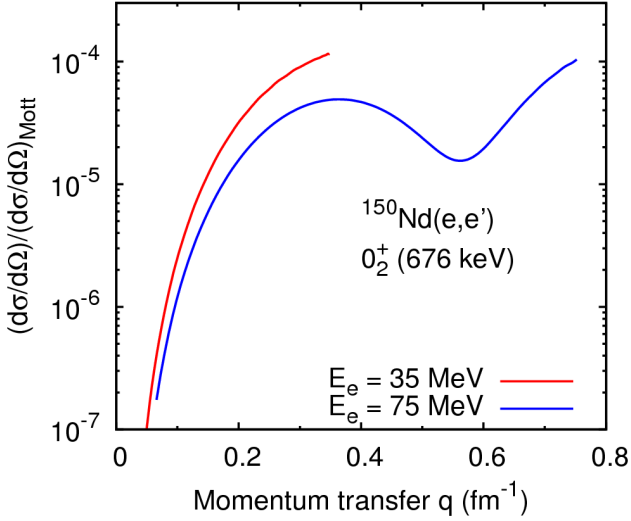


**Figure 3.1.:** Calculated proton and neutron transition densities for the  $0_1^+ \rightarrow 0_2^+$  transition in  $^{150}\text{Nd}$  from [Shi09]. In the case of electron scattering, only the proton transition densities are used.

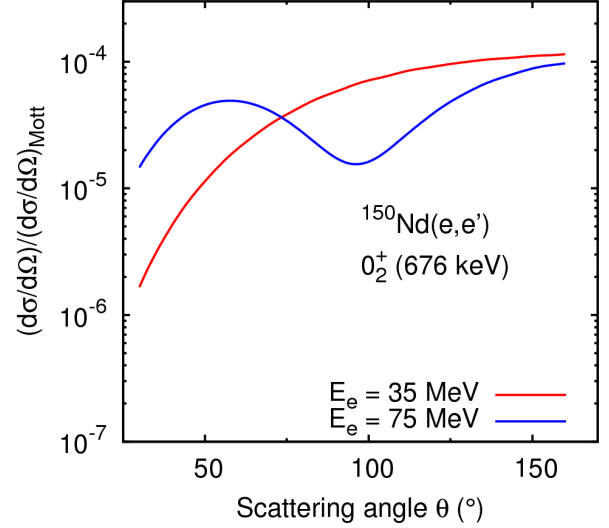
### 3.2.3 Predicted DWBA form factors for the electron scattering experiment

The proton transition densities have been taken as an input for a DWBA calculation [Pon, Tua68]. The DWBA calculation has been performed for two electron energies. Figure 3.2(a) shows in red the electron scattering form factor for the  $0_1^+ \rightarrow 0_2^+$  transition in  $^{150}\text{Nd}$  for an electron energy of 35 MeV and in blue for an energy of 75 MeV as a function of the momentum transfer. It is obvious that for higher electron energies a much larger range of momentum transfer is accessible. Cross sections of the first maximum, the first minimum and even the second maximum could be obtained using a 75 MeV electron beam. That's why this energy was chosen for the experiment. Figure 3.2(b) shows the same form factors as figure 3.2(a) but here, they are plotted as a function of the scattering angle  $\theta$ . In figure 3.2(c) the cross section of the elastic scattering process (black curve) is compared to the inelastic form factor of the  $0_2^+$  state. Here, the immense difference in cross section turns out, since there are at some points almost 5 orders of magnitudes between the respective cross section. Finally in figure 3.2(d) the wave functions obtained in the CBS calculations are displayed. One of the main purposes of this experiment is trying to prove that the node in the  $\beta$  band actually exists. The feature of the  $\beta$  band, showing a node in the deformation coordinate  $\beta$  should manifest in the particular form of the form factor (obviously also in the transition density). The minimum in the form factor might be a possible signature for the node in the wave function of the  $\beta$  band.

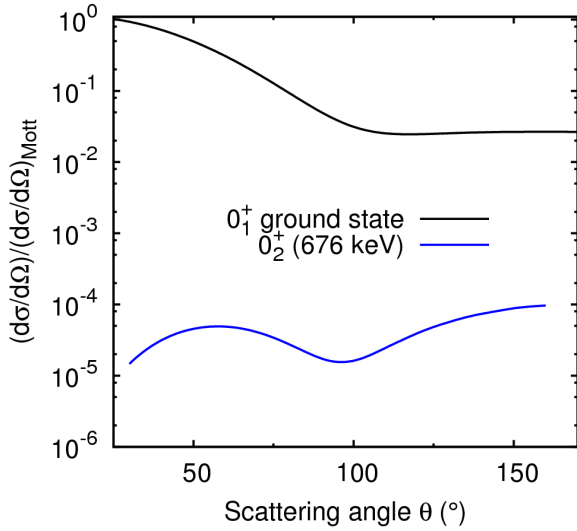
The predicted value for the  $\rho^2(E0; 0_1^+ \rightarrow 0_2^+)$  transition strength in  $^{150}\text{Nd}$  is  $55 \cdot 10^{-3}$  which is a typical value in the region of the X(5) shape phase transitional point. It has already been estimated [Kru08] that with an electron scattering experiment at the S-DALINAC in Darmstadt it



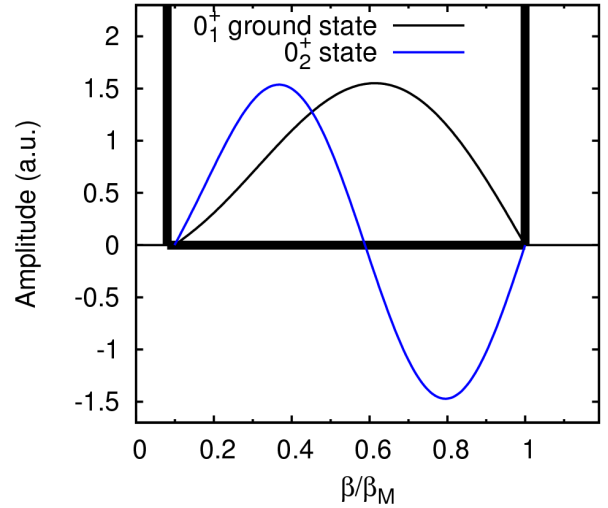
(a) Form factor of  $0_2^+$  state as a function of the momentum transfer  $q$ .



(b) Form factor of  $0_2^+$  state as a function of the scattering angle.



(c) Form factor of the  $0_2^+$  state compared to the elastic form factor for  $E_e = 75$  MeV.



(d) CBS wave functions for the ground state and for the band head of the  $\beta$  band.

**Figure 3.2.:** Correlation between the minimum in the form factor of the  $0_2^+$  state and the node in the wave function of the  $\beta$  band.

should be possible to extract the  $\rho^2(E0; 0_1^+ \rightarrow 0_2^+)$  transition strength in  $^{150}\text{Nd}$ . At typical beam energies of 75 MeV, electron currents of  $1 \mu\text{A}$  and measurements at 4 to 5 different scattering angles (momentum transfers), the beam time should not exceed 2 weeks.



---

## 4 Inelastic electron scattering experiments at the S-DALINAC

---

### 4.1 S-DALINAC and experimental facilities

---

Since 1991 the recirculating superconducting electron linear accelerator S-DALINAC [Ric96] at the Institut für Kernphysik [IKP14] at the TU Darmstadt is in operation. The accelerator and all the experimental facilities were built in the framework of many dissertations and diploma theses and are still modified and improved by bachelor, master and PhD students. Figure 4.1 gives an overview of the S-DALINAC and its experiments. The S-DALINAC once was the first superconducting continuous-wave electron linear accelerator in Europe. Electrons can be either accelerated by a thermionic electron gun ① or by a new source ② that is emitting spin polarized electrons [End11, Fri11]. The superconducting injector ③ with its 3 GHz-cavities allows already experiments with Bremsstrahlung of up to 10 MeV at the Darmstadt High intensity Photon Setup (DHIPS) ④ [Son11]. The electrons can also be bent by 180 degree and pass the main accelerator ⑤ up to 3 times ⑥ to get a final beam energy of 130 MeV and electron currents of up to 20  $\mu\text{A}$ .

Different experimental facilities (see figure 4.1) provide a huge variety of experiments in the field of nuclear structure physics. Experiments with tagged photons can be performed at the photon tagger NEPTUN ⑦ [Sav10]. One of the working horses for the electron scattering experiments at low momentum transfer is the so-called QCLAM spectrometer ⑧ [Die95, Neu97a] where coincidence experiments can be performed [NC97, Str00, Die01, NC02]. This spectrometer is also equipped with a special 180° beam line ⑨ where experiments in transverse kinematics can be preferred [NC99, Rei02, Rye06]. The spectrometer which has been used in this work is the 169° spectrometer ⑩ [Grä78, Wal78, Sch78, Foh78]. It has a much smaller solid angle but due to its dispersion matching beam line, excellent energy resolution can be achieved.

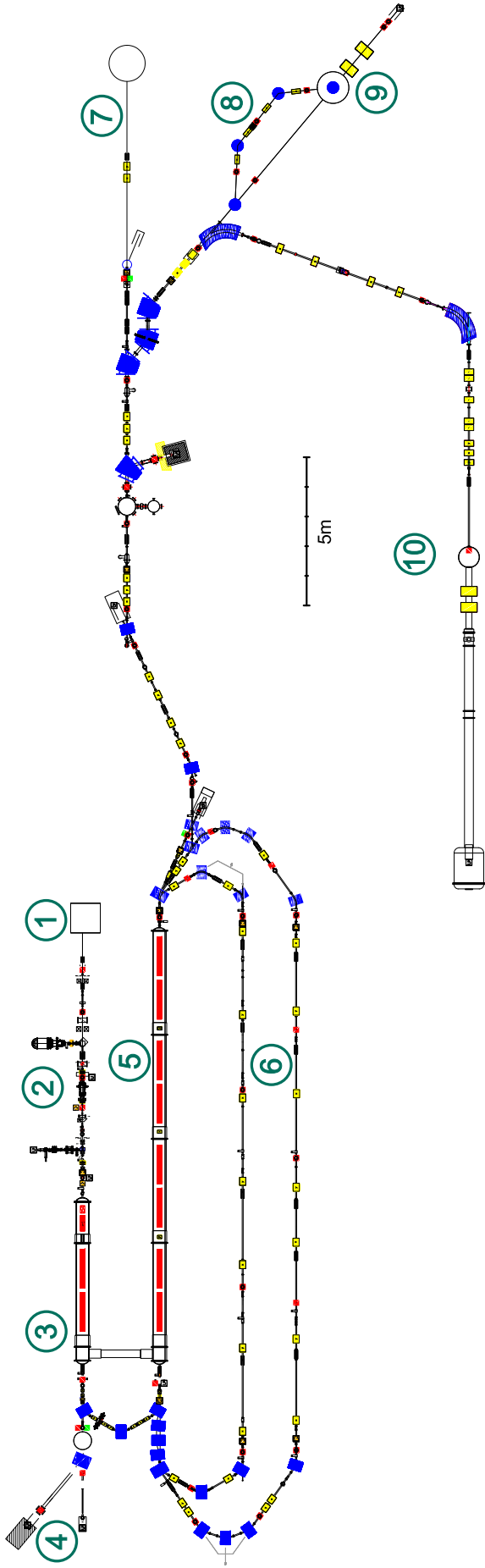


**Figure 4.1.:** Overview of the S-DALINAC with its experimental facilities. ① Thermionic electron gun, ② new source of polarized electrons SPIN, ③ the 10 MeV injector accelerator, ④ the DHIPS facility for  $(\gamma, \gamma')$  measurements, ⑤ main accelerator (40 MeV), ⑥ recirculation beam lines, ⑦ low energy photon tagger NEPTUN, ⑧ 180° beam line, ⑨ QCLAM-Spectrometer, ⑩ 169°-Spectrometer.

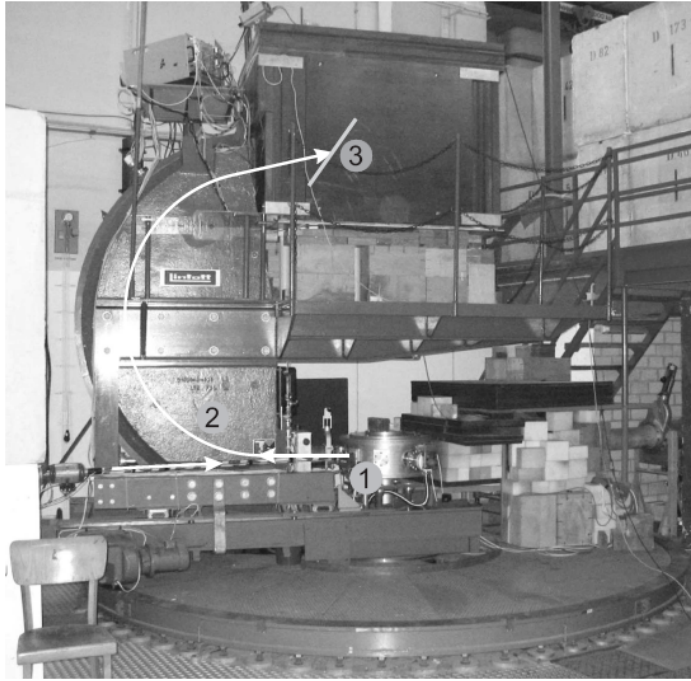


**Figure 4.2.:** Photo of the high energy resolution 169° spectrometer. ① Scattering chamber with the target, ② Dipole magnet and ③ focal plane with detector system.

---

## 4.2 High resolution electron scattering

---

When the accelerated and recirculated electron beam leaves the accelerator hall and enters the experimental hall it is guided to the high-resolution electron scattering facility which consists of a beam transport line and a 169° magnetic spectrometer. The schematic layout of the beam transport system is shown in figure 4.3. The main dispersive elements are two 70° bending magnets E4BM01 and E4BM02 which are placed symmetrically around an energy-defining slit system. This system has two purposes. On the one hand a slit system can be used to cut off unwanted parts of the beam in vertical direction. On the other hand in horizontal direction, a water-cooled copper block with 5 equally spaced slits with a width of 1 mm and a distance of 2 mm is used for tuning the beam to the so-called energy-loss mode. During the beam optimization process when the copper block is inside the beam line, the electron beam is dispersively broadened in horizontal direction and the electrons pass through the separate slits with different energies. The image of the 5 holes can then be observed in the focal plane detector system. The best energy resolution is achieved when the 5 spots are mapped to only one spot on the focal plane.

Since there was not enough space in the experimental hall, the spectrometer has been installed vertically. In order to rotate the the dispersion plane from the beam line to the dispersive plane

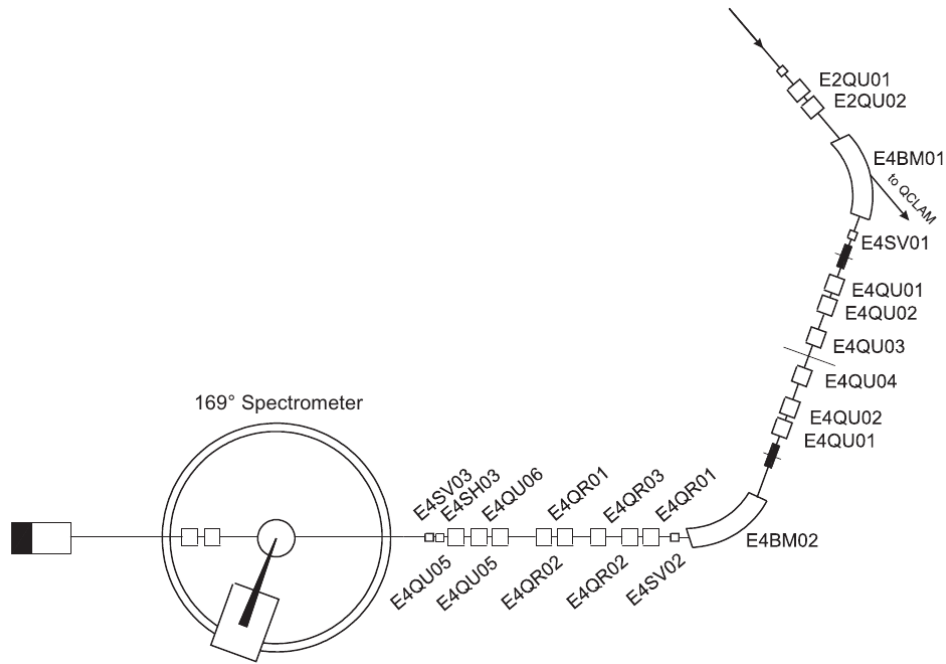


**Figure 4.3.:** Beam line to the high resolution electron scattering facility with the 169° spectrometer.

of the spectrometer (90°) five quadrupoles (labeled as E4QR01-05) are installed. The beam is then guided into the scattering chamber where measurements at angles between 33° and 165° are possible in discrete steps of 12°. A very high percentage of the electrons pass the target which is situated at the center of the scattering chamber and are dumped in a Faraday cup, where the collected beam charge is measured. To reduce the beam divergence behind the target due to multiple scattering, a doublet of two large quadrupoles is installed directly behind the target chamber. Electrons scattered in the solid angle  $\Delta\Omega$  are bent through a dipole magnet and their momentum is analyzed in the focal plane of the 169° spectrometer. The so-called 'magic angle' of  $\pi\sqrt{8}/3 = 169.7^\circ$  was chosen to improve the improve the electron-optical properties of the spectrometer [Wal78]. The focal plane is tilted to 35° relative to the electron orbit to minimize aberration errors. Figure 4.2 shows a photo of the spectrometer. The technical details of the 169° spectrometer can be found in table 4.1.

### 4.3 Focal plane detector system

The focal plane detector system [Len05, Len06] consists of 4 silicon strip detector units, each 6.9 cm long and consisting of 96 silicon strips (channels). The whole focal plane covers a range of 24 cm and the distance between two modules corresponds to a gap of 10.5 strips. The obtained spectra are therefore 415.5 channels wide. Each silicon strip has a thickness of 500  $\mu\text{m}$  and a pitch of 650  $\mu\text{m}$ . The guard ring around the 96 strips and the printed circuit board carrier result in an inactive zone of 7 mm, corresponding to the 10.5 strips, between two adjacent

Energy acceptance:	20 - 120 MeV
Deflection angle:	$169.7^\circ \pm 0.1^\circ$
Radius of central trajectory:	1.0 m
Tilt of focal plane:	$35^\circ \pm 2^\circ$
Dispersion:	3.76 cm/%
Momentum acceptance:	$\frac{\Delta p}{p} = \pm 2\%$
Solid angle acceptance:	$\Omega_{max} \approx 6 \text{ msr}$
Maximum relative energy resolution:	$3 \cdot 10^{-4}$ (FWHM)
Range of scattering angles:	$33^\circ - 165^\circ$ (12 Steps)
Field strength:	0.6 - 4.0 kG

**Table 4.1.:** Some technical details of the high resolution  $169^\circ$  spectrometer.

detectors. Measurements are repeated with slightly different magnetic field settings in order to avoid holes in the spectrum. Figure 4.4 shows a photo of the focal plane detector system. In order to reduce background radiation, a massive radiation shielding has been constructed around it [Bur02a]. As a trigger detector to suppress the background, a 40 cm long plastic

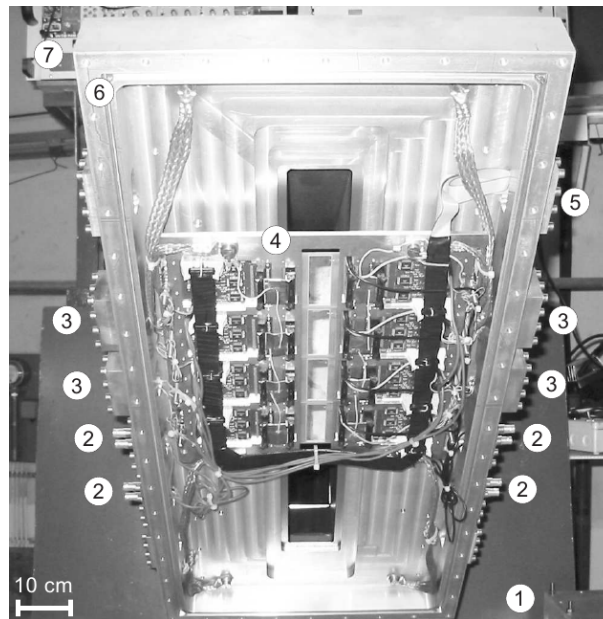


**Figure 4.4.:** Focal plane detector system of the  $169^\circ$  spectrometer. ① Iron yoke of the dipole magnet, ② vacuum connections of bias signals to the preamplifiers, ③ vacuum connections of the preamplifier analog signals, ④ detector unit, ⑤ supply voltage connections and control signals of the preamplifiers, ⑥ detector case, ⑦ readout electronics and high voltage connections. Picture is taken from [Len06].

scintillator with a thickness of 5 mm is used.

---

## 4.4 Modes of operation

---

The 169° spectrometer can be used in two different operational modes. The 'conventional mode' or dispersive mode and the 'energy loss mode' or dispersion matching mode. As an explanation, we start from the common relation between the momentum  $p$  of the electron (in GeV), the bending radius  $R$  (in m) and the magnetic field  $B$  (in T)

$$B \cdot R = 0.3356p, \quad (4.1)$$

and the resulting dispersion of the spectrometer dipole. Dispersion means that electrons with higher momenta have a larger bending radius. One obtains the offset  $\Delta x$  in the focal plane for electrons with the momentum difference  $\Delta p$  from the ideal momentum  $p_0$  and the dispersion

$D_{sp}$

$$\Delta x = D_{sp} \frac{\Delta p}{p_0}. \quad (4.2)$$

---

### 4.4.1 Dispersive mode

---

To measure in the dispersive mode (see left part of figure 4.5), the target is focus point. Due to the different orbit lengths in the magnetic field, electrons with the same momentum  $p$  but different entrance angles in the focal plane are projected to the same point. The spectrometer focuses in a radial direction. This means that the effective energy resolution depends strongly on the momentum resolution of the beam. Typical energy resolutions of  $\Delta E/E \approx 0.5 - 1 \cdot 10^{-3}$  can be reached. The dependence of the electron energy resolution of the beam properties can become a main problem if the accelerator settings are not running stable.

---

### 4.4.2 Energy-loss mode

---

Besides the dispersive mode there exists another mode of operation. In the so-called energy loss mode [Wal78] the dispersion of the extraction beam line to the spectrometer is matched to the dispersion of the spectrometer (see right part of figure 4.5) Applying this mode of operation the energy resolution is independent of the beam resolution because all scattered electrons with the same energy loss in the target are focused on the same point in the focal plane. In order to gain a higher count rate, relatively thick targets with an areal density of up to 20 mg/cm<sup>2</sup> can be used. The energy resolution is mainly determined by the different energy loss of the electrons in the target. In the energy loss mode typical energy resolutions of  $\Delta E/E \leq 3 \cdot 10^{-4}$  can be achieved.

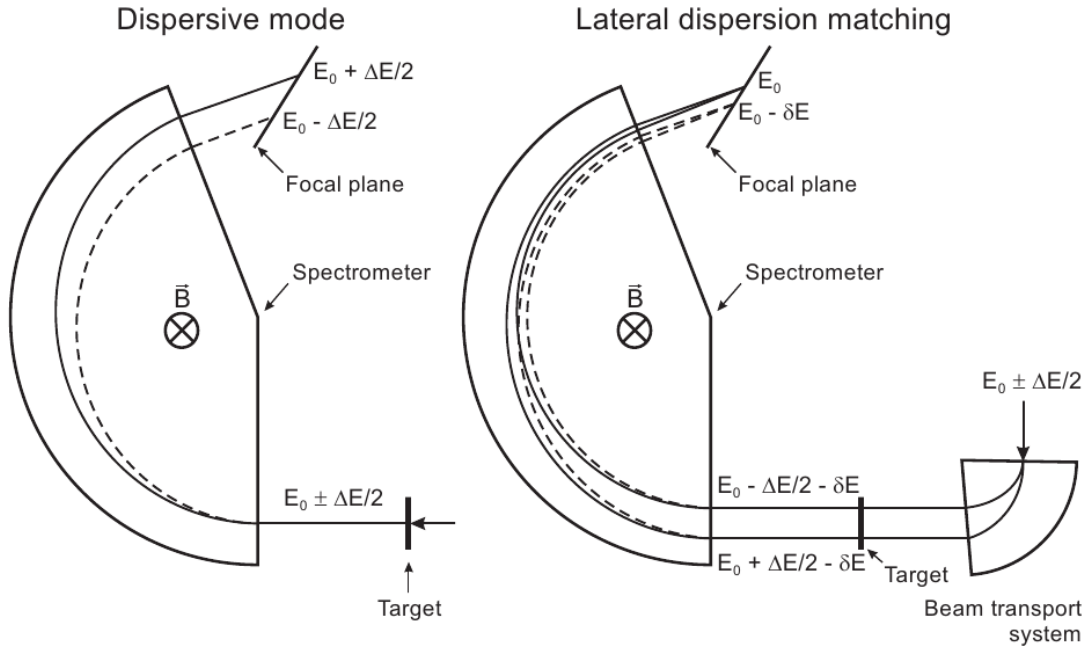


**Figure 4.5.:** Dispersion matching technique. Left: dispersive mode. The position and the angle of scattered particles at the focal plane depend on the initial energy spread  $\Delta E$ , which thereby limits the resolution. Right: lateral dispersion matching. It allows to improve the resolution by spatially spreading the beam spot at the target position according to the dispersion of the beam, matching it to that of the spectrometer. This figure has been taken from [Bur08].

## 4.5 $^{150}\text{Nd}(e,e')$ experiment

The experiment was carried out in late 2013 at the Darmstadt superconducting electron accelerator S-DALINAC. As an electron source, the conventional thermionic electron gun has been used. The electron beam had an energy of 73.9 MeV and typical electron beam currents of 0.8 to 1.5  $\mu\text{A}$  were measured. The energy resolution was between 22 and 30 keV (FWHM)). In this experiment a highly enriched self supporting metallic foil of  $^{150}\text{Nd}$  which was made in Oak Ridge National Lab, has been used. The metallic foil had a dimension of 2 cm by 3 cm and was attached to a typical Lintott target frame made of aluminum. The areal density is 10  $\text{mg}/\text{cm}^2$  with an isotopic enrichment of 96.11%. Table 4.2 gives an overview of the isotopic composition of the target.

Being one of the more reactive lanthanide rare-earth metals, neodymium quickly oxidizes in air. So, special precaution was necessary for the handling of the target. The scattering chamber was filled with argon for mounting/dismounting the target. Despite all the above mentioned safety precautions the elastic line of Oxygen could be observed clearly in every spectrum. Also a very small contamination of argon, which stems from the venting process and carbon that is probably originating from the pump oil, have been observed in the spectra. Figure 4.6 shows

$^{150}\text{Nd}$	96.11 %
$^{142}\text{Nd}$	0.77 % $\pm$ 0.01 %
$^{143}\text{Nd}$	0.39 % $\pm$ 0.01 %
$^{144}\text{Nd}$	0.89 % $\pm$ 0.01 %
$^{145}\text{Nd}$	0.34 % $\pm$ 0.01 %
$^{146}\text{Nd}$	0.89 % $\pm$ 0.01 %
$^{148}\text{Nd}$	0.66 % $\pm$ 0.01 %

**Table 4.2.:** Isotopic enrichment of the  $^{150}\text{Nd}$  target which has been used in this experiment.

a typical spectrum of  $^{150}\text{Nd}$  taken at a scattering angle of 93 degree. The most prominent line at the left hand side is the so-called elastic line, where electrons are scattered elastically. It is common to calibrate the spectra in such way that the elastic line has an excitation energy of 0 MeV. Several inelastic transitions as well as elastic lines coming from the contaminations are indicated.

The most accurate way to determine the electron energy is to calculate the difference of the

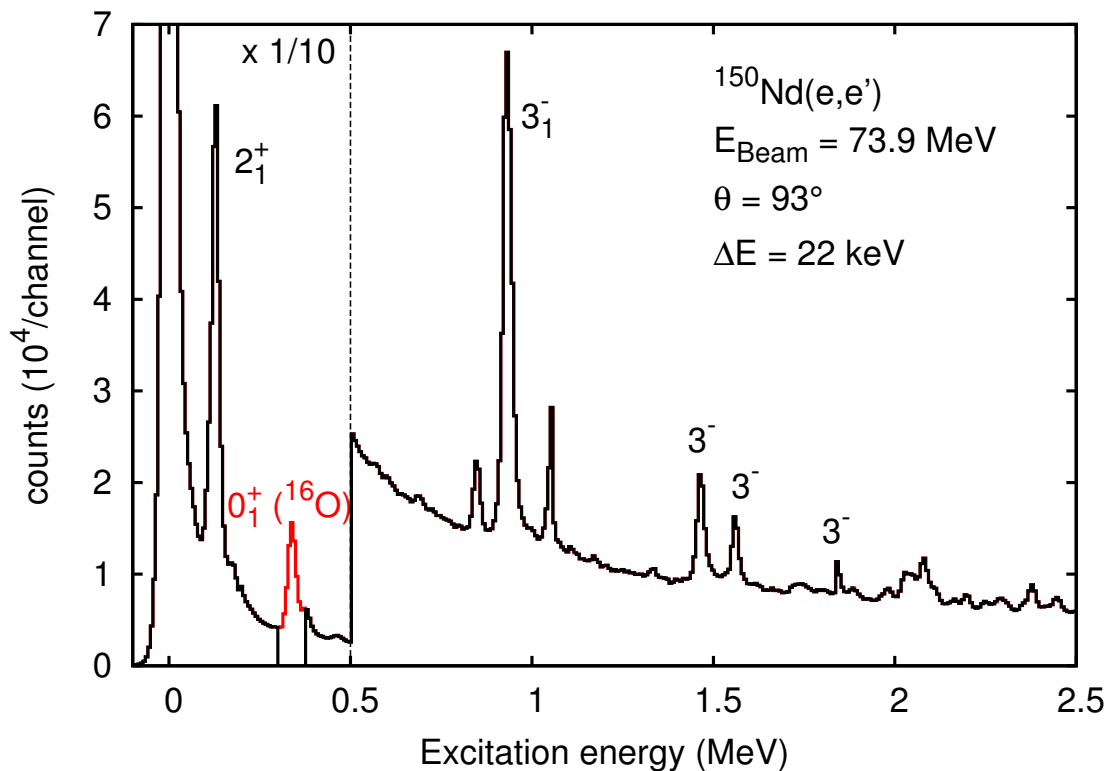


**Figure 4.6.:** Spectrum of the  $^{150}\text{Nd}(e,e')$  reaction at 73.8 MeV, taken at a scattering angle of  $93^\circ$ . The contamination line, originating in elastic scattering off  $^{16}\text{O}$ , is shown in red.

recoil energy of two peaks from different isotopes. This has been done here with the elastic line of argon and neodymium.



---

## 5 Data analysis of the electron scattering data

---

### 5.1 Line shapes

---

For the analysis of the discrete states the line area content  $A_{in}^{exp}$  is determined by adjusting a model function for the line form to the measured spectrum [Hof02].

$$y = y_0 \cdot \begin{cases} \exp \left[ -\ln 2 \cdot (x - x_0)^2 / \Delta x_1^2 \right] & x < x_0 \\ \exp \left[ -\ln 2 \cdot (x - x_0)^2 / \Delta x_2^2 \right] & x_0 < x \leq x_0 + \eta \Delta x_2 \\ A / (B + x - x_0)^\gamma & x > x_0 + \eta \Delta x_2 \end{cases} \quad (5.1)$$

with

$x_0$	maximum energy,
$y_0$	count rate at $x_0$ ,
$\Delta x_{1,2}$	half width at half maximum for $E_x < x_0$ and $E_x > x_0$ , respectively
$\eta$	starting point of the radiative tail in units of $\Delta x_2$ ,
$\gamma$	exponent of the hyperbolic function of the radiative tail.

The parameters  $A$  and  $B$  result from the condition of the continuous differentiable joining of the individual functions to the junctures  $x_0$  and  $x_0 + \eta \Delta x_2$ .

The fit of the model functions to the spectral lines has been performed with the program HDTV [Bra, Bas12]. The parameters  $\sigma_{1,2}$ ,  $\eta$  and  $\gamma$  are fixed for a given spectra, and have been determined by the fit to the dominant elastic line. Then the line positions  $x_0$  and line heights  $y_0$  of the other peaks are fitted simultaneously. The area content  $A_{in}^{exp}$  is calculated as an integral of the function used in the parameterization

$$A_{in}^{exp} = \int_{-\infty}^{x_0 + k \Delta x_1} y(x) dx, \quad (5.2)$$

where  $k$  is the integral cutoff parameter (by default  $k = 5$ ).

---

### 5.2 Energy calibration of the excitation spectra

---

For a comprehensive overview over the off-Yrast low-spin excitations it is necessary to measure the electron scattering spectra up to several MeV. Because of the small momentum acceptance

of the spectrometer (only 4%) one needs to perform the measurement at several settings of the spectrometer magnetic field. Then, it is necessary to make also a calibration measurements for each spectrometer magnetic field setting using other nuclei with known prominent transitions. The calibration could be performed using a direct correspondence between the scattered electron energy  $E'$  and a channel number  $N$ . One has to take into account also the electron energy loss in the target. As a result of an ionization of the electrons in the targets of an effective thickness  $t_{\text{eff}}$  before and after scattering they lose on the average an energy of  $\Delta E [\text{MeV}] = \frac{1}{2} \times 1.4 \times t_{\text{eff}} [\text{g/cm}^2]$ .  $t_{\text{eff}}$  is the effective target thickness. For measurements at the scattering angles  $\theta \leq 141^\circ$  the target is set in transmission geometry (perpendicular to the scattering angle bisector). In this case the electrons have an effective path length  $t_{\text{eff}} = t/\cos(\theta/2)$ , where  $t$  and  $\theta$  are the target thickness and the scattering angle, respectively. Measurements at angles  $\theta > 141^\circ$  are only possible in the reflection geometry. Here, there effective path length of the electrons in the target is  $t_{\text{eff}} = t/\sin(\theta/2)$ .

$$E'(E_i, E_x, \Delta E, M, \theta) = \frac{(E_i - \Delta E) - E_x(1 + \frac{E_x}{2Mc^2})}{1 + \frac{2(E_i - \Delta E)}{Mc^2} \sin^2 \frac{\theta}{2}} - \Delta E = f(N). \quad (5.3)$$

If the spectrometer magnetic field is homogeneous, the function  $f(N)$  is linear. Thus, one gets a quadratic equation for  $E_x$ . Solving that, one obtains an excitation energy as a function of a channel number. This calibration is valid only for a given spectrometer magnetic field setting. The same procedure has to be repeated for other settings.

---

### 5.3 Experimental cross sections

---

The calculation of the experimental cross sections requires the subtraction of the background and a determination of the area  $A_{in}^{exp}$  of the observed lines. The absolute value of the cross sections can be calculated from

$$\frac{d\sigma}{d\Omega} = A_{in}^{exp} \cdot \frac{1}{\Delta\Omega} \cdot \frac{e}{It} \cdot \frac{M}{\rho dx N_A}, \quad (5.4)$$

where  $\Delta\Omega$  is the spectrometer solid angle in (sr),  $It$  the accumulated charge in (C),  $M$  the mass number in (g/mol),  $\rho dx$  the areal density of the target in (g/cm<sup>2</sup>) and  $N_A$  the Avogadro number in (1/mol).

The differential cross section  $d\sigma/d\Omega$  for the excitation of a nuclear state can also be extracted from the measured spectra relative to the elastic cross section

$$\frac{(d\sigma/d\Omega)_{in}}{(d\sigma/d\Omega)_{el}} = \frac{A_{in}^{exp}}{A_{el}^{exp}}, \quad (5.5)$$

Since the electron scattering process is purely electromagnetic and the elastic scattering cross section can be calculated in the framework of Quantum Electrodynamics, one usually determines the inelastic cross section  $\left(\frac{d\sigma}{d\Omega}\right)_{in}$  relative to the elastic cross section  $\left(\frac{d\sigma}{d\Omega}\right)_{el}$ , respectively in terms of the form factors

$$\frac{|F(\theta)|_{in}^2}{|F(\theta)|_{el}^2} = \frac{A_{in}}{A_{el}}, \quad (5.6)$$

where  $A_{el}$  and  $A_{in}$  are the peak areas corrected for the radiative processes, discussed in the next chapter. The elastic form factor  $|F(\theta)|_{el}^2$  were calculated with two different phase shift codes PHASHI [Bäh, Yen54] and DREPHA [Dre, Dre74]. These codes use ground state charge density distributions for  $^{150}\text{Nd}$  which are approximated by three-parameter Fermi distributions. The parameters were taken from reference [Vri87].

---

### 5.3.1 Radiative corrections

---

Bremsstrahlung leads to a radiative tail in the line shape of electron scattering data. To correct for that the area under the peak is integrated up to a cutoff limit  $E_{\text{cutoff}} = x_0 + \Delta E$ . Electrons with an energy loss larger than  $\Delta E = 5 \Delta x_1$  are missed. Therefore, the calculated peak area  $A_{in}^{exp}$  is corrected by multiplying with correction factors for the radiation effects

$$A_{in} = C_{rad} \cdot A_{in}^{exp}. \quad (5.7)$$

The total correction  $C_{rad}$  includes the Schwinger ( $\delta_S$ ), bremsstrahlung ( $\delta_B$ ) and ionization ( $\delta_I$ ) correction

$$C_{rad} = e^{\delta_B + \delta_S + \delta_I}. \quad (5.8)$$

The Schwinger correction is given by

$$\delta_S = \frac{2\alpha}{\pi} \left\{ \left[ \frac{1}{2} \ln \left( \frac{E_0}{\eta^2 \Delta E} \right) + \frac{1}{2} \ln \left( \frac{E'}{\eta \Delta E} \right) - \frac{13}{12} \right] \times \left[ 2 \ln \left( \frac{E_R}{m_0 c^2} \right) - 1 \right] + \frac{17}{16} \right\}, \quad (5.9)$$

where  $E_R$ ,  $E'$  and  $\eta = 1 + \frac{2E_0}{Mc^2} \sin^2 \frac{\theta}{2}$  are the recoil energy, the energy of the scattered electrons and the recoil parameter, respectively.

The bremsstrahlung correction is expressed as

$$\delta_B = \frac{t_{eff}}{X_0 \ln 2} \left[ \frac{1}{2} \ln \left( \frac{E_0}{\eta^2 \Delta E} \right) + \frac{1}{2} \ln \left( \frac{E'}{\eta \Delta E} \right) \right], \quad (5.10)$$

where  $X_0$  is the radiation length

$$X_0 = \frac{716.4 M}{Z(Z+1) \ln(287 Z^{-\frac{1}{2}})} \left[ \frac{\text{g}}{\text{cm}^2} \right] \quad (5.11)$$

A detailed description of these factors can be found in [Mo69].

---

### 5.3.2 Dead time correction

---

During times where the data acquisition is busy, no other events can be processed. To calculate the measurement time and the dead time one uses the expressions

$$T_{meas} [s] = \frac{\text{clkdvd}}{40 \times 10^6} \cdot \text{OnTimeArmed} = 10^{-7} \cdot \text{OnTimeArmed} \quad (5.12)$$

$$T_{dead} [\%] = \frac{\text{OnTimeArmed} - \text{LifeTimeArmed}}{\text{OnTimeArmed}} \cdot 100 \quad (5.13)$$

clkdvd is a constant, depending on the maximum chosen data rate of the detector system. The quantities OnTimeArmed and LifeTimeArmed are quantities indicating the time the data acquisition has been active. Thus, the fitted area under the peak should be corrected on the following dead time correction factor  $C_{dt}$

$$C_{dt} = (1 - T_{dead})^{-1} = \frac{\text{OnTimeArmed}}{\text{LifeTimeArmed}}. \quad (5.14)$$

For calculating the final experimental cross section one has to use this expression for the corrected peak area

$$A_{in}^{cor} = C_{rad} \cdot C_{dt} \cdot A_{in}^{exp}. \quad (5.15)$$

---

## 5.4 Estimation of uncertainties

---

When calculating the experimental cross sections and form factors from the peak areas, systematical and statistical uncertainties were taken into account which contributed to the total uncertainties. In the following, the systematical uncertainties are listed:

- Uncertainty in the determination of the accumulated charge in the Faraday cup ( $\approx 5\%$ ). This value has been obtained by comparing the beam current measured in different Faraday cups throughout the beam line.
- Uncertainty in the determination of the solid angle ( $\approx 2\%$ ). The solid angle is determined by horizontal and vertical slits at the entrance of the dipole magnet. The uncertainty corresponds to the uncertainty in setting the correct vertical and horizontal position of the slits by hand.
- Dead-time correction ( $< 1\%$ ). The dead-time can be measured very precisely, since the elastic scattering process has a huge cross section which is by orders of magnitude larger than in inelastic scattering.
- Target inhomogeneity ( $\approx 3\%$ ).

The largest part of the uncertainties in the form factors originate in the determination of background in the counting statistics. For the elastic scattering and the strong  $2^+$  and  $3^-$  states, the statistical uncertainties were negligible. But in very weak transition like the  $0_2^+$  excitation, uncertainties up to 40% arrived.

---

## 5.5 Experimental Data

---

Figure 5.1 shows all the measured spectra at scattering angles from  $69^\circ$  to  $141^\circ$ . The prominent peaks at 0 MeV (elastic scattering), 0.130 MeV ( $2_1^+$  state), 0.932 MeV ( $3_1^-$  state) and the two  $3^-$  excitations at 1.482 MeV and 1.578 MeV, respectively, have been used for the excitation energy calibration. Due to technical problems, the measurements at  $141^\circ$  could only be performed for one single magnetic field setting, that's why there are still holes from the three blind areas in the focal plane detector system.

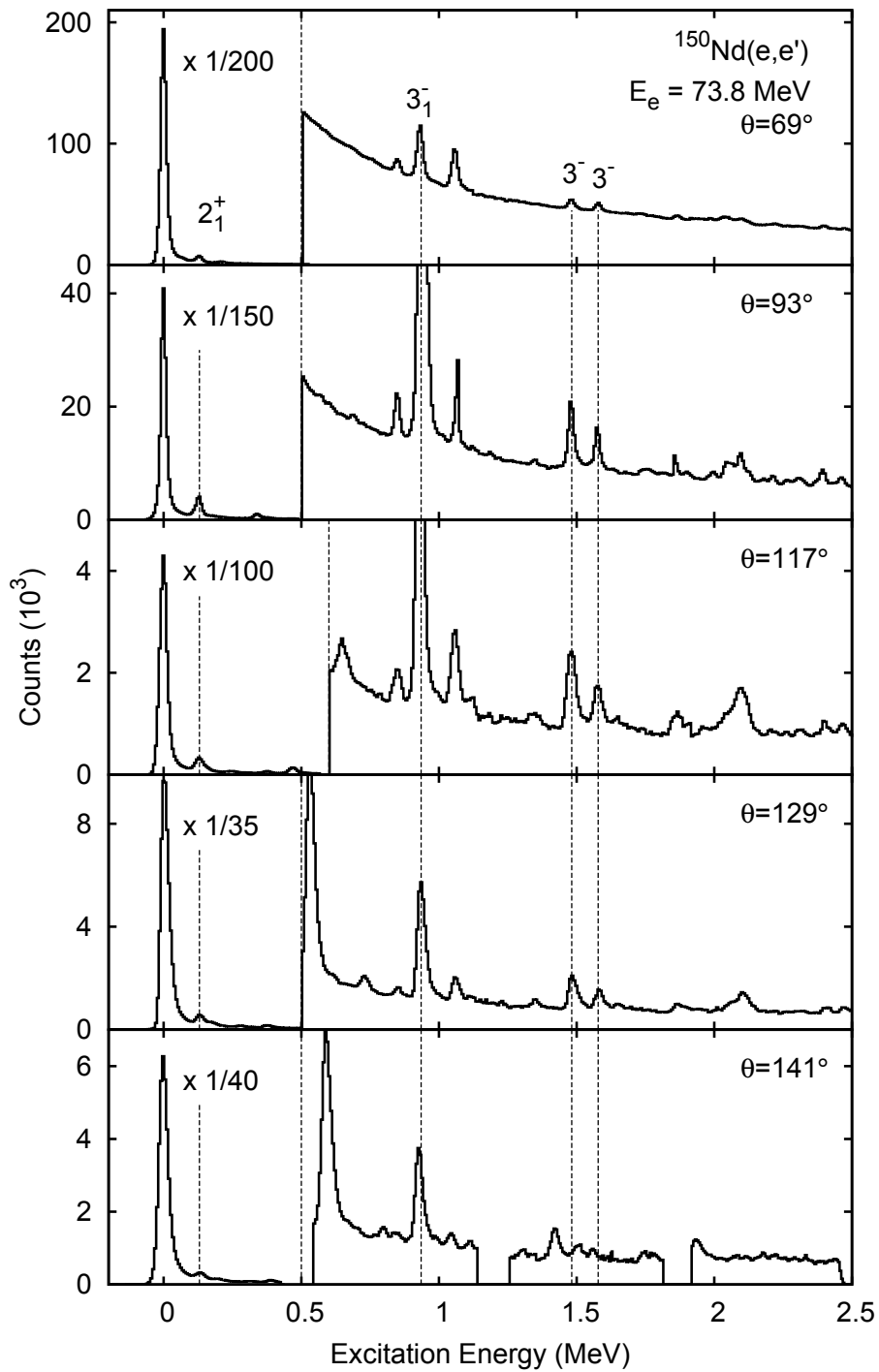


**Figure 5.1.:** Spectra of the  $^{150}\text{Nd}(e,e')$  reaction with an electron energy of 73.8 MeV at the scattering angles of  $69^\circ$ ,  $93^\circ$ ,  $117^\circ$ ,  $129^\circ$  and  $141^\circ$ .

---

## 6 Discussion of the electron scattering data

---

### 6.1 Elastic scattering

---

The experimental elastic form factor for  $^{150}\text{Nd}$  are compared in figure 6.1 to the phase shift analysis codes DREPHA and PHASHI. The two codes agree well with the measured values for the scattering angles  $69^\circ$  to  $129^\circ$ . Due to technical problems, the collected charge in the spectra could not be determined correctly in the  $141^\circ$  data set. Therefore the data setting has not been used in the analysis. The results of the two codes also coincides very well. Since DREPHA can

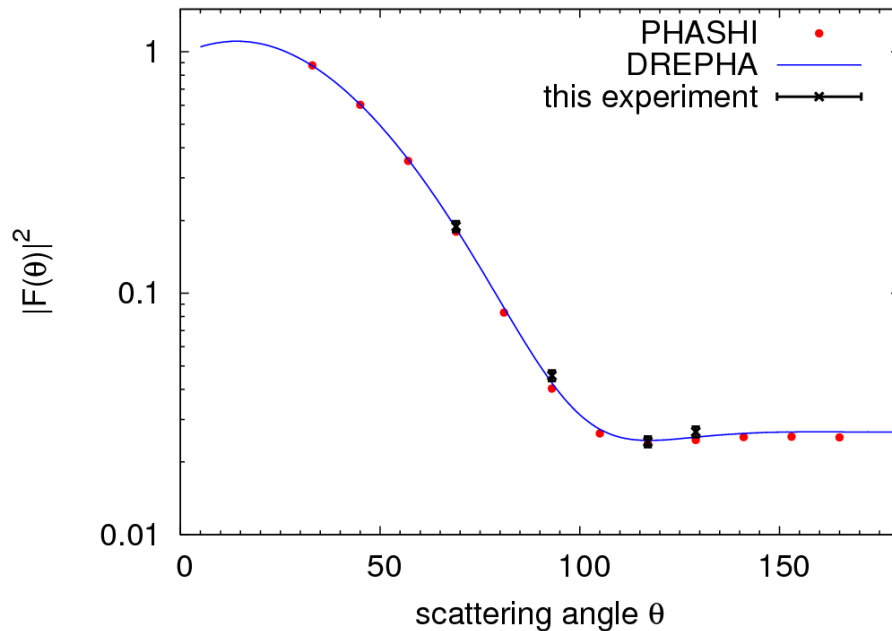


**Figure 6.1.:** Experimental elastic form factor of the  $^{150}\text{Nd}(e,e')$  reaction at  $E_0=73.8$  MeV as a function of the scattering angle compared to the results of the phase shift analysis codes DREPHA and PHASHI.

be used in a more intuitive way, it has been used for further analysis.

---

### 6.2 Electric monopole strength of the $0_1^+ \rightarrow 0_2^+$ transition in $^{150}\text{Nd}$

---

Since the  $0_1^+ \rightarrow 0_2^+$  transition in  $^{150}\text{Nd}$  is very weak, it was not easy to observe the corresponding peak in the excitation energy spectra. At an scattering angle of  $117^\circ$  it was not possible to distinguish the peak from the contamination of  $^{12}\text{C}$  in the target, that showed up at this angle due to kinematical reasons. For the remaining three settings, the fit of the peak area was extremely sensitive to the choice of start parameters for the fit procedure. Another problem was

the fact that the  $0_2^+$  state in  $^{150}\text{Nd}$  is situated at a very low excitation energy, where the elastic line is extremely dominant and the slope of the elastic line shape is very high. Therefore the line shape was fitted and in figure 6.2 the excitation spectrum without the contribution of the elastic line is shown. The elastic line has been subtracted which made the fitting procedure easier. Figure 6.3 finally shows the obtained form factor of the  $0_1^+ \rightarrow 0_2^+$  transition in  $^{150}\text{Nd}$ . Using a

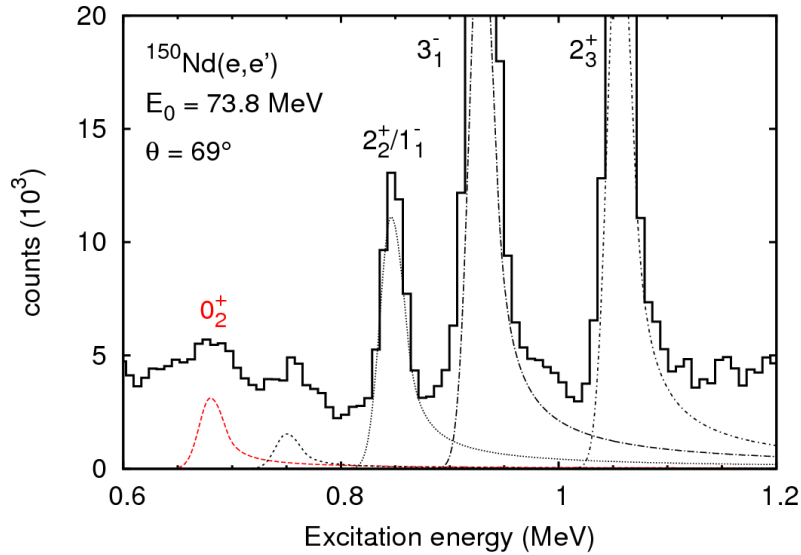


**Figure 6.2.:** Excitation energy spectrum at an scattering angle of  $69^\circ$  where the contribution of the elastic line is subtracted.

$\chi$ -square fit, the experimental form factor data points have been scaled to the theoretical curve shown in figure 3.2(a) or figure 3.2(b). This leads to a E0 transition strength of

$$\rho^2(E0; 0_1^+ \rightarrow 0_2^+) = 38 \pm 25 \cdot 10^{-3}. \quad (6.1)$$

The experimental data points in figure 6.3 seem to follow the first minimum and the second maximum of the theoretical curve. This minimum of the form factor might be a signature of the node in the wave function of the  $\beta$  band. For further proofs of this claim the minimum should be examined in further detail.

### 6.3 Evolution of absolute E0 strengths

In [Bon09] the absolute E0 transition rates have been predicted by the CBS model for the whole transitional path from X(5) to the rigid rotor limit.

With the help of figure 6.4 which is taken from [Bon09] it has been figured out that with increasing  $r_\beta$  (that means increasing potential stiffness) the E0 transition strength goes down. Here, the E0 transition strengths for different angular momenta depending on  $r_\beta$  are shown. All transition strengths are normalized to the  $0_2^+ \rightarrow 0_1^+$  transition for X(5). For  $r_\beta$  approaching unity,



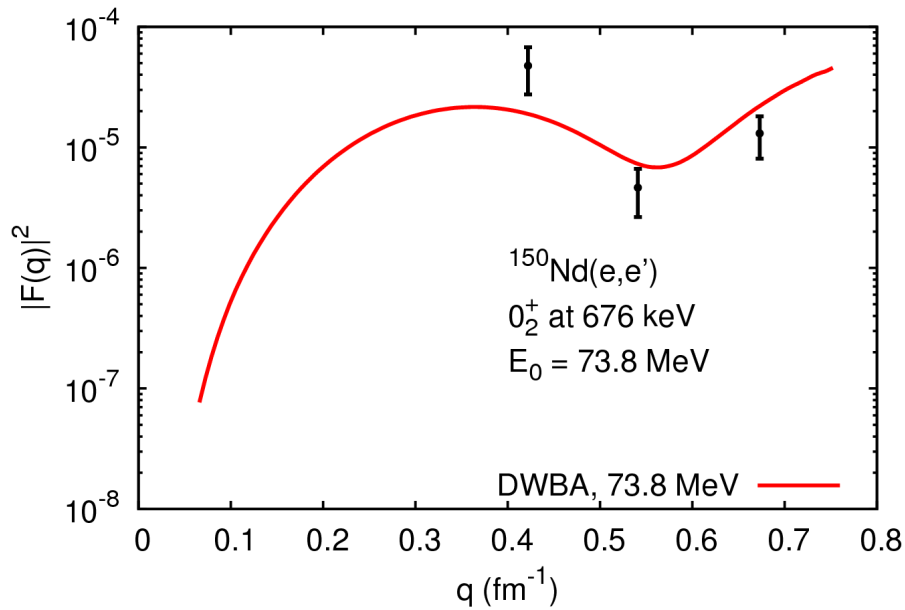


**Figure 6.3.:** Form factor of the  $0_2^+$  excitation in the  $^{150}\text{Nd}(e,e')$  reaction at 73.8 MeV. The solid line represents the scaled form factor from [Shi09]

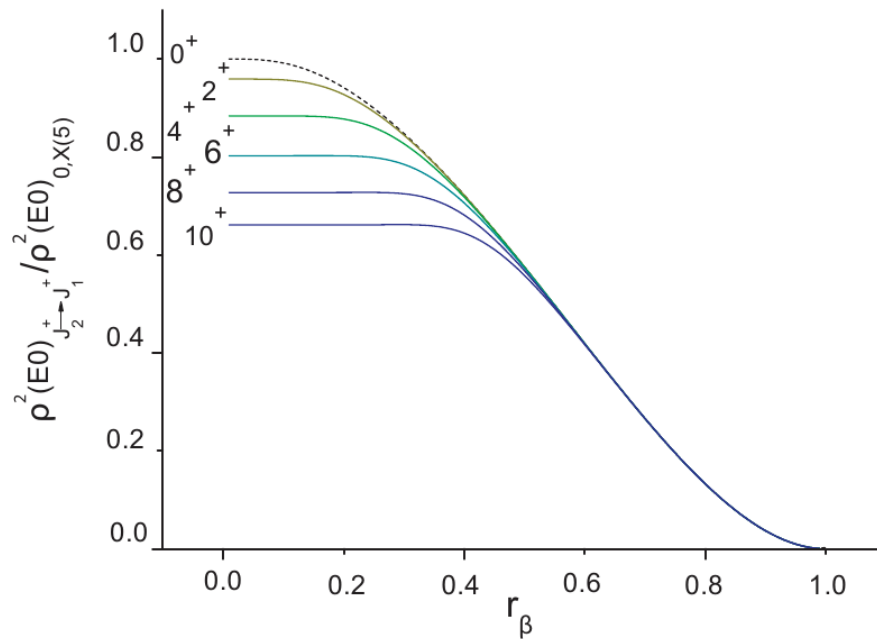


**Figure 6.4.:** Absolute E0 transition rates predicted in the CBS model. This picture has been taken from [Bon09].

all  $E0$  transition strengths drop to zero. In the case  $0^+$  states, the strengths even monotonically decrease with increasing  $r_\beta$ .

Now that another  $\rho^2(E0)$  value has been measured for this particular region, it would be interesting to investigate this claim by a comparison with experimental results. Also the derivation of equation 2.18 in the theoretical introduction supports the need of experimental verification.

### 6.3.1 Stiffness dependence of the $\rho^2(E0)$ transition strengths

Since the CBS parameter  $r_\beta$  is a direct measure for the potential stiffness and the experimental observable  $R_{4/2}$  is monotonically correlated with  $r_\beta$  [Pie04], it would be interesting to investigate the stiffness dependence of the experimentally known  $\rho^2(E0)$  values on the transitional path between X(5) and the rigid rotor limit. The  $\rho^2(E0)$  values in figure 6.5 are taken from [Kib05] and listed in appendix B. The new value for  $^{150}\text{Nd}$ , determined in this work, is also included. Most likely the  $\beta$  band of  $^{166}\text{Er}$  is erroneously assigned. At the critical point ( $r_\beta=0$  and  $R_{4/2}=2.9$ ) the E0 strength shows a maximum and then decreases again with increasing potential stiffness.

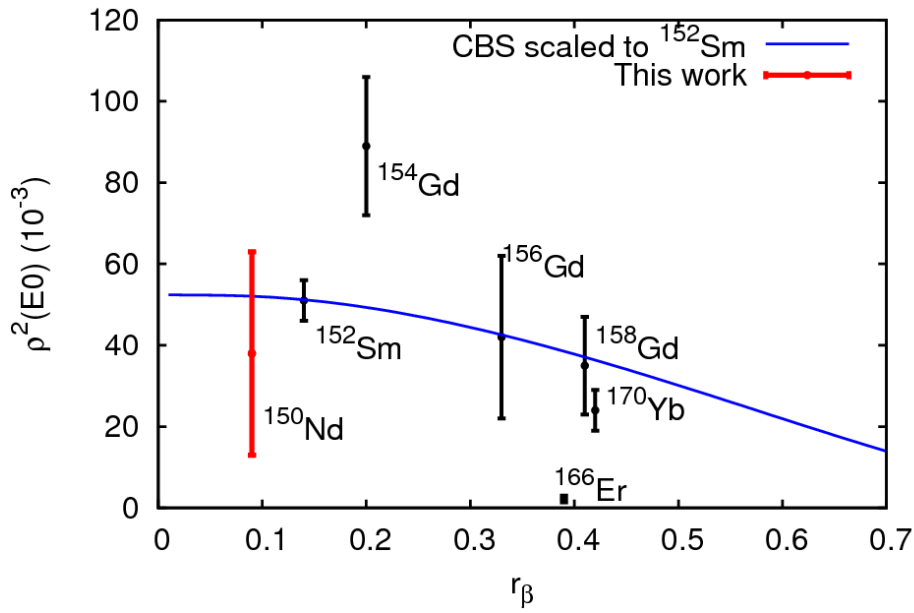


**Figure 6.5.:** Various  $\rho^2(E0)$  values in the shape-phase transitional region as a function of the CBS parameter  $r_\beta$  indicating the potential stiffness. The CBS curve has been scaled to the absolute value of  $^{152}\text{Sm}$ , where the  $\rho^2(E0)$  values is known precisely.

To understand the decrease of the  $\rho^2(E0)$  values as a function of the potential stiffness, figure 6.6 may be taken into consideration. This figure has been taken from [Bon09]. Here, the E0 matrix element from equation (2.32) has been investigated in more detail. All functions of the relative deformation parameter  $b$  which contribute to the E0 transition matrix element ( $0_1^+ \rightarrow 0_2^+$ ) are plotted for  $r_\beta = 0$  (top) and  $r_\beta = 0.5$  (bottom). The matrix element represents the overlap integral of the initial and final wave functions, which are weighted by the square of the relative variable,  $b^2$ . Due to the orthogonality of the wave functions, the overlaps of the initial and final wave functions are equal in absolute size and opposite in sign to the left and to the right of the node of the wave function in the  $\beta$  band. As a consequence, the partial E0 matrix elements on either side of that node have opposite signs while the respective overlap integrals are weighted by  $b^2$ .

The absolute value of the partial  $E0$  matrix element on the corresponding side of that node is indicated by the length of the arrow in figure 6.6. Finally, the difference between these absolute values gives the total matrix elements. Furthermore, the positions of the arrows indicate the root mean square of  $\mathfrak{b}$  weighted by the wave function's overlap on either side of the node. While in the upper graph in figure 6.6 the  $\rho^2(E0)$  values shows a rather high value, the lower graph with a higher potential stiffness obviously indicates a decrease in  $\rho^2(E0)$ .

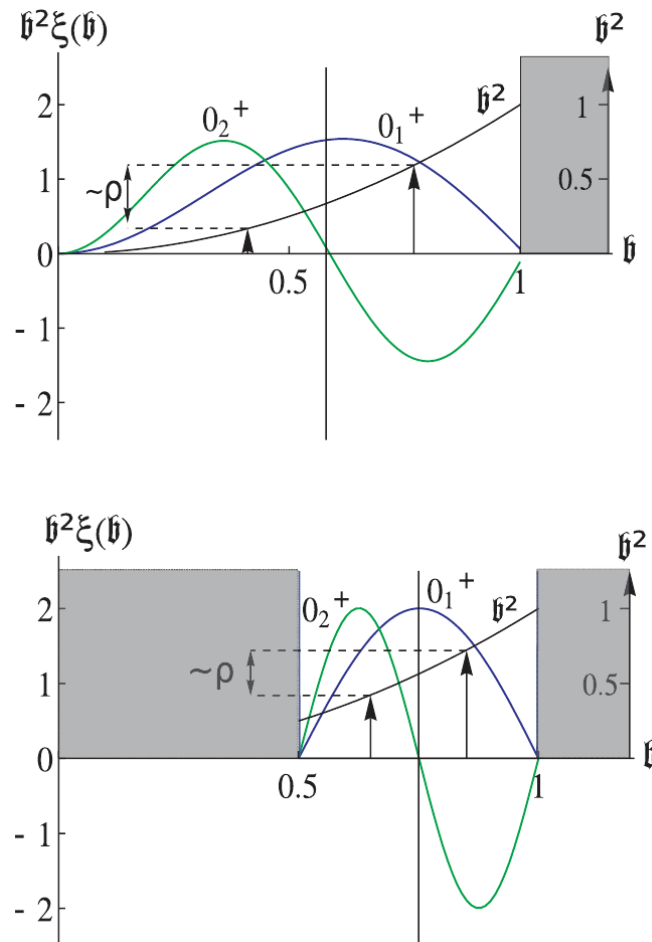


**Figure 6.6.:** Behavior of  $\rho^2(E0)$  transition strengths for the  $0_2^+ \rightarrow 0_1^+$  transition for different values of  $r_\beta$ . Upper graph:  $r_\beta = 0$ , lower graph:  $r_\beta = 0.5$  (high potential stiffness). Picture taken from [Bon09].



---

## 7 Comparison of the CBS rotor model with a macroscopic collective mean field

### Hamiltonian for $^{150,152}\text{Nd}$

---

In this rather theoretical chapter the results of a comparison between the analytical wave functions of the CBS rotor model (see section 2.3) and a collective Hamiltonian based on the relativistic mean field model (see section 2.4), will be presented. The work has already been published [Kru11].

---

#### 7.1 Description of $K=0$ bands and their centrifugal stretching

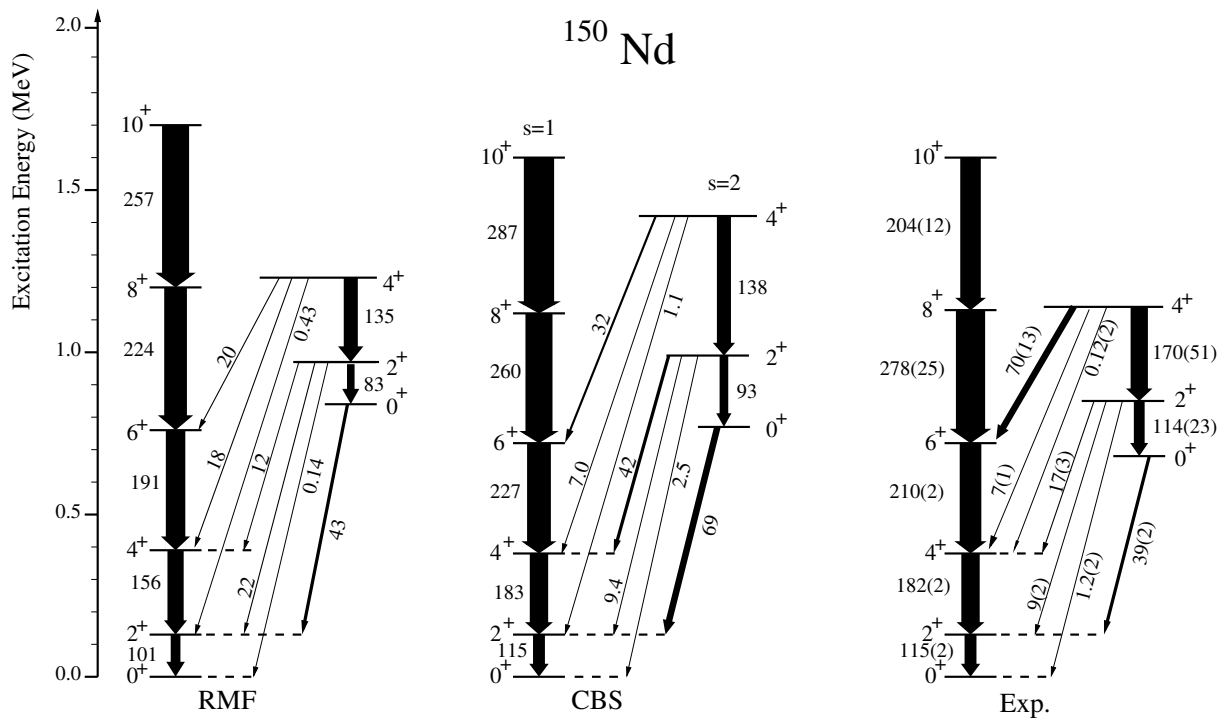
---

Figure 7.1 shows the low lying excitation spectrum of the nucleus  $^{150}\text{Nd}$  [Bag76] in comparison to the two models. For the CBS rotor model we have fitted the structural parameter  $r_\beta$  to the  $4_1^+/2_1^+$ -energy ratio  $R_{4/2}$ . For  $^{150}\text{Nd}$  we used  $r_\beta = 0.078$  and for  $^{152}\text{Nd}$   $r_\beta = 0.35$ . The energy-scale parameter  $\frac{\hbar^2}{2B\beta_M^2}$  [see equation (2.27)] has been fitted to the excitation energies of the  $2_1^+$  states and takes the values of 37.9 keV for  $^{150}\text{Nd}$  and 30.7 keV for  $^{152}\text{Nd}$ . The effective E2 charges of the first order ( $\Delta k = 0$ )-part of the transition operator  $T(E2) = \frac{3}{4\pi}ZeR^2\beta_M(\beta/\beta_M)D_{\mu 0}^2$  [Pie04] have been scaled to the experimental  $B(E2; 2_1^+ \rightarrow 0_1^+)$  values. For the calculations we used  $\beta_M = 0.451$  for  $^{150}\text{Nd}$  and  $\beta_M = 0.471$  for  $^{152}\text{Nd}$ .

For the RMF model we have multiplied the Inglis-Belyaev moments of inertia in equation (2.35) with a common factor  $(1 + \alpha)$  determined in such a way that the calculated energy of the  $2_1^+$  state coincides with the experimental value. This is because the well-known fact that the Inglis-Belyaev formula predicts effective moments of inertia that are considerably smaller than empirical values. For  $^{150}\text{Nd}$  we used  $\alpha = 0.40$  and for  $^{152}\text{Nd}$   $\alpha = 0.57$ . The transition strengths are calculated in the full configuration space using bare charges [Nik09, Li09].

The  $s=1$  ground state band is very well reproduced by the two models. In the microscopic RMF approach the energies differ only by a few percent compared to the experimental energies. In the CBS rotor model the deviation is even less than 0.3 % [Dus05]. In the  $s=2$  band, which is the collective  $\beta$ -band for this nucleus, the rotational structure is very well reproduced in the two models and the deviations in energy primarily result from a mismatch of the rotational moment of inertia by up to 25 %. The  $B(E2)$  intra- and inter-band transition strengths show a satisfactory agreement in both models. Note, that both, energies and  $B(E2)$  values for the excited  $k=0$  band in the CBS rotor model, represent model predictions without any further parameter adjustment.

Figure 7.2 shows the same spectra for the nucleus  $^{152}\text{Nd}$  [Hel92]. In this case, only few data is available. Here, the two models show again a nice agreement in the excitation energies and  $B(E2)$  values for the ground state band, as well as for the  $\beta$ -band. One underlying mechanism at work in the CBS rotor model is the centrifugal stretching of the nucleus which can be classically



**Figure 7.1.:** Low lying energy levels in  $^{150}\text{Nd}$  for the relativistic mean field Hamiltonian (left), the CBS rotor model (middle) and experimental values (right). Energies and  $B(E2)$  values for Exp. and RMF were taken from reference [Li09]. Picture is taken from [Kru11].

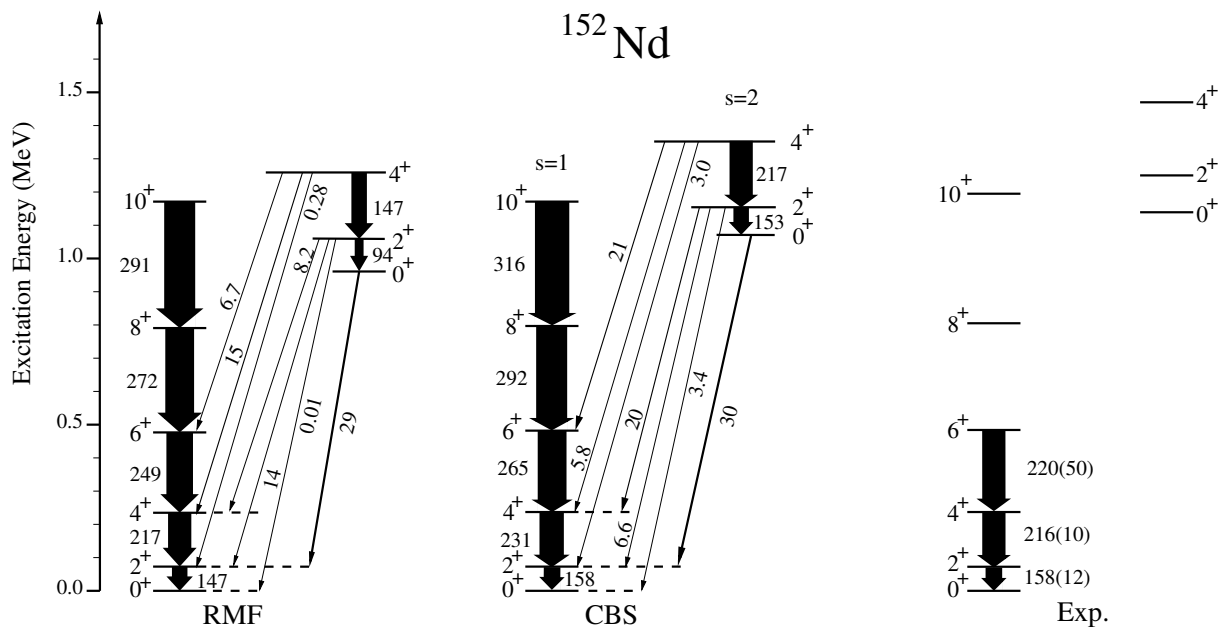


**Figure 7.2.:** Low lying energy levels in  $^{152}\text{Nd}$  for the relativistic mean field Hamiltonian (left), the CBS rotor model (middle) and experimental values (right). Energies and  $B(E2)$ -values for Exp. were taken from reference [Hel92]. Picture is taken from [Kru11].

understood as an increase in the moment of inertia (MoI) as a function of the rotational angular

momentum. In the upper graph in figure 7.3 the evolution of the MoI with spin, here plotted as the relative dynamical moment of inertia (see also [Dus05])

$$\frac{\theta(J)}{\theta(2)} = \left[ \frac{J(J+1)}{6} \right] \frac{E(J=2)}{E(J)} \quad (7.1)$$

is compared to the CBS and microscopic RMF predictions. Both models well agree with the data on the ground state bands of  $^{150,152}\text{Nd}$ .

The stretching for the two models has been calculated for the ground state rotational bands in the nuclei  $^{150,152}\text{Nd}$ . Defining a dimensionless stretching parameter

$$S(J) = \frac{\langle \beta \rangle_{J_i} - \langle \beta \rangle_{0_1^+}}{\langle \beta \rangle_{0_1^+}}, \quad (7.2)$$

one can quantitatively see in the lower graph of figure 7.3, that the two models show a very good agreement on the predicted centrifugal stretching. In this figure the centrifugal stretching goes more or less linearly with the spin, and an increasing potential stiffness means a decrease in centrifugal stretching.

It is remarkable how well the experimental MoI graph in the upper part of the figure correlates with the theoretically calculated stretching parameters in the lower part. The slope for the centrifugal stretching in  $^{150}\text{Nd}$  is for both models approximately  $0.025/\hbar$ . The much stiffer potential in  $\beta$  for  $^{152}\text{Nd}$  creates only a slope of approximately  $0.01/\hbar$ . Looking at the evolution as a function of valence nucleons, the centrifugal stretching decreases approximately by a factor of 2.5, going from the X(5) nucleus  $^{150}\text{Nd}$  to the well deformed rotor  $^{152}\text{Nd}$ .

The agreement of both models in figure 7.3 appears to be worse for  $^{150}\text{Nd}$  than for  $^{152}\text{Nd}$ . However, the disagreement between the models simply scales with the size of the effect. In  $^{150}\text{Nd}$  the dynamical MoI for the  $10_1^+$  state is 49 % larger than the one for the  $2_1^+$  state. The RMF model predicts an increase of 40 %, only, i.e., underestimates this increase by about one fifth of its size. In  $^{152}\text{Nd}$  the dynamical MoI for the  $10_1^+$  state is 11 % larger than the one for the  $2_1^+$  state. Here, the RMF model predicts an increase of 14 %, i.e., again, at slight variance to the data.

---

## 7.2 Comparison of the collective wave functions

---

Figure 7.4 shows wave functions of the ground state bands in  $^{150}\text{Nd}$  and  $^{152}\text{Nd}$  as a function of  $\beta$ . The vertical bold lines in the first and third subfigure represent the potential boundaries of the square-well CBS potential. The vertical lines inside the wave functions represent the centroid of each wave function. Comparing these nuclides, one can easily see the similar amount of

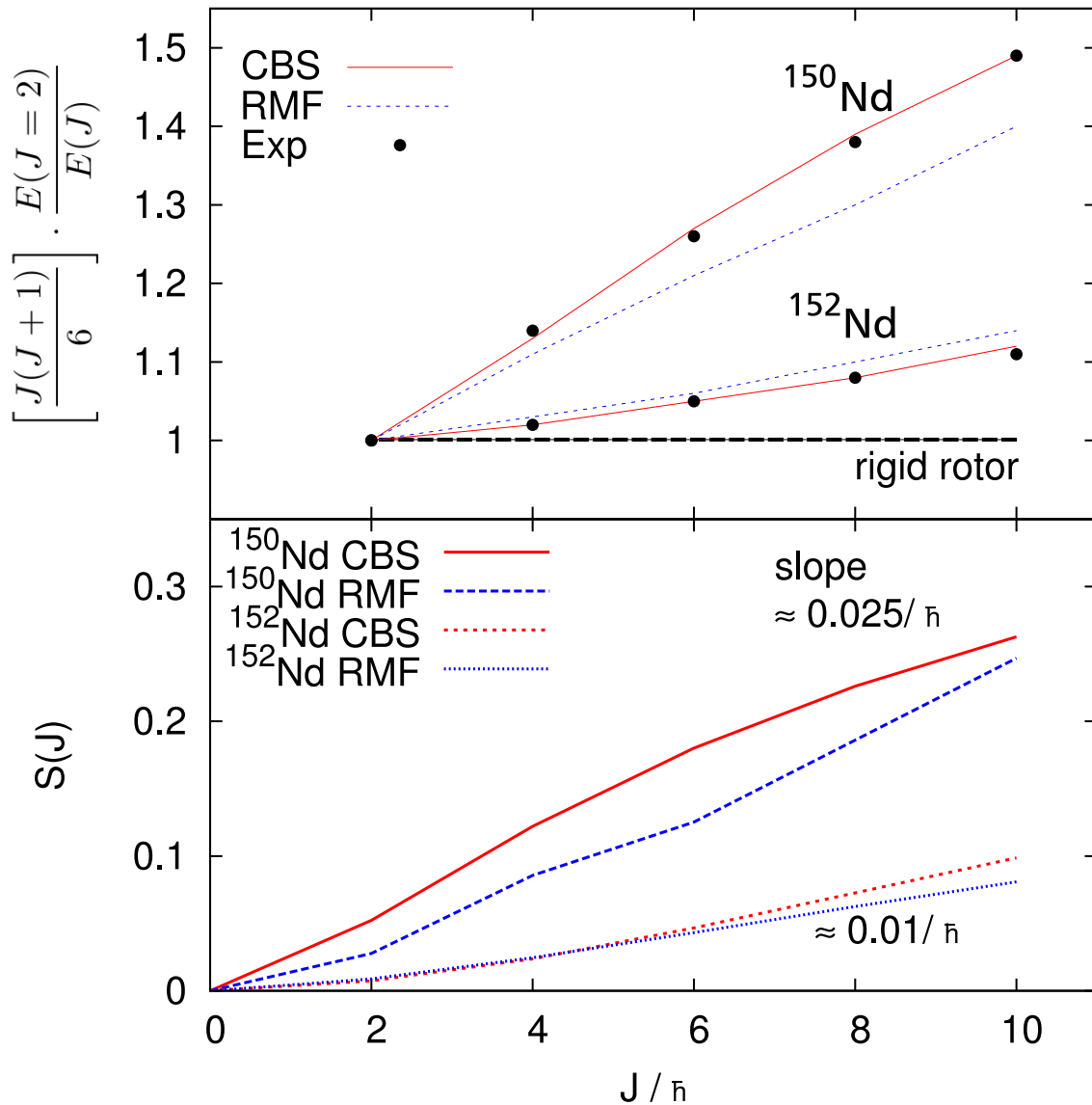


**Figure 7.3.:** Upper graph: Experimental Moments of Inertia and theoretical predictions for the ground state band in the nuclei  $^{150,152}\text{Nd}$ . lower graph: Comparison of the centrifugal stretching parameter  $S(J)$  in  $^{150,152}\text{Nd}$  for the two models as a function of spin. Picture is taken from [Kru11].

centrifugal stretching in the two models. The fact, that the potential stiffens with increasing neutron number can also be seen by comparing the upper and the lower two subfigures. The wave functions of the rotational nucleus  $^{152}\text{Nd}$  are more compressed and shifted towards a larger average deformation.

Figure 7.4 and 7.5 indicate that just a very small fraction of the wave functions computed microscopically in the relativistic mean field model turns out to lie outside of the CBS square well potential walls. In fact, the wave functions of the two models are very similar. They almost exactly show the same amplitude as well as the same centroid for the ground state band in  $^{150}\text{Nd}$  and  $^{152}\text{Nd}$ , respectively.



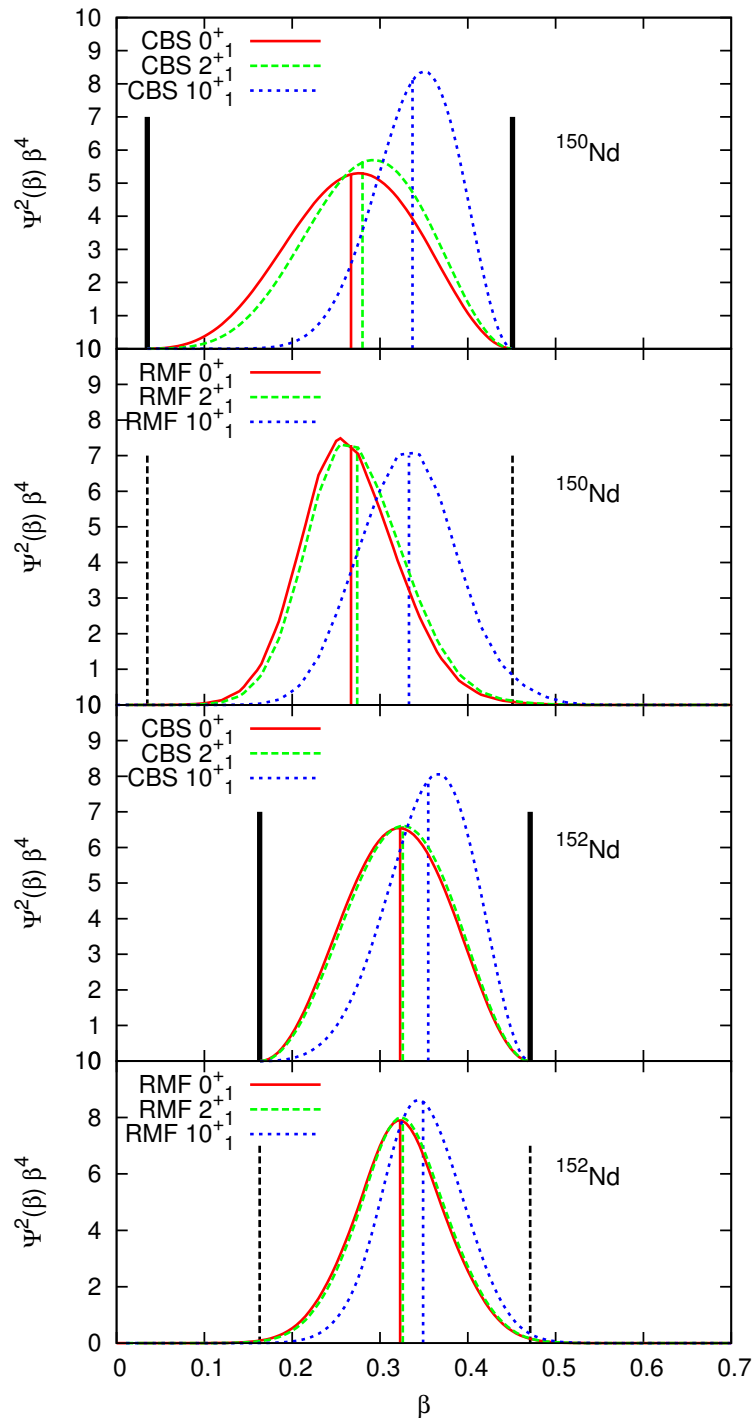


**Figure 7.4.:** Wave functions of the ground state band in  $^{150,152}\text{Nd}$  for the CBS rotor model and the relativistic mean field model. The black borders show the potential walls in case of the CBS potential. Picture is taken from [Kru11].

Figure 7.5 shows the wave functions of the  $\beta$ -band heads. They have one node in the deformation coordinate  $\beta$ . One can clearly see the large overlap of the wave functions between the two models. The centroids of the two peaks in the wave functions of the  $\beta$ -band head almost exactly

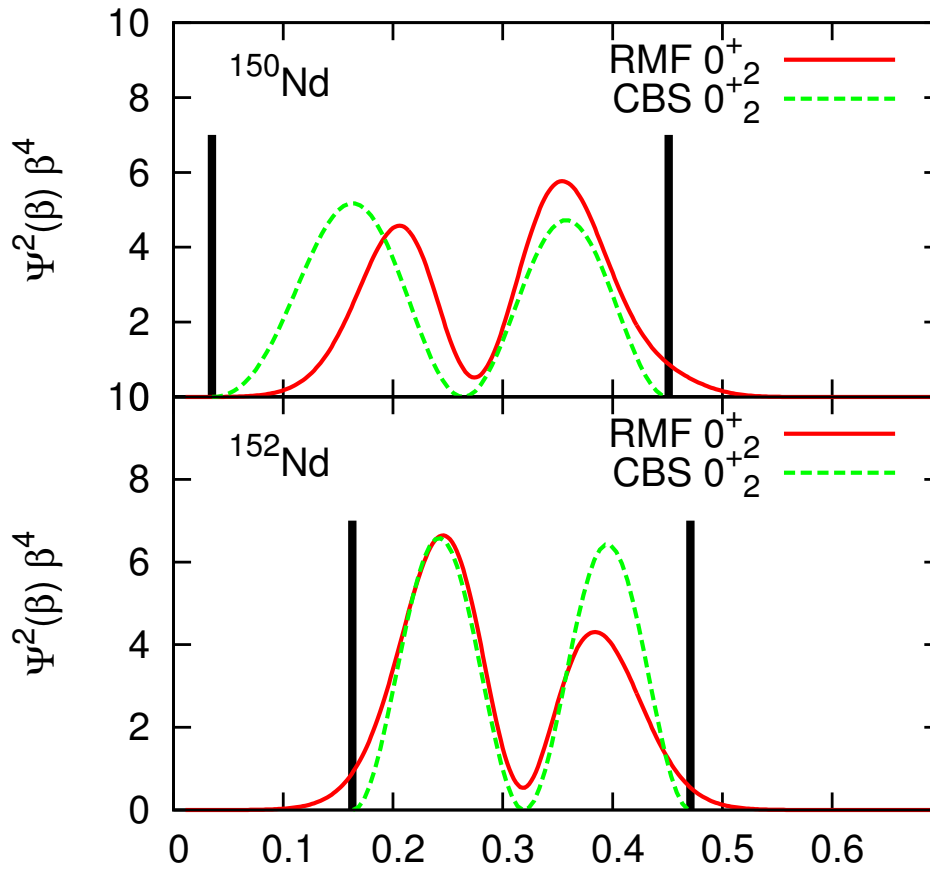


**Figure 7.5.:** Wave functions of the band heads of the  $\beta$ -band in  $^{150,152}\text{Nd}$ . The black borders show the potential walls in case of the CBS potential. Picture is taken from [Kru11].

coincide in the case of  $^{152}\text{Nd}$ . However, the shapes of the wave functions in the  $\beta$ -band differ slightly for both models. Here, the CBS rotor model shows two peaks in the  $\beta$ -band that have almost the same amplitude whereas the microscopic RMF model produces a smaller peak for the waist of the wave function at larger deformation than for the waist at smaller deformation.

For the case of  $^{150}\text{Nd}$  the difference between the prediction of the models for the  $0_2^+$  wave function is slightly larger than for the more rotational nucleus  $^{152}\text{Nd}$ . The top of figure 7.5 shows, that the amplitudes of the two waists of the wave functions are very similar, and the centroids of the second waist are close, but here, the first maxima of the wave functions occur at different deformations. For this example the RMF potential is more repulsive for small deformations than the CBS potential, see figure 1.2, and hence, the RMF wave function is reduced for lower  $\beta$  in comparison to the CBS rotor model.

---

## 8 Conclusion and Outlook

---

Electron scattering experiments at the S-DALINAC in Darmstadt have been performed in order to extract the electric monopole transition strength  $\rho^2(E0; 0_1^+ \rightarrow 0_2^+)$  for the transitional nucleus  $^{150}\text{Nd}$ . The experimental form factor of this transition has been scaled to a macroscopic model prediction so that in a model-dependent analysis the value of  $\rho^2(E0; 0_1^+ \rightarrow 0_2^+) = 38 \pm 25 \cdot 10^{-3}$  was obtained. The experimentally obtained form factor follows the theoretical predictions, e.g. the first minimum of the form factor which might be a signature for the node in the wave function of the  $\beta$  band, has been seen. This needs further evaluation in terms of a very precise determination of the form factor. Therefore a much better energy resolution and more data points in the particular momentum transfer range is required.

Since the experimental uncertainties are still rather high, due to the very low cross section of this particular state, it is planned to continue this experiment at lower momentum transfer by using electron energies of 35 MeV to 40 MeV. Reducing the electron energy by a factor of two, enhances the absolute energy resolution of the spectrometer by the same amount.

Once, this experimental method is established, it will be used to measure the  $\rho^2(E0; 0_1^+ \rightarrow 0_2^+)$  for other nuclei in the vicinity of the shape phase transitional point. A good candidate to start with, would be  $^{152}\text{Sm}$  because of the already known  $\rho^2(E0; 0_1^+ \rightarrow 0_2^+)$ . Also  $^{154}\text{Sm}$  is an interesting option, where the  $\rho^2(E0; 0_1^+ \rightarrow 0_2^+)$  could not yet be determined and  $^{154,156}\text{Gd}$ , where the value is known with very large uncertainties.

Since the relativistic mean field model gives predictions about the evolution of the  $\rho^2(E0; 0_1^+ \rightarrow 0_2^+)$  values, it would be very interesting to have also predictions for transition densities from this model. First considerations in terms of utilizing the generator coordinate method have been done already [Vre] and results will be available in the near future.

Furthermore, a comparison between the analytical wave functions of the CBS rotor model and a microscopic Hamiltonian based on the relativistic mean field model has been performed for the low lying states in the ground-state band and  $\beta$ -band of the nuclei. A remarkable similarity of the two models in energies, intra- and inter-band  $B(E2)$ -values and centrifugal stretching has been observed. In particular, the ansatz in the CBS model of an outer potential wall that stays almost constant with a varying number of valence neutrons and an inner wall that shifts to higher deformations has been microscopically justified for the given example of the isotopes  $^{150,152}\text{Nd}$  near the shape phase transitional point. In both compared models, the position of the outer potential wall seems to be almost independent of a transition from a spherical to an axially symmetric shape of the nucleus while the change in structure as a function of nucleon number is dominated by the change of the potential at small deformation.

---

Very recently a derivation for the transition density for the  $2_1^+$  state ( $E_x = 130.21$  keV) which is a member of the ground state rotational band, became available [Jolb]. It would be very interesting to compare the theoretical form factor with the experimentally obtained form factor from this experiment.

---

**Part II.**

**Low-energy dipole strength  
in  $^{154}\text{Sm}$**

---



---

## 9 Introduction

---

Many-body fermionic quantum systems like the atomic nucleus provide a huge variety of collective and non-collective phenomena. A good way to test the electric and magnetic response of such quantum systems is to excite them with electromagnetic or hadronic probes and investigate their behavior. In nuclei, these collective excitations can be classified by the transfer of angular momentum ( $\Delta L$ ), spin ( $\Delta S$ ) and isospin ( $\Delta T$ ) [Har01]. While monopole ( $\Delta L = 0$ ), dipole ( $\Delta L = 1$ ) and quadrupole ( $\Delta L = 2$ ) modes show a compact structure as a function of excitation energy, resonances with higher  $\Delta L$  are distributed over much larger excitation energy regions [Har01, Spe81]. Concerning the isospin degree of freedom, the resonances can be classified in either **isoscalar** ( $\Delta T = 0$ ) modes, where neutrons and protons move in phase, or **isovector** ( $\Delta T = 1$ ) modes, where neutrons and protons oscillate out of phase. Similar to the oscillation in the isospin space, oscillation in spin space may occur when nucleons with spin up and spin down are excited either in phase ( $\Delta S = 0$ ) or out of phase ( $\Delta S = 1$ ). The latter class of excitations is referred to as **spinflip** excitation.

---

### 9.1 Electric Resonances

---

The investigation of the electric dipole response in nuclei has been started many years ago with the discovery of the so-called giant dipole resonance (GDR) in 1947 by Baldwin and Klaiber [Bal47]. Since then extensive studies in different areas of the nuclear chart have been performed with many probes. Today an almost clear picture of the electric dipole response has been established. Electric dipole excitations can be divided into three groups which can be seen in figure 9.1. The upper panel shows the case of spherical nuclei, whereas in the lower panel the case of deformed nuclei is shown: The low-lying two-phonon state, the pygmy dipole-resonance (PDR) and the giant dipole resonance (GDR).

At low excitations (below 5 MeV) in spherical nuclei, a strong isolated electric dipole excitation occurs, which is interpreted as a member of a quintuplett of states ( $J^\pi = 1^-, \dots, 5^-$ ). It originates in the coupling of  $[2^+ \otimes 3^-]_{1^-}$  [And01]. The term phonon describes in this context low-energy collective surface vibrations of the nucleus. For deformed nuclei, this isolated excitation eventually shows fragmentation [Zil91]. Above the neutron separation threshold  $S_n$ , the isovector giant dipole resonance (IVGDR or GDR) is situated, exhausting the major part of the electric dipole strength [Har01]. It appears as a broad structure typically in the excitation energy range between 10 and 20 MeV. In the hydrodynamical model, the GDR is explained as a collective

oscillation of all protons against all neutrons in the nucleus. The centroid energy of the GDR can be estimated with the relation:

$$E_x = 31.2 \text{ MeV} \cdot A^{-1/3} + 20.6 \text{ MeV} \cdot A^{-1/6}. \quad (9.1)$$

In deformed nuclei, a splitting of the GDR which is caused by the different frequencies of oscillation along the long and short axes, has been observed in experiments [Ber75] (see also lower panel in figure 9.1). Also in the low-energy region of the  $[2^+ \otimes 3^-]_{1-}$  two-phonon states, a splitting in  $K = 0$  and  $K = 1$  parts have been observed for deformed nuclei [Don66]. At ener-

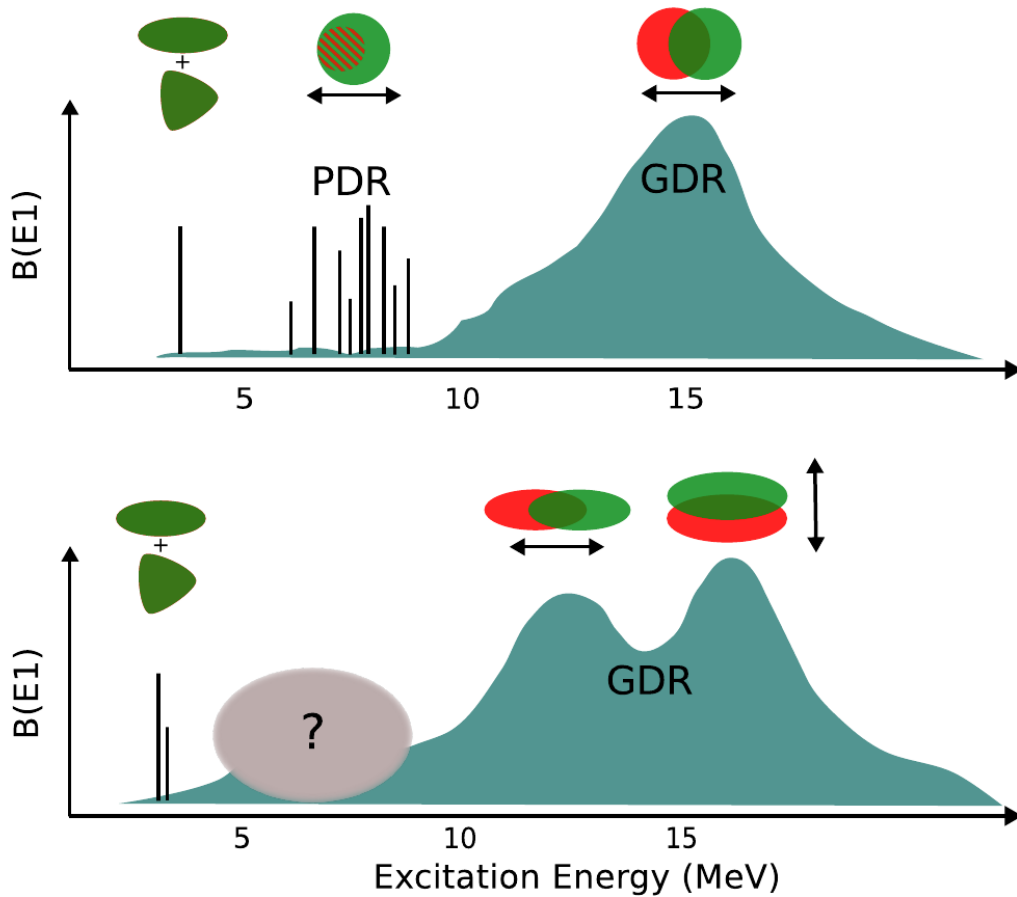


**Figure 9.1.:** Schematic picture of the electric dipole excitations for typical spherical nuclei (upper panel) and typical deformed nuclei (lower panel).

gies between the two-phonon state and the GDR, the so called pygmy dipole resonances (PDR) is situated. An extensive review article about experiments to the PDR in spherical nuclei can be found in [Sav13]. A common interpretation of the PDR is that it arises from the oscillation of an isospin-saturated  $N \approx Z$  core against the excess neutrons. While in spherical nuclei a huge amount of experiments concerning the nature and systematics of the PDR have been performed it is not yet fully understood. For deformed nuclei, the situation is even worse, because almost no experimental data has been taken. In [Tor14] first hints of a double-hump structure of the



PDR in the heavy deformed nucleus  $^{238}\text{Np}$  have been reported. Here, a  $^{237}\text{Np}(p,d)^{238}\text{Np}$  has been performed and with the so-called Oslo Method [Sch00, Lar11], the  $\gamma$  strength function (GSF), which is directly related to the deduced dipole strength distribution, has been obtained. No interpretation for the double-hump structure has been given so far. Likewise, very recently a double structure in the PDR has been observed in  $^{195,196}\text{Pt}$  [Gia14], where they demonstrate, that these resonances exhaust a significant part of the total GSF.

In the last decade, the relevance of knowing the properties of the GDR became more important, since the PDR is assumed to be correlated with the neutron thickness [Pie10, Rei10]. Thus, the density dependence of the symmetry energy in the equation of states (EoS) for neutron-rich matter can be constrained, which is necessary for the description of neutron stars [Tam11]. It has also been reported that the PDR may have an impact on neutron capture rates in the r-process nucleosynthesis [Gor98].

---

## 9.2 Magnetic Resonances

---

In heavy nuclei at excitation energies of about  $1 \hbar\omega$  the so called spin- $M1$  resonance appears. In years of intense studies it has been found out that the centroid energy of this resonance scales approximately with  $40 \cdot A^{-1/3}$  [Fre89, Fre90]. Figure 9.2 shows that the strength is distributed in a double hump structure with an isoscalar part at lower excitation energies and an isovector part at higher excitation energies [Hey10]. Difficulties occur due to the presence of quenching and the lack of data in the heavy deformed mass region. The experimental data for the systematics shown in figure 9.2 have been taken in the early 1990s in a proton scattering experiment with polarized protons at a bombarding energy of 223 MeV at forward angles up to  $2.8^\circ$  performed at the TRIUMF facility in Canada. Figure 9.3 demonstrates the difficulties of the analysis [Wör94]. One assumption made was that the entire  $E1$  strength entering the analysis is described by the giant dipole resonance, i.e., the possible existence of a pygmy dipole resonance was neglected. The other problem was that the resonance structures are built on top of a huge background that originates from quasi-free scattering due to the fact that the experiment has been performed at non-zero scattering angles. A decomposition of the spectrum into contributions of the isovector giant dipole resonance (IVGDR, horizontally hatched), spin- $M1$  resonance (black, low  $E_x$ ) and the isovector giant quadrupole resonance (IVGQR, black, high  $E_x$ ) and a background from quasifree scattering (lower smooth line) is shown.

The interpretation of the double-hump structure of the spin- $M1$  resonance is contradictory. While some calculations suggest an explanation based on a separation of the proton and neutron  $1p-1h$  states, others explain it as a separation into isoscalar and isovector strength [Zaw90, Cos92, Sar96, Hil98].

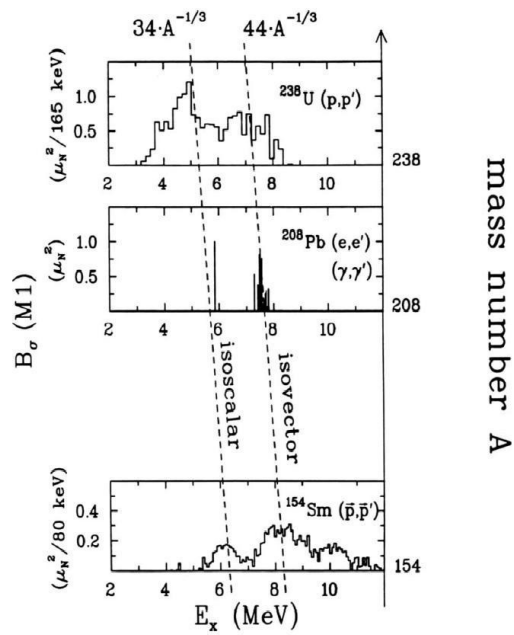


**Figure 9.2.:** Systematics of the spin- $M1$  resonance in heavy deformed nuclei measured at TRIUMF [Hey10].

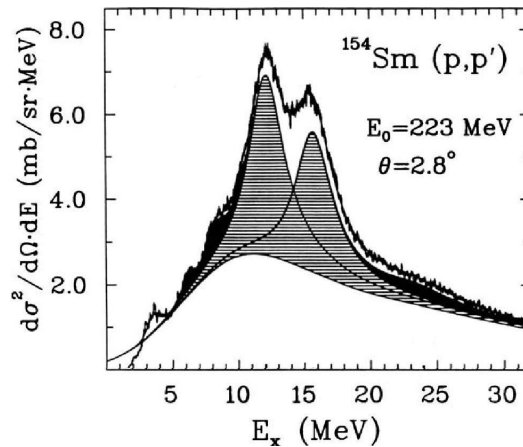


**Figure 9.3.:** Double-differential cross section of the  $^{154}\text{Sm}(\vec{p}, \vec{p}')$  reaction measured at  $\theta = 2.8^\circ$  at TRIUMF [Hey10, Wör94]. A decomposition of the spectrum into contributions of the IVGDR (horizontally hatched) spin- $M1$  resonance (black, low  $E_x$ ) and the IVGQR (black, high  $E_x$ ) and a background from quasi-free scattering (lower smooth line) is shown. From Ref. [Hey10].

---

### 9.3 Separation of $E1$ and $M1$ : New experimental approaches

---

Recently the method of polarized proton scattering at exactly  $0^\circ$  has become available and this provides a new tool to investigate this intriguing physics with a clearer view. At the Research Center for Nuclear Research (RCNP) in Osaka one is able to perform polarized proton scattering at  $0^\circ$  at an intermediate proton energy of 300 MeV. This is optimal for spin-isospin excitations as the central term of the nucleon-nucleon cross section shows a minimum. Combined with a very good energy resolution of 25 keV it is possible to do two independent experiments. At first a separation of  $E1$  and  $M1$  contributions to the cross section can be done by comparing the experimentally extracted angular distributions. In addition a spinflip/non-spinflip separation of the cross section can be performed with the method of polarization transfer observables. As a reference case of a heavy nucleus these types of analyses have been performed for the nucleus  $^{208}\text{Pb}$  and they show good agreement [Pol11, Tam11, Pol12]. Also in a more recent study in the nucleus  $^{96}\text{Mo}$  [Mar13] the two methods have shown excellent agreement.

---

### 9.4 Outline

---

Within this work a high resolution polarized proton scattering experiment on the heavy deformed nucleus  $^{154}\text{Sm}$  has been performed at the RCNP in Osaka, Japan. The purpose was the investigation of the pygmy dipole resonance and the spin- $M1$  resonance at very forward angles including  $0^\circ$ . Part II of this thesis is structured in the following way. In section 10 the theoretical background for the polarized proton scattering experiment is introduced. The experimental proton scattering facility of the RCNP and the experimental setup is shown in section 11. The many steps of the data analysis procedure are explained in section 12, while the results are discussed in section 12.3. Part II closes also with a summary and an outlook for the future.



---

## 10 Theoretical background for polarized proton scattering at 0°

---

In this chapter the theoretical aspects concerning the scattering of (polarized) protons off a nucleus will be discussed. First of all the projectile-target interaction will be explained in details. Furthermore the distortion that the projectile wave functions experience by passing the charged distribution of the nucleus will be explained and since for the strong interaction up to now no complete picture has been established, information on effective nucleon-nucleon interactions will be given.

---

### 10.1 Inelastic proton scattering

---

During the scattering process, where the singly charged protons interact with the nucleus, the electromagnetic Coulomb force causes various kinds of electromagnetic transitions. At extreme forward angles the dominant transitions are electric and magnetic dipole excitations. Besides that the target and the projectiles also interact via the nuclear force that may trigger spinflip transitions.

If energy of the projectile is well below the Coulomb barrier

$$U_{Coulomb} = \frac{1}{4\pi\epsilon_0} \frac{Z_1 Z_2 e^2}{r} \quad (10.1)$$

only Coulomb interaction occurs. Here,  $\epsilon_0$  is the dielectric constant,  $Z_1$  and  $Z_2$  are the atomic numbers of the target and the projectile, respectively, and  $r$  denotes the interaction radius. If the projectile energy is higher than the Coulomb barrier, both types of interaction take place in a coherent way.

---

### 10.2 Lippmann-Schwinger equation

---

When solving the quantum mechanical problem of inelastic proton scattering at a nucleus, the first thing to start with is the time-independent Schrödinger equation (the formalism is mainly taken from the references [Pol11, Amo00, Sat83, Lip50]):

$$(H_0 + V)\psi = E\psi \quad (10.2)$$

where the Hamiltonian  $H_0$  can be separated into

$$H_0 = H_N + K_0. \quad (10.3)$$

$H_N$  is the nuclear Hamiltonian,  $K_0 = p^2/2m_p$  the kinetic energy of the proton and  $V$  the potential used as proton-nucleus interaction. Solving equation 10.2 leads to the well-known Lippmann-Schwinger equation [Lip50]:

$$\psi^\pm = \phi^\pm + \frac{1}{E - H_0 \pm i\epsilon} V \psi^\pm, \quad (10.4)$$

where the  $\pm$  stands for the incoming (+) and outgoing waves (-).  $\phi^\pm$  denote the ground state eigenfunction of the unperturbed state (in the limit  $V \rightarrow 0$ ) and  $\psi^\pm$  the eigenfunctions of the Lippmann-Schwinger equation. The transition operator for calculating the transition probability between perturbed and unperturbed states can be constructed:

$$T = V + V \frac{1}{E - H_0 \pm i\epsilon} T. \quad (10.5)$$

Now the differential cross section can be written as:

$$\frac{d\sigma}{d\omega}(\vec{k}_i, \vec{k}_f) = \left( \frac{\mu}{2\pi\hbar^2} \frac{|\vec{k}_f|}{|\vec{k}_i|} \right) T_{fi}(\vec{k}_i, \vec{k}_f). \quad (10.6)$$

Here, the incoming and outgoing proton wave functions in the laboratory frame are expressed by  $\vec{k}_i$  and  $\vec{k}_f$  and  $\mu$  denotes the reduced mass. It is important to mention, that equation 10.6 only holds for even-even nuclei which have a  $J^\pi = 0^+$  ground state.

---

### 10.3 Distorted waves

---

In the Distorted Wave Born Approximation (DWBA), the Lippmann-Schwinger equation (10.4) can be rewritten by expanding the transition matrix  $T_{fi}(\vec{k}_i, \vec{k}_f)$  in a basis of distorted wave functions  $\chi^\pm$ :

$$\chi^\pm = \phi^\pm + \frac{1}{E - H_0 \pm i\epsilon} V_0 \chi^\pm, \quad (10.7)$$

with  $V_0 = V_0(\vec{r} - \vec{r}_N)$  describing the interaction between the projectile and the target in the incoming channel. The computer code DWBA07 [Ray07] which has been used in this work to calculate the DWBA transition amplitudes, uses the descriptions given above.

---

## 10.4 Optical potential

---

From the potential given in equation 10.7 a so-called local potential, or often referred to as optical potential,  $U_0(\vec{r})$  can be constructed by a convolution of  $V_0$  with the ground state density  $\rho_0(\vec{r}_N)$  of the nucleus

$$U_0(\vec{r}) = \int \rho_0(\vec{r}_N) V_0(\vec{r} - \vec{r}_N) d^3 r_N. \quad (10.8)$$

In an alternative approach one uses elastic scattering data to construct phenomenological optical potentials. Optical model potentials are usually made up of a central and a spin-orbit term with both real and imaginary part. A commonly used parametrization in the non-relativistic case is

$$U(\vec{r}) = V_{\text{Coulomb}}(r) + V_0 f(x_0) + iW_0 f(x_0) - 2(V_{\text{so}} + iW_{\text{so}}) \frac{1}{r} \frac{d}{dr} f(x_{\text{so}}) \vec{L} \cdot \vec{\sigma}, \quad (10.9)$$

with

$$f(x_i) = \frac{1}{1 + e^{x_i}} \quad \text{and} \quad x_i = \frac{(r - r_i A^{1/3})}{a_i}, \quad (i = 0, \text{so}). \quad (10.10)$$

Here  $V_{\text{Coulomb}}(r)$  is the Coulomb potential and  $V_j$  ( $W_j$ ) the real (imaginary) depths for the central and the spin-orbit term, respectively. The Woods-Saxon functions  $f(x_j)$  with radius  $x_j$  and surface diffuseness  $a_j$  are used to build the radial dependence.

---

## 10.5 Effective nucleon-nucleus interaction

---

Nucleon-nucleus scattering has been a widely used tool to investigate nuclear structure in the intermediate energy region between 100 MeV and 800 MeV [Tam99, Tam07, Tam09, Tam11]. In this energy region the contribution of multistep excitation to the complete cross section is suppressed as well as distortion effects. The distorted wave impulse approximation (DWIA) provides a good description of the inelastic scattering process. The distortion of incoming and outgoing waves is described with the use of optical potentials.

For protons with  $S = \frac{1}{2}$  and  $T = \frac{1}{2}$  four possible excitation modes are possible

- isoscalar non-spinflip ( $\Delta T = 0, \Delta S = 0$ ),
- isoscalar spinflip ( $\Delta T = 0, \Delta S = 1$ ),

- isovector non-spinflip ( $\Delta T = 1, \Delta S = 0$ ),
- isovector spinflip ( $\Delta T = 1, \Delta S = 1$ ).

Nucleon-nucleon interactions can be constructed in many different ways. The famous Bonn and Paris interactions [Are00] use consistent meson-exchange contributions, whereas Epelbaum *et al.* [Epe13] use the chiral effective field theory by expanding the nucleon-nucleon potential by means of many-body forces. In the early 1980s, Love and Franey [Lov81, Fra85] developed a projectile-nucleus interaction for the above mentioned intermediate beam energies:

$$V(\vec{r}, \vec{p}) = V^C(r) + V^{LS}(r) \vec{L} \cdot \vec{S} + V^T(r) S_{12}. \quad (10.11)$$

Here,  $V^C$  denotes the central part,  $V^{LS}$ , the spin-orbit component and  $V^T$  the tensor part. Table 10.1 shows the different components that are used in equation 10.11. Since the momentum

**Table 10.1.:** Variables used in Equation (10.11).

$\vec{r}$	relative distance vector	$\vec{r} = \vec{r}_1 - \vec{r}_2$
$\vec{L}$	relative angular momentum	
$\vec{S}$	relative spin	$\vec{S} = \vec{\sigma}_1 + \vec{\sigma}_2$
$\vec{L} \cdot \vec{S}$	spin-orbit operator	
$S_{12}$	tensor operator	$S_{12} = 3(\vec{\sigma}_1 \cdot \hat{r})(\vec{\sigma}_2 \cdot \hat{r}) - \vec{\sigma}_1 \cdot \vec{\sigma}_2, \quad \hat{r} = \vec{r}/ \vec{r} $
$\vec{\sigma}_i$	Pauli spin operator	

transfer in the proton scattering process investigated in this work is smaller than  $1 \text{ fm}^{-1}$  the fraction of the spin-orbit contribution and the tensor contribution are negligible in comparison to the central part. Consequently, the effective interaction consists only of terms with different spin-isospin transfer properties:

$$V(\vec{r}, \vec{p}) = V_0^C(r) + V_\sigma^C(r) \vec{\sigma}_1 \cdot \vec{\sigma}_2 + V_\tau^C(r) \vec{\tau}_1 \cdot \vec{\tau}_2 + V_{\sigma\tau}^C(r) \vec{\sigma}_1 \cdot \vec{\sigma}_2 \vec{\tau}_1 \cdot \vec{\tau}_2. \quad (10.12)$$

Here, the spin operator  $\vec{\sigma}_1 \cdot \vec{\sigma}_2$  causes spinflip transitions, and the isospin operator  $\vec{\tau}_1 \cdot \vec{\tau}_2$  is responsible for isospin flips. The spin-isospin operator  $\vec{\sigma}_1 \cdot \vec{\sigma}_2 \vec{\tau}_1 \cdot \vec{\tau}_2$  has the effect that spin and isospin flip simultaneously. Figure 10.1 shows the central parts of equation 10.12 as a function of the energy of the projectile. One can clearly see, that  $V_0^C$  dominates for all projectile energies and that the contribution of the spin part  $V_\sigma^C$  is the smallest. However,  $V_\sigma^C$  shows a maximum at projectile energies of roughly 200 MeV, while the spin- and isospin-independent term  $V_0^C$  and the isospin-dependent term  $V_\tau^C$  have their minima in the energy range between 200 - 300 MeV. That means the ratios  $V_{\sigma\tau}/V_0^C$  and  $V_{\sigma\tau}^C/V_\tau^C$  are enhanced which provides excellent conditions to observe isovector spinflip excitations, e.g. spinflip-M1 excitations.



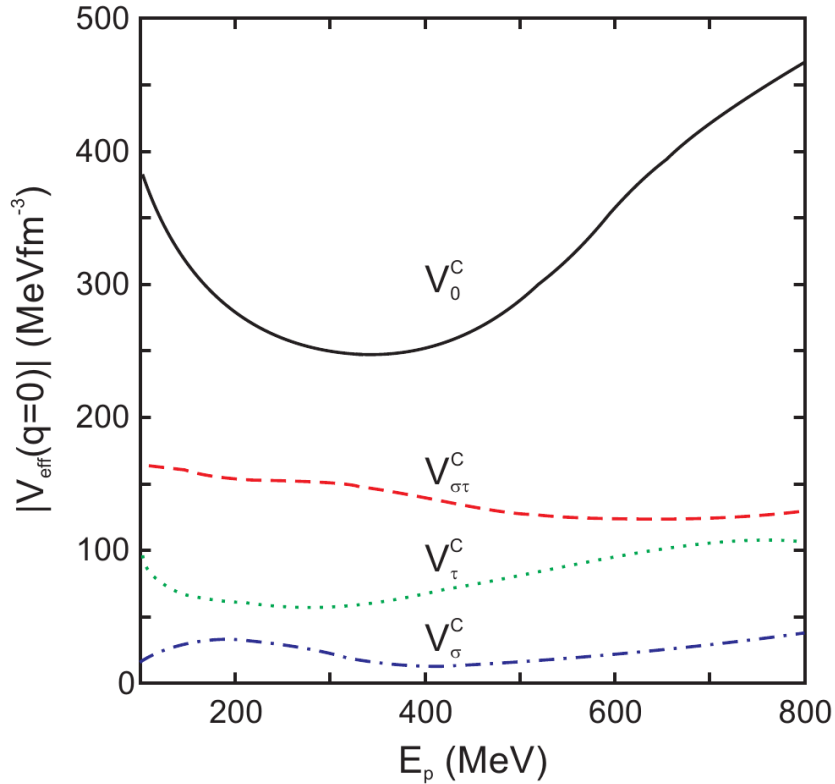


**Figure 10.1.:** Energy dependence of the central parts of the nucleon-nucleon scattering in the  $q \approx 0$  limit [Lov81].

---

## 10.6 Coulomb excitation

---

### 10.6.1 Classical Coulomb excitations

---

For large impact parameters  $b > r_{\text{Coulomb}}$ , where  $r_{\text{Coulomb}} = r_p + r_t$  is the sum of the projectile and target radii, mainly Coulomb excitation is observed, since the nuclear excitation cross sections are marginal. In this case the Coulomb repulsion prevents projectile and target from approaching each other too closely. Consequently the excitation cross sections are directly proportional to the transition matrix elements revealing basic nuclear structure information. Furthermore, Coulomb excitation is well understood [Ber85], so that it is possible to extract the corresponding electromagnetic transition strengths  $B(\pi\lambda)$  independently of nuclear models. There are two common descriptions of this process: the excitation of a target nucleus in the electromagnetic field of a charged projectile, or vice versa, and the exchange of virtual photons between the interacting particles.

## 10.6.2 Semiclassical coulomb excitations

In the semiclassical Coulomb scattering approach a point-like charged projectile with the mass  $m$  and momentum  $\vec{p}$  comes from infinity and moves along the target nucleus. A schematical view can be seen in figure 10.2. Here, the impact parameter  $b$  gives the closest distance between projectile and the target. The momentum transfer  $q = |\vec{k} - \vec{k}'|$  can be expressed as a function of

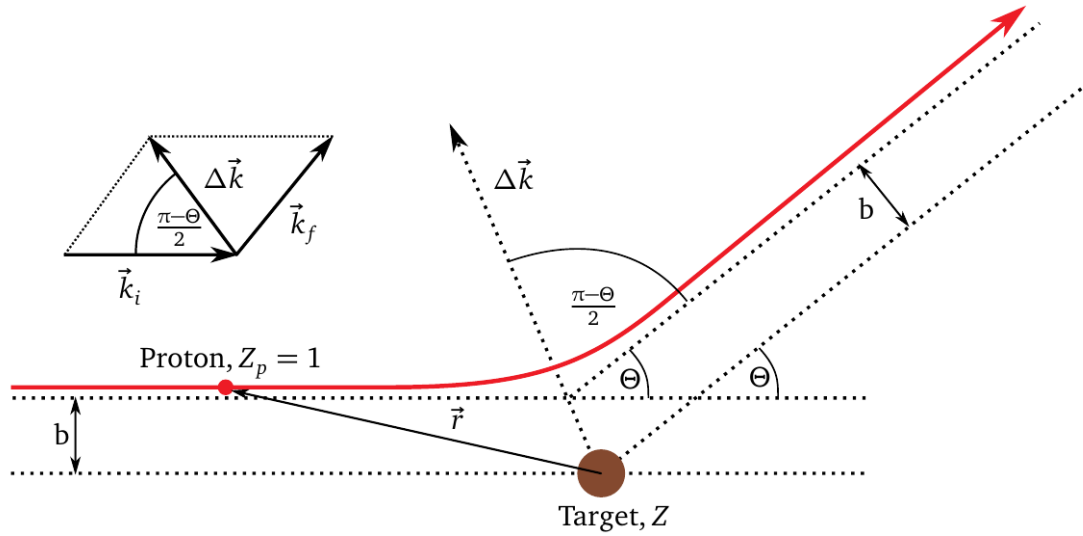


**Figure 10.2.:** Classical picture of a projectile trajectory in the coulomb scattering process. The impact parameter is denoted with  $b$ . The projectile is moving along the red curvature. The picture is taken from reference [Mat14].

the mass  $m$ , the particle velocity  $v_0$  and the scattering angle  $\theta$ :

$$q = 2mv_0 \sin\left(\frac{\theta}{2}\right). \quad (10.13)$$

The famous Rutherford scattering formula gives the differential elastic cross section:

$$\left(\frac{d\sigma}{d\Omega}\right)_{\text{Ruth}} = a^2 \frac{1}{\sin^4\left(\frac{\theta}{2}\right)} \quad (10.14)$$

with

$$a = \frac{1}{4\pi\epsilon_0} \frac{Z_1 Z_2 e^2}{4E}. \quad (10.15)$$

In case of small momentum transfer, when the bombarding energy of the projectile is large compared to its energy loss, large cross sections due to inelastic Coulomb scattering are observed.

Introducing relativistic projectile energies ( $\beta = v/c$ ), the Rutherford scattering formula (10.14) transforms to the Mott formula

$$\left(\frac{d\sigma}{d\Omega}\right)_{\text{Mott}} = \left(\frac{d\sigma}{d\Omega}\right)_{\text{Ruth}} \left[1 - \beta^2 \sin^2\left(\frac{\theta}{2}\right)\right]. \quad (10.16)$$

In a good approximation, the relative motion follows a classical Rutherford trajectory [Win79]. The differential cross section is then be given by

$$\left(\frac{d\sigma}{d\Omega}\right) = \left(\frac{d\sigma}{d\Omega}\right)_{\text{Ruth}} P_{i \rightarrow f}. \quad (10.17)$$

The probability for the excitation of an initial state  $|i\rangle$  into a final state  $|f\rangle$  is given by  $P_{i \rightarrow f}$ . For a time-dependent electromagnetic field  $V(\vec{r}(t))$ , that weakly excites the target,  $P_{i \rightarrow f} = |a_{i \rightarrow f}|^2$  can be calculated in first order perturbation theory by means of the excitation amplitude

$$a_{i \rightarrow f} = \frac{1}{i\hbar} \int_{-\infty}^{\infty} e^{i\omega t} \langle f | V(\vec{r}(t)) | i \rangle dt, \quad (10.18)$$

with  $\omega = (E_i - E_f)/\hbar$ . With a multipole expansion of  $V(\vec{r}(t))$ , the excitation amplitude can be given as

$$a_{i \rightarrow f} = i \sum_{\lambda} \chi_{i \rightarrow f}^{\pi\lambda} f_{\lambda}(\xi), \quad (10.19)$$

with the strength parameter  $\chi_{i \rightarrow f}^{\pi\lambda}$ , which describes the action of the field in terms of matrix elements of electric and magnetic multipole moments with parity  $\pi$  and multipolarity  $\lambda$ . The factors  $f_{\lambda}(\xi)$  define the dependence of the cross section on the degree of adiabaticity, which is given by the adiabaticity parameter  $\xi = \omega b / (v\gamma)$ . The total cross section for Coulomb excitation of a final state  $|f\rangle$  for a component with given  $\pi\lambda$  yields

$$\sigma_{\pi\lambda} = 2\pi \int_R^{\infty} b P_{i \rightarrow f}(b) db \approx 2\pi \int_R^{\rho_a} b \left| \chi_{i \rightarrow f}^{\pi\lambda}(b) \right|^2 db. \quad (10.20)$$

In equation (10.20),  $R$  is taken as the sum of the nuclear radii of projectile and target, below which nuclear interaction will also occur, while  $\rho_a = v\gamma/\omega$  is the impact parameter evaluated

at  $\xi = 1$ , where the adiabatic cutoff sets in. Inserting  $\chi_{i \rightarrow f}^{\pi\lambda}$  and considering a  $0^+$  ground state  $|i\rangle$  (as in the case of  $^{154}\text{Sm}$ ), this leads to

$$\sigma_{\pi\lambda} \approx \left( \frac{Z_1 e^2}{\hbar c} \right)^2 \frac{B(\pi\lambda; 0 \rightarrow \lambda)}{e^2 R^{2\lambda}} \pi R^2 \begin{cases} (\lambda - 1)^{-1} & \text{for } \lambda \geq 2, \\ 2 \ln(\rho_a/R) & \text{for } \lambda = 1. \end{cases} \quad (10.21)$$

Therefore, the reduced transition strength  $B(\pi\lambda, 0 \rightarrow \lambda)$  can be obtained by measuring the scattering cross sections. In case of  $E1$  transitions that are investigated in this work, equation (10.21) simplifies to

$$\sigma_{E1} \approx \left( \frac{Z_1 e^2}{\hbar c} \right)^2 \frac{2\pi \ln(\rho_a/R)}{e^2} B(E1; 0 \rightarrow 1). \quad (10.22)$$

---

### 10.6.3 Equivalent virtual photon method

---

Coulomb excitation can be considered as the absorption of virtual photons by the target nucleus. Produced by the moving projectile, the number of virtual photons is related to the amount of real photons, which would have an equivalent net effect for one specific transition. It is linked to the Fourier transformation of the time-dependent electromagnetic field induced by the projectile. A theoretical description of this process is given in [Ber88]. Here, the Coulomb excitation cross section is expressed as

$$\sigma_{i \rightarrow f} = \sum_{\pi\lambda} \int N_{\pi\lambda}(E_\gamma) \sigma_\gamma^{\pi\lambda}(E_\gamma) \frac{1}{E_\gamma} dE_\gamma, \quad (10.23)$$

where  $\sigma_\gamma^{\pi\lambda}(E_\gamma)$  is the photoabsorption cross section depending on the photon energy  $E_\gamma$  and  $N_{\pi\lambda}(E_\gamma)$  is the equivalent photon numbers for electric ( $\pi = E$ ) or magnetic ( $\pi = M$ ) transitions of multipole order  $\lambda$ . In a semiclassical approximation [Ber88, Win79] the virtual photon numbers can be calculated analytically for negligible energy loss of the projectile. As long as the object is large enough compared to the wavelength of light, this assumption works quite well. However, microscopic phenomena have to be explained by Maxwell's equations with the dispersion relation  $\omega = kc$ . In quantum mechanics, microscopic phenomena are described by Schrödinger's equation with a dispersion relation  $\omega = \hbar k^2/2m$  for small scales, too. Just as well

an eikonal approximation can be adopted here for processes concerning small scattering angles and large impact parameters. This leads to

$$N_{\pi\lambda}(E_\gamma) = Z_1^2 \alpha \frac{\lambda[(2\lambda + 1)!!]^2}{(2\pi)^3(\lambda + 1)} \sum_m \left| G_{\pi\lambda m} \left( \frac{c}{v_0} \right) \right|^2 g_m(\xi), \quad (10.24)$$

with the fine structure constant  $\alpha = e^2/\hbar c$  and the functions  $g_m$  and  $G_{\pi\lambda m}$ , which are tabulated in [Win79]. In a similar way, the double differential cross section is derived from virtual photon numbers as

$$\frac{d^2\sigma}{d\Omega dE_\gamma} = \frac{1}{E_\gamma} \sum_{\pi\lambda} \frac{dN_{\pi\lambda}}{d\Omega} \sigma_\gamma^{\pi\lambda}(E_\gamma). \quad (10.25)$$

$$\left( \frac{dN_{E1}}{d\Omega} \right)_{rel} = \frac{Z_1^2 \alpha}{4\pi^2} \zeta^2 \varepsilon^2 \left( \frac{1}{\gamma\beta} \right)^2 \left[ K_1^2(x) + \frac{1}{\gamma^2} K_0^2(x) \right]. \quad (10.26)$$

Here,  $\zeta = \omega a/v_0$  is the adiabaticity parameter with  $a = Z_1 Z_2 e^2/\mu v_0^2$  referring to half of the closest distance,  $\mu$  is the reduced mass, and  $\varepsilon = \sin^{-1}(\theta/2)$  the eccentricity parameter. The variable in  $K(x)$  of the modified Bessel function of the second kind is an abbreviation for  $x = (\varepsilon\zeta/\gamma)\cos(\theta/2)$ . For  $\gamma \approx 1$  ( $\varepsilon \gg 1$ ) the equivalent photon number for  $E1$  transitions can be calculated as

$$\left( \frac{dN_{E1}}{d\Omega} \right)_{nonrel} = \frac{Z_1^2 \alpha}{4\pi^2} \varepsilon^2 \left( \frac{1}{\beta} \right)^2 x^2 \left[ K_1^2(x) + K_0^2(x) \right]. \quad (10.27)$$

---

## 10.6.4 Eikonal description of Coulomb excitation

---

Since the semiclassical treatment of the virtual photon number does not work properly at very low scattering angles and produces a pole at  $0^\circ$ , Bertulani and Nathan [Ber93] found a way to include diffraction and get rid of the semiclassical approximations for the impact parameter. For the virtual photon numbers they obtain

$$\frac{dN_{\pi\lambda}}{d\Omega} = Z_1^2 \alpha \left( \frac{\omega k}{\gamma v} \right)^2 \frac{\lambda[(2\lambda + 1)!!]^2}{(2\pi)^3(\lambda + 1)} \sum_m \left| G_{\pi\lambda m} \left( \frac{c}{v_0} \right) \right|^2 |\Omega_m(q)|^2 \quad (10.28)$$

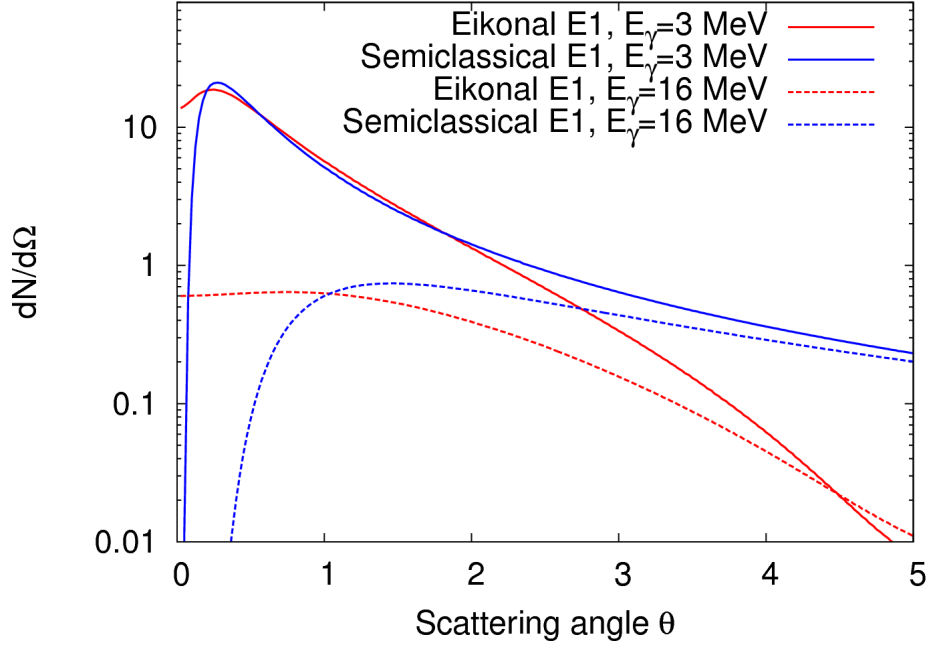


**Figure 10.3.:** Virtual photon numbers per unit solid angle for E1 transitions in Coulomb excitation induced by 295 MeV protons on a  $^{154}\text{Sm}$  target at  $E_\gamma=3$  MeV and 16 MeV. In blue: semiclassical calculation [Win79], in red: eikonal approximation [Ber93].

where the function  $\Omega_m(q)$  is given by

$$\Omega_m(q) = \int_0^\infty db b J_m(qb) K_m\left(\frac{\omega b}{\gamma v}\right) e^{i\chi(b)}. \quad (10.29)$$

Here,  $q = 2k \sin(\frac{1}{2}\theta)$  is the momentum transfer,  $\theta$  the scattering angle and

$$\chi(b) = -\frac{1}{\hbar v} \int_0^\infty U_N^{opt}(z', b) dz' + \psi_C(b) \quad (10.30)$$

the nuclear optical potential which can be obtained from fits to the available elastic-scattering data. Figure 10.3 shows a comparison between the semiclassical approximation of the virtual photon number (blue lines) and the approximation by the eikonal description including quantum mechanical diffraction effects (red lines). The spectra are calculated for E1 transitions in Coulomb excitation in the  $^{154}\text{Sm}(p,p')$  reaction at incident proton beam energies of 295 MeV for the excitation energies 3 MeV (solid lines) and 16 MeV (dashed lines), respectively. One concludes from figure 10.3 that the two methods yield drastically different results with increasing energy  $E_\gamma$ .

## 10.7 Magnetic dipole transitions and $B(M1_{\sigma\tau})$ from $(p,p')$ cross section data

For magnetic dipole transitions that are induced by the electromagnetic interaction the total spin of the nucleus changes by one ( $\Delta J = 1$ ) while the parity  $\pi$  of the total nuclear wave function does not change ( $\pi_i\pi_f = 1$ ). This is possible for  $\Delta L = 1$  transitions or for  $\Delta S = 1$  transitions. Since we are considering spinflip transitions in  $^{154}\text{Sm}$ , the  $B(M1)$  transition strength (see [Fuj11]) is defined as

$$B(M1) = \frac{3}{4\pi} \frac{1}{2J+1} \left| \langle \psi'_N || O(M1) || \psi_N \rangle \right|^2. \quad (10.31)$$

Here,  $|\psi_N\rangle$  and  $|\psi'_N\rangle$  are the nuclear wave functions before and after the transition and  $J$  is the total angular momentum of the initial state.  $O(M1)$  is the operator of the magnetic dipole moment, which can be separated into an isoscalar part ( $IS, \Delta T = 0$ ) and an isovector part ( $IV, \Delta T = 1$ ):

$$O(M1) = \left[ \sum_{i=1}^Z \left( g_l^p \vec{l}_i + \frac{1}{2} g_s^p \vec{\sigma}_i \right) + \sum_{i=Z+1}^A \left( g_l^N \vec{l}_i + \frac{1}{2} g_s^N \vec{\sigma}_i \right) \right] \mu_N \quad (10.32)$$

$$= \left[ \sum_{i=1}^A \left( g_l^{IS} \vec{l}_i + \frac{1}{2} g_s^{IS} \vec{\sigma}_i + \tau_{zi} \left( g_l^{IV} \vec{l}_i + \frac{1}{2} g_s^{IV} \vec{\sigma}_i \right) \right) \right] \mu_N \quad (10.33)$$

with  $\vec{\sigma}_i$  being the Pauli spin operator and  $\tau_{zi} = 1$  (0) for protons and neutrons, respectively. Utilizing the Wigner-Eckhardt theorem, the  $B(M1)$  transition strength can now be rewritten:

$$B(M1) = \frac{3}{4\pi} \frac{1}{2J+1} \left| \frac{C_{M1,00}}{\sqrt{2T'+1}} \left( g_l^{IS} M(\vec{l}) + \frac{1}{2} g_s^{IS} M(\vec{\sigma}) \right) + \frac{C_{M1,10}}{\sqrt{2T'+1}} \left( g_l^{IV} M(\tau\vec{l}) + \frac{1}{2} g_s^{IV} M(\tau\vec{\sigma}) \right) \right|^2 \mu_N^2 \quad (10.34)$$

Here,  $C_{M1,00}$  and  $C_{M1,10}$  denote the Clebsch-Gordan coefficients ( $TT_z 00 | T'T'_z$ ) and ( $TT_z 10 | T'T'_z$ ), respectively, and  $\tau$  represents the isospin operator.  $T$  and  $T'$  stand for the total nuclear isospin

in the initial and final state. With the help of equation 10.34 the  $B(M1)$  transition strength can now be separated in an isovector and an isoscalar part:

$$B(M1)_{IS} = \frac{3}{4\pi} \frac{1}{2J+1} \frac{C_{M1,00}^2}{2T'+1} \left| g_l^{IS} M(\vec{l}) + \frac{1}{2} g_s^{IS} M(\vec{\sigma}) \right|^2 \mu_N^2 \quad (10.35)$$

$$B(M1)_{IV} = \frac{3}{4\pi} \frac{1}{2J+1} \frac{C_{M1,10}^2}{2T'+1} \left| g_l^{IV} M(\tau\vec{l}) + \frac{1}{2} g_s^{IV} M(\tau\vec{\sigma}) \right|^2 \mu_N^2. \quad (10.36)$$

In the case of pure spinflip transitions, these transition strengths reduce to:

$$B(M1)_{IS} \approx \frac{3}{16\pi} \frac{1}{2J+1} \frac{C_{M1,00}^2}{2T'+1} \left| g_s^{IS} M(\vec{\sigma}) \right|^2 \mu_N^2 \quad (10.37)$$

$$B(M1)_{IV} \approx \frac{3}{16\pi} \frac{1}{2J+1} \frac{C_{M1,10}^2}{2T'+1} \left| g_s^{IV} M(\tau\vec{\sigma}) \right|^2 \mu_N^2. \quad (10.38)$$

If the nucleus is excited via inelastic proton scattering, the interaction is mainly mediated via the nuclear force and not via the electromagnetic interaction. Additionally, it has been shown that at very low momentum transfers (e.g.  $q \rightarrow 0$ ) and proton energies around 300 MeV, mostly isovector spinflip transitions occur. Thus, an excitation of  $^{154}\text{Sm}$  from the ground state to a  $1^+$  state corresponds to a spinflip- $M1$  excitation with a reduced transition strength of

$$B(M1)_{\sigma\tau} = \frac{1}{2(2J+1)} \frac{C_{M1,10}^2}{2T'+1} |M(\tau\vec{\sigma})|^2. \quad (10.39)$$

Also referring to [Fuj11] the following relation can be defined

$$B(M1)_{\sigma\tau} = \frac{\left( \frac{d\sigma}{d\Omega} \right)_{pp'}^{M1}(0^\circ)}{F_{M1} \hat{\sigma}_{M1}(A)}. \quad (10.40)$$

Here,  $\left( \frac{d\sigma}{d\Omega} \right)_{pp'}^{M1}(0^\circ)$  denotes the spinflip- $M1$  cross section, measured in inelastic proton scattering at  $0^\circ$ . The kinematical correction factor  $F_{M1}$  can be calculated from the ratio of the theoretical cross section at excitation energy of  $E_x = 0$  MeV to the theoretical cross section at an excitation energy of  $E_x$ .  $\hat{\sigma}_{M1}(A)$  is the so-called 'unit cross section' that represents the mass dependence of  $B(M1)_{\sigma\tau}$ . Analogue to equation 10.40 the reduced transition strength for Gamow-Teller transitions can be defined as

$$B(GT) = \frac{1}{2} \frac{1}{(2J+1)} \frac{C_{GT,\pm}^2}{2T'+1} |M(\tau\vec{\sigma})|^2, \quad (10.41)$$



and the corresponding definition, involving the unit cross section for Gamow-Teller transitions  $\hat{\sigma}_{GT^\pm}(A)$ :

$$B(GT^\pm) = \frac{\left(\frac{d\sigma}{d\Omega}\right)_{pp'}^{GT^\pm}(0^\circ)}{F_{GT^\pm} \hat{\sigma}_{GT^\pm}(A)}. \quad (10.42)$$

---

## 10.8 Polarization transfer observables (PT observables)

---

Polarized proton scattering is a well established tool for the distinction from spinflip and non-spinflip transitions in nuclei [Ohl02, Wol56]. In a simple notation, these reactions are of the type:

$$\frac{\vec{1}}{2} + A \rightarrow \frac{\vec{1}}{2} + A' \quad (10.43)$$

with  $\frac{\vec{1}}{2}$  denoting a polarized spin- $\frac{1}{2}$  proton,  $A$  the target nucleus and  $A'$  the excited target nucleus.

Using the plane wave impulse approximation (PWIA), the  $T$ -matrix for nucleon-nucleus scattering between an initial state  $|i\rangle$  and a final state  $|f\rangle$  can be written as

$$T = \langle f | M(q) e^{-i\vec{q}\cdot\vec{r}} | i \rangle. \quad (10.44)$$

The analyzing power for the  $j$ -th component of the beam polarization vector, the differential cross section  $d\sigma/d\Omega$  and the polarization transfer observables  $D_{ij}$  can then be expressed in terms of the  $T$ -matrix [Kaw02]

$$A_j = \frac{\text{Tr}(TT^\dagger \sigma_n)}{\text{Tr}(TT^\dagger)}, \quad \frac{d\sigma}{d\Omega} = \frac{1}{2} \text{Tr}(TT^\dagger), \quad D_{ij} = \frac{\text{Tr}(T\sigma_j T^\dagger \sigma_i)}{\text{Tr}(TT^\dagger)}, \quad (10.45)$$

where  $i$  and  $j$  denote the direction of the projectile spin in the initial and final state, respectively. According to [Ker59] one can write the nucleon-nucleon scattering amplitude  $M_{NN}$  as a phenomenological sum of operators in spin space

$$M_{NN} = A + B\sigma_{1\hat{n}}\sigma_{2\hat{n}} + C(\sigma_{1\hat{n}} + \sigma_{2\hat{n}}) + E\sigma_{1\hat{q}}\sigma_{2\hat{q}} + F\sigma_{1\hat{p}}\sigma_{2\hat{p}}. \quad (10.46)$$

Here, the indices  $\hat{n}$ ,  $\hat{p}$  and  $\hat{q}$  are unit vectors of the coordinate system that origins in the rest-frame of the polarized proton that is flying on the ideal trajectory. This coordinate system is defined as

$$\hat{n} = \frac{\vec{n}}{|\vec{n}|}, \quad \vec{n} = \vec{k}' \times \vec{k}, \quad (10.47)$$

$$\hat{q} = \frac{\vec{q}}{|\vec{q}|}, \quad \vec{q} = \vec{k}' - \vec{k}, \quad (10.48)$$

$$\hat{p} = \hat{q} \times \hat{n}, \quad (10.49)$$

where  $\vec{k}$  and  $\vec{k}'$  are the incoming and scattered momentum vectors, respectively. With the assumption that each of the components  $A - F$  of the nucleon-nucleon scattering amplitude  $M_{NN}$  can be represented as a sum of isoscalar and isovector terms (e.g.)

$$A = A_{IS} + A_{IV} \vec{\tau}_1 \cdot \vec{\tau}_2, \quad (10.50)$$

equation (10.46) transforms to

$$M_{NN} = A + \frac{1}{3}(B + E + F) \vec{\sigma}_1 \cdot \vec{\sigma}_2 + C (\vec{\sigma}_1 + \vec{\sigma}_2) + \frac{1}{3}(E - B) S_{12}(\hat{q}) + \frac{1}{3}(F - B) S_{12}(\hat{p}), \quad (10.51)$$

where the tensor operator  $S_{12}(\hat{q})$  is defined as

$$S_{12}(\hat{q}) = \frac{3(\vec{\sigma}_1 \cdot \vec{r})(\vec{\sigma}_2 \cdot \vec{r})}{r^2} - \vec{\sigma}_1 \cdot \vec{\sigma}_2 \quad (10.52)$$

and the other terms correspond to the central spin-independent, central spin-dependent, spin-orbit, direct tensor and the tensor exchange components of the effective interaction, respectively. At  $0^\circ$  scattering experiments, the spin-orbit ( $C$ ) and the direct tensor ( $E - B$ ) parts cancel, since  $C = 0$  and  $E = B$  [Mos82]. Thus, the polarization transfer observables can be defined as:

$$D_{SL} = D_{LS} = 0, \quad (10.53)$$

$$D_{SS} = D_{NN} = \frac{(|B_i|^2 - |F_i|^2) X_T^2 - |B_i|^2 X_L^2}{(|B_i|^2 + |F_i|^2) X_T^2 + |B_i|^2 X_L^2}, \quad (10.54)$$

$$D_{LL} = \frac{(-3|B_i|^2 + |F_i|^2) X_T^2 + |B_i|^2 X_L^2}{(|B_i|^2 + |F_i|^2) X_T^2 + |B_i|^2 X_L^2}. \quad (10.55)$$

The indices  $L$  (longitudinal),  $N$  (normal) and  $S$  (sideways) refer to the axes  $\hat{l}$ ,  $\hat{n}$  and  $\hat{s}$  in the projectile helicity frame, that can be seen in figure 10.4. Here,  $\hat{l}$  goes along the beam direction,  $\hat{n}$  denotes the normal to the horizontal plane and  $\hat{s}$  completes the right-handed coordinate system. Additionally, the quantities  $X_L$  and  $X_T$  are the spin-longitudinal and spin-transverse form factors.

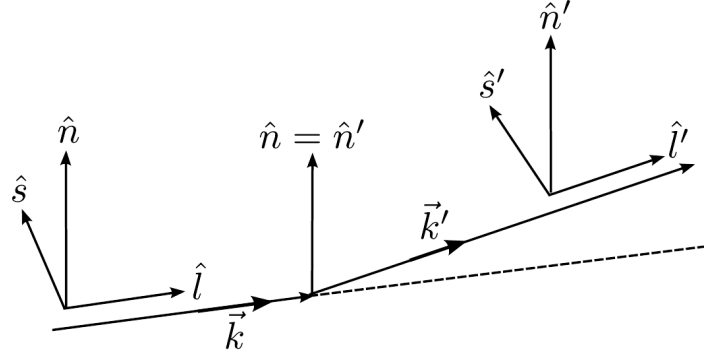


**Figure 10.4.:** Coordinate system in the projectile frame.

The polarization transfer observables  $D_{NN}$  and  $D_{SS}$  are equal, due to rotational symmetry at  $0^\circ$ . At very forward angles, the sum of the diagonal elements is equal to -1 for spinflip transitions and equal to 3 in the case of non-spinflip transitions [Suz00]. Therefore, the total spin transfer  $\Sigma$  can be defined as a linear combination of polarization transfer coefficients [Sak97]

$$\Sigma = \frac{3 - (D_{SS} + D_{NN} + D_{LL})}{4}. \quad (10.56)$$

At  $0^\circ$ , where  $D_{NN} = D_{SS}$  holds,  $\sigma$  can be simplified to

$$\Sigma = \frac{3 - (2D_{NN} + D_{LL})}{4} = \frac{3 - (2D_{SS} + D_{LL})}{4}. \quad (10.57)$$

In  $(\vec{p}, \vec{p}')$  experiments at forward angles ( $\hat{l} \approx \hat{l}'$ ),  $\Sigma$  becomes 1 for spinflip or 0 for non-spinflip transitions and it is now possible to extract spinflip and non-spinflip cross section parts from polarization transfer measurements

$$\frac{d\sigma}{d\Omega}(\Delta S = 1) \equiv \Sigma \left( \frac{d\sigma}{d\Omega} \right), \quad (10.58)$$

$$\frac{d\sigma}{d\Omega}(\Delta S = 0) \equiv (1 - \Sigma) \left( \frac{d\sigma}{d\Omega} \right). \quad (10.59)$$

---

Since in proton scattering experiments at very forward angles, dipole excitations are favored, non-spinflip cross sections can be associated with  $E1$  excitations whereas spinflip cross sections are assigned to spinflip-M1 excitations. This method has already been successfully applied in the analysis of nuclei in various mass regions:  $^{12}\text{C}$  [Tam99],  $^{16}\text{O}$  [Kaw02],  $^{96}\text{Mo}$  [Mar13],  $^{120}\text{Sn}$  [Kru] and  $^{208}\text{Pb}$  [Pol11].

## 11 Polarized proton scattering experiment at RCNP

At the Research Center for Nuclear Physics (RCNP) [RCN14] in Osaka, Japan, a high resolution study with polarized protons on the heavy deformed nucleus  $^{154}\text{Sm}$  at very forward angles including  $0^\circ$  was performed. A schematic overview of the experimental facilities at the RCNP is depicted in figure 11.1.

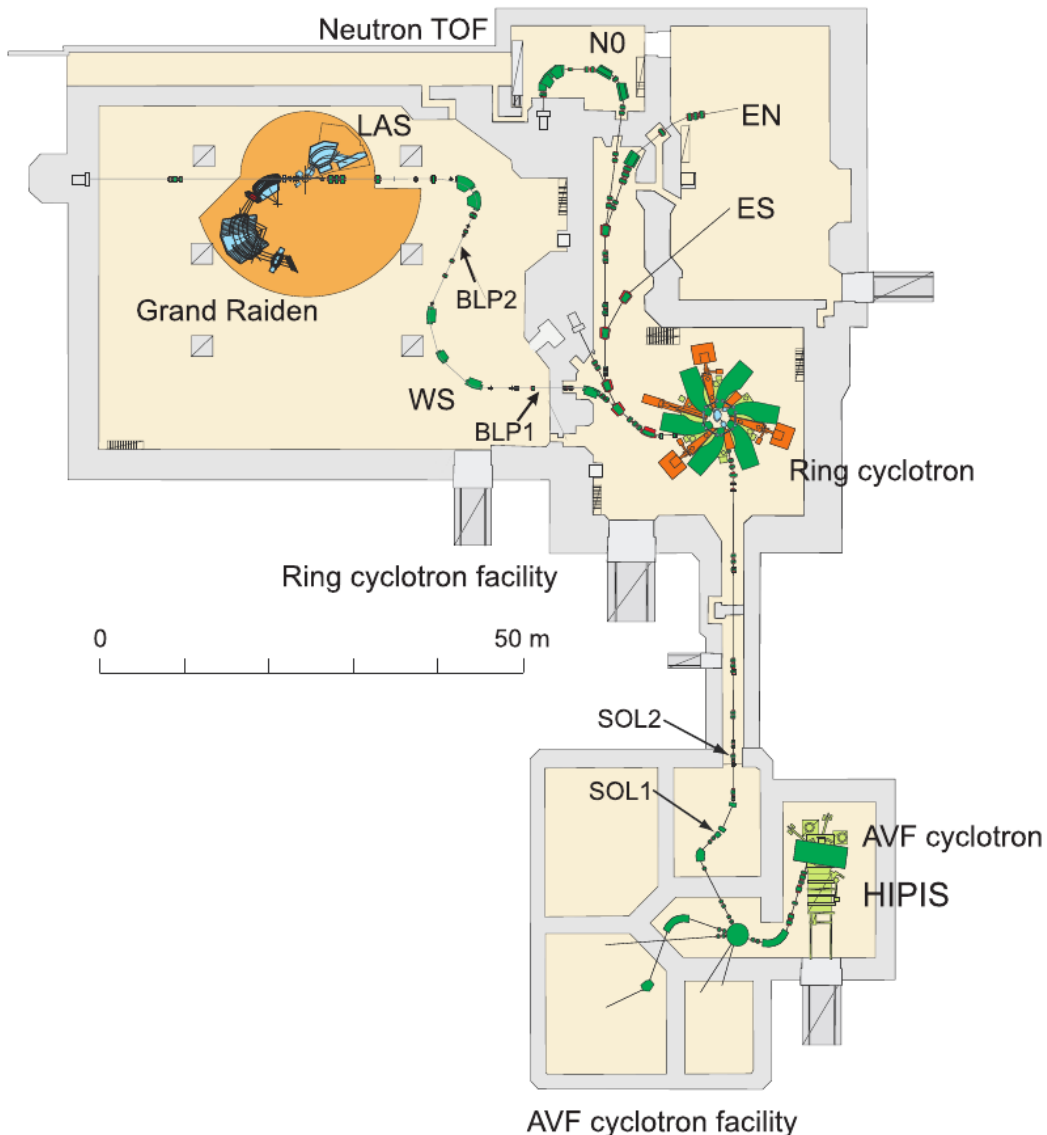


**Figure 11.1.:** Schematic overview of the RCNP facility in Osaka.

Polarized protons with a typical polarization of 70% are produced in the High Intensity Polarized Ion Source (HIPIS) [Hat97]. Here, hydrogen molecules were dissociated and a beam of cooled hydrogen atoms was produced. By using the Stern-Gerlach Effect, one polarization (either up or down) is selected and this part of the beam gets ionized in an electron cyclotron

---

ionizer (ECR). In order to compensate geometrical asymmetries of the experimental setup, the beam polarization is flipped with a frequency of 1 Hz. For the measurements at finite spectrometer angles, the NEOMAFIOS ECR [Tan91] source has been used due to its ability to provide much higher proton intensities.

The (polarized) proton beam was then injected in the Azimuthally Varying Field (AVF) Cyclotron and accelerated to a kinetic energy of 54 MeV. After the AVF Cyclotron, the beam was transported to the RING Cyclotron and accelerated to the final energy of 295 MeV. On the way from the source to the target, two superconducting solenoids and two Beam Line Polarimeters are installed to control and monitor the magnitude and direction of the beam polarization. The scattering chamber is connected to two spectrometer. The Large Acceptance spectrometer (LAS) is used to monitor the vertical beam position. With the Grand Raiden Spectrometer, which consists of two dipole magnets (D1 and D2), a multipole magnet (MX) and a dipole magnet for spin rotation (DSR) the scattered protons were analyzed in the focal plane. With the help of the Focal Plane Polarimeter (FPP) polarization transfer observables of protons which were scattered at a carbon block between the focal plane and the FPP can be extracted.

---

## 11.1 Beam line polarimeters (BLPs)

---

With the two beam line polarimeters BLP1 and BLP2 the polarization of the proton beam was monitored periodically. Each BLP consists of four pairs of plastic scintillators in order to measure the p-p scattering asymmetries of a polyethylene foil. As an example, figure 11.2 shows the top view of one of the BLPs measuring the left-right asymmetry. A similar setup can be found for the up-down asymmetry. To experimentally determine the scattering asymmetry, elastic scattering off hydrogen and quasi-elastic scattering off carbon (which both have the same kinematics) are measured in coincidence with recoiling protons from the target. The analyzing power of the BLPs for proton scattering at 295 MeV has been measured to be  $A_y = 0.40 \pm 0.01$  [Tak02].

In order to detect all three-dimensional polarization components of the beam, a configuration of two BLPs and a  $50^\circ$  dipole magnet as shown in figure 11.3 has been used. Each 99 seconds, the polyethylene target was inserted for 10 seconds into the beam. During that time, the readout electronic was inactive.

---

## 11.2 The setup for $0^\circ$ measurements

---

---

### 11.2.1 The Grand Raiden spectrometer

---

The Grand Raiden spectrometer [Fuj99] consists of a Q1-SX-Q2-D1-MP-D2+DSR magnet configuration, where D, Q and SX stand for dipole, quadrupole and sextupole, respectively, and MP denoting a multipole magnet. Additionally, the DSR (Dipole for spin rotation) magnet has been

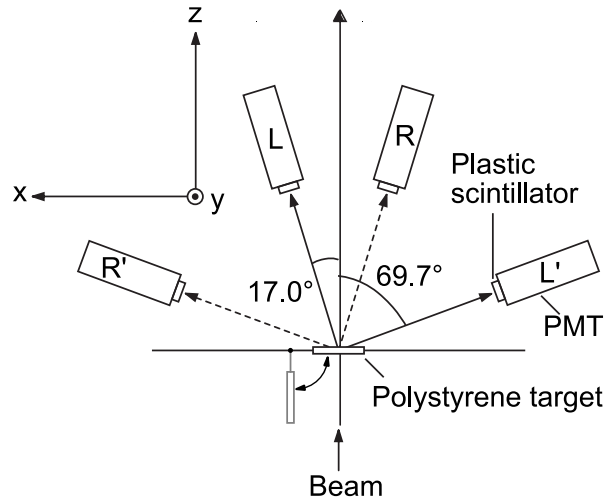


**Figure 11.2.:** Schematic view of one beam line polarimeter (BLP).

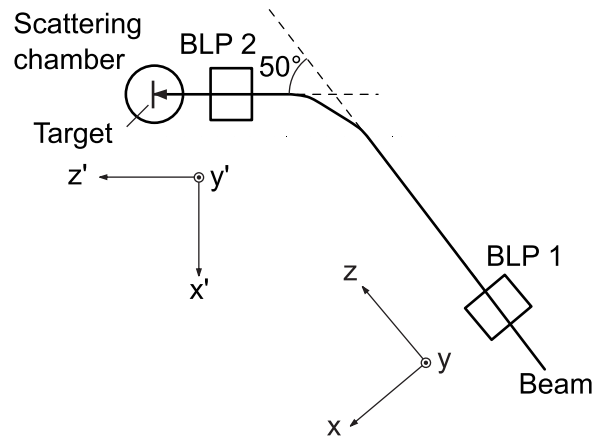


**Figure 11.3.:** Arrangement of the two beam line polarimeters for the determination of the beam polarization at the target position.

utilized during the measurement with longitudinal polarization. In the so-called DSR+ mode it is possible to bend the scattered proton beam additionally by + 18° without affecting the resolving power of the Grand Raiden spectrometer. A schematic view of the Grand Raiden spectrometer can be seen on the left hand side of figure 11.4. With its high momentum resolution of  $p/\Delta p \approx 37000$  at a momentum acceptance of  $\pm 2.5\%$  the Grand Raiden spectrometer is one of the worlds best spectrometer for proton scattering experiments. In table 11.1, all the important specifications of the spectrometer are listed.

As one can also see in figure 11.4 the detector system of the Grand Raiden spectrometer consists of two major components. Directly behind the DSR magnet, the Focal Plane Detector System with its vertical drift chambers (VDCs) and its plastic scintillators is situated. The second part is the Focal Plane Polarimeter. Two different Faraday cups have been used during the measurement campaign. For the polarized proton measurements at 0° the 0° FC is used with its extra

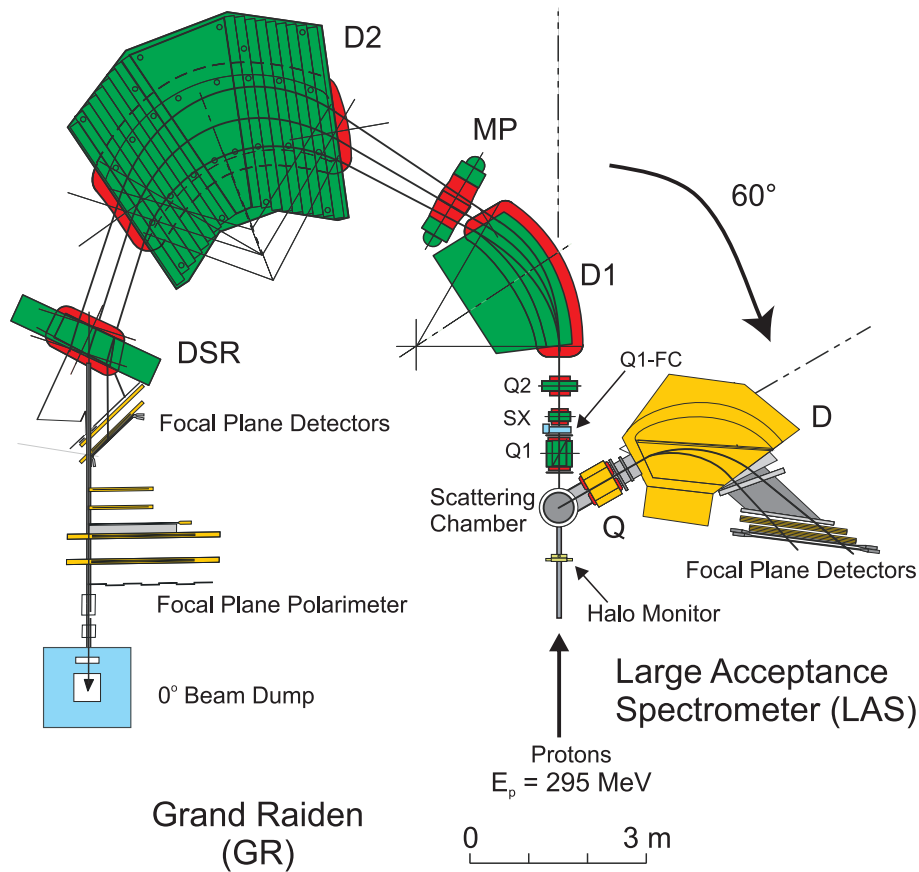


**Figure 11.4.:** Setup for  $0^\circ$  experiments.

steering magnet for sweeping away low energy electrons that are created upstream. The other Faraday cup (Q1-FC) has been used during the finite angle measurement at  $3^\circ$ .

### 11.3 The Large Acceptance Spectrometer (LAS)

The Large Acceptance Spectrometer [Mat91] with solid angle of 20 msr and a momentum resolution of  $p/\Delta p \approx 5000$  consists of a quadrupole magnet and a dipole magnet. Further properties of the LAS can be found in table 11.1. A schematic view of the LAS is presented on the right hand side of figure 11.4. The focal plane detector system of the LAS consists of pairs of multi-wire drift chambers and two planes of plastic scintillators as trigger detectors. During this experiment, the LAS has been set at a scattering angle of  $60^\circ$  to monitor the vertical beam position, since it provides a large vertical magnification of 7.3. An entrance collimator has been installed to reduce the vertical angular acceptance of the LAS to  $\pm 6$  mr which improved the beam position resolution. With this setup one was able to detect a  $\pm 0.01$  mm shift of the beam position.



**Table 11.1.: Specifications of GR and LAS spectrometer**

	Grand Raiden (GR)	Large Acceptance spectrometer (LAS)
Configuration	QSQDMDD	QD
Mean orbit radius	3 m	1.5 m
Total deflecting angle	180°	70°
Tilting angle of focal line	45°	57°
Maximum magnetic rigidity	5.4 Tm	3.2 Tm
Vertical magnification	5.98	-7.3
Horizontal magnification	-0.417	-0.4
Momentum range	5 %	30 %
Momentum resolution	37 075	4 980
Acceptance of horizontal angle	±20 mr	±60 mr
Acceptance of vertical angle	±70 mr	±100 mr

## 11.4 Detector systems at the 0° scattering facility

The detector system at the Grand Raiden spectrometer consists of the Focal Plane Detector System [Nor90] and the Focal Plane Polarimeter [Yos95]. Figure 11.5 shows a schematic view of the detector system with the Focal Plane Detector System in the upper part and the Focal Plane Polarimeter in the central part. The Focal Plane Detector System has been used to reconstruct the trajectories of the scattered protons in order to calibrate scattering angles and excitation energies, while the Focal Plane Polarimeter was used to determine the polarization of the scattered protons.

### 11.4.1 The Focal Plane Detector System

During the first scattering process at the target position in the scattering chamber of the spectrometer the protons lose energy due to the excitation of the target nuclei. Because of the Lorentz force, the protons that have less energy are deflected more in the dipole field of the spectrometer and in the focal plane the scattered protons can be mapped by their momentum. The Focal Plane Detector System consists of two Vertical Drift Chambers (VDCs) and a plastic scintillator (PS1) of 3 mm thickness. More technical details of the VDCs (from the Grand Raiden spectrometer and the Large Acceptance Spectrometer) can be found in table 11.2.

In the two VDCs of the Focal Plane Detectors the intersection points at the focal plane  $x_{fp}$  and  $y_{fp}$  and also the intersection angles  $\theta_{fp}$  and  $\phi_{fp}$  are determined.

When charged particles like the scattered protons pass the drift chamber, they ionize the gas mixture and create electron-ion pairs. Each VDC consists of two times 192 sense wires (X and U) that are placed between three cathode planes and by measuring the drift times of the

electrons in these wires, and combining the information of all VDCs it is possible to reconstruct the intersection points of the scattered protons in the focal plane. So in the X1 and X2 plane informations on the dispersive observables  $x_{fp}$  and  $\theta_{fp}$  are collected while the U1 and U2 planes are tilted by an angle of  $48.19^\circ$  with respect to the X planes, providing informations about the non-dispersive observables  $y_{fp}$  and  $\phi_{fp}$ . The cathode planes of the VDCs are set of a high voltage level of -5.6 kV, the potential wires on a voltage level of -0.3 kV and the sense wires are set at ground level. Further technical properties of the VDCs are summarized in table 11.2.

**Table 11.2.:** Technical details of the VDCs in the Grand Raiden and the Large Acceptance Spectrometers

	Grand Raiden	Large Acceptance spectrometer
Wire configuration	X ( $0^\circ$ ), U ( $48.19^\circ$ )	X ( $0^\circ$ ), U ( $-31^\circ$ ), V ( $+31^\circ$ )
Active area, mm <sup>2</sup>	$1150^W \times 120^H$	$1700^W \times 350^H$
Number of sense wires	192 (X), 208 (U)	272 (X), 256 (U,V)
Anode-cathode gap	10 mm	10 mm
Anode wire spacing	2 mm	2 mm (X), 2.33 mm (U,V)
Sense wire spacing	6 mm (X), 4 mm (U)	6 mm (X), 7 mm (U,V)
Applied voltage	-5.6 kV (cath.), -0.3 kV (pot.)	-5.5 kV (cath.), -0.3 kV (pot.)
Entrance and exit window	12.5 $\mu$ m carbon aramid film	25 $\mu$ m carbon aramid film
Sense wires	20 $\mu$ m $\varnothing$ gold-plated tungsten wire	
Potential wires	50 $\mu$ m $\varnothing$ gold-plated beryllium-copper wire	
Cathode	10 $\mu$ m carbon-aramid film	
Gas mixture	argon (70%) + isobutane (30%) + isopropyl alcohol	

#### 11.4.2 The Focal Plane Polarimeter (FPP)

For the polarization measurements, the Focal Plane Polarimeter has been used. The first scattering process took place in the scattering chamber and right before the Focal Plane Polarimeter a carbon slab of 9 cm thickness was inserted, where a secondary scattering process occurred. The spin-orbit interaction between the scattered protons and the  $^{12}\text{C}$  nuclei lead to an azimuthal asymmetry in the secondary scattering process which can be very well analyzed in the Focal Plane Polarimeter. Here, the measured asymmetry in the focal plane of the Focal Plane Polarimeter is combined with the spin-transfer matrix of the spectrometer. With this method one is able to determine the polarization of the initial reaction vertex. The FPP is equipped with four multi-wire proportional chambers (MWPCs), one pair before and one pair behind the carbon slab. A plastic scintillator (PS2) and a hodoscope (HS) also serve here as trigger detectors. While MWPC1 and MWPC2 only have X planes, MWPC3 and MWPC4 consist of X, U and V planes. Table 11.3 gives a summary of the technical details of the MWPCs used in the Focal Plane Polarimeter.

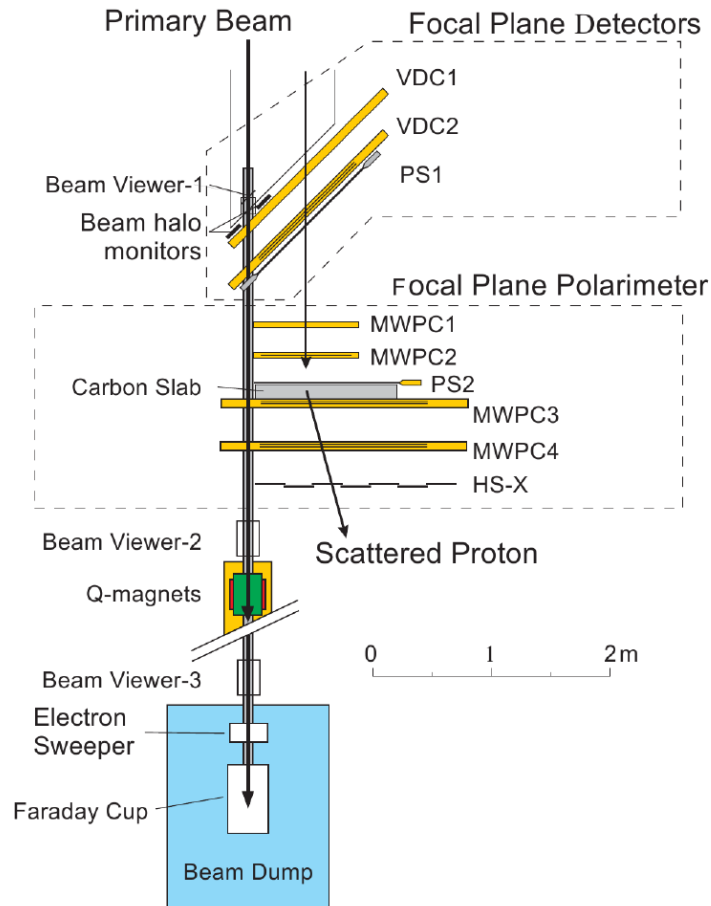


**Figure 11.5.:** Schematic view of the detector system at the Grand Raiden spectrometer. The Focal Plane Detectors are shown in the upper part, and in the center part, the Focal Plane Polarimeter is shown.

**Table 11.3.:** Technical details of the MWPCs in the Focal Plane Polarimeter

	MWPC 1,2	MWPC 3	MWPC 4
Wire configuration	X (0°)	X (0°), U (-45°), V (+45°)	
Active area, mm <sup>2</sup>	760 <sup>W</sup> × 200 <sup>H</sup>	1400 <sup>W</sup> × 418 <sup>H</sup>	1400 <sup>W</sup> × 600 <sup>H</sup>
Number of wires	384	704 (X) × 640 (U,V)	704 (X,U,V)
Anode-cathode gap		6 mm	
Sense wire spacing		2 mm	
Applied voltage	-4.9 kV		-4.7 kV
Sense wires		25 μm Ø gold-plated tungsten wire	
Cathode	10 μm carbon-aramid	6 μm aluminized mylar	
Gas mixture	argon (66%) + isobutane (33%) + freon (0.3%) + isopropyl alcohol		

## 11.5 Experimental conditions

The experiment was performed in May 2011 within three weeks. The main experiment was the  $(\vec{p}, \vec{p}')$  scattering on  $^{154}\text{Sm}$  while also unpolarized measurements on the semi-magical nucleus

$^{144}\text{Sm}$  have been performed [Mar11].

At first, 4 days of intense beam tuning had to be done in order to deliver a halo-free polarized proton beam with a very high energy resolution using the technique of lateral and angular dispersion matching. In the first three days, the measurements at  $^{154}\text{Sm}$  with a transversally polarized proton beam at  $0^\circ$  have been done. Then, the beam polarization was switched by using solenoids to a longitudinal polarization and again three days were needed to measure with sufficient statistical uncertainties.

Then the ion source was switched to an unpolarized ion source, as the beam current of the polarized source HIPIS was limited to roughly  $2\text{ nA}$ . The ion source NEOMAFIOS could achieve higher beam currents and for the further measurements no polarized beam was needed. Therefore the Focal Plane Polarimeter downstream of the Grand Raiden spectrometer was switched off in order to reduce the increase of the dead time. With the unpolarized source the  $0^\circ$  measurement for  $^{144}\text{Sm}$  has been done and then the Grand Raiden spectrometer was rotated to  $3^\circ$  to measure the data that was needed for the angular distribution measurement. The last day was used for calibration measurements which were needed to calibrate the ion optics of the Grand Raiden spectrometer. Here, elastic proton scattering was measured with a sieve slit target under  $16^\circ$ . Additionally, elastic scattering runs for determination of target thicknesses were performed at  $10^\circ$ .

The polarization of the beam was stable throughout the experiment and in the order of 65-70%. Tables 11.4 and 11.5 summarize the experimental conditions.

**Table 11.4.:** Summary of the experimental conditions during this experiment

Proton beam energy	295	MeV
Energy resolution (achromatic, $^{197}\text{Au}$ and $^{27}\text{Al}$ )	40	keV
Energy resolution (dispersive with faint beam)	18	keV
Energy resolution (dispersive, $^{208}\text{Pb}$ )	25	keV

**Table 11.5.:** Summary of the experimental conditions in each measurement

Measurement	$0^\circ$	forward angle	elastic
Transport mode	dispersive	dispersive	achromatic
GR angle	$0^\circ$	$3^\circ$	$9^\circ, 10^\circ, 12^\circ, 13.5^\circ, 16^\circ$
Beam intensity	6 nA	6 nA	6 nA

## 11.6 Used targets

The targets, that have been used were highly enriched self-supporting metallic foils with an isotopic enrichment of 98.69% and an areal density of  $4.0\text{ mg/cm}^2$  in the case for  $^{154}\text{Sm}$  and for  $^{154}\text{Sm}$ . For checking the energy resolution of the beam a short measurement with  $^{26}\text{Mg}$  was

done before each Sm-run. These Mg-runs were also used to check if the incoming proton energy has shifted slightly which corresponds to a shift of the excitation spectra due to the nature of the dispersion matching of the spectrometer.

At the beginning a Gold foil was used to check the beam resolution utilizing the faint beam method. For the sieve-slit calibration runs a very thick  $^{58}\text{Ni}$  target with a thickness of  $100.1 \text{ mg/cm}^2$  has been used. Figure 11.6 shows the target ladder as it was used during the experiment.

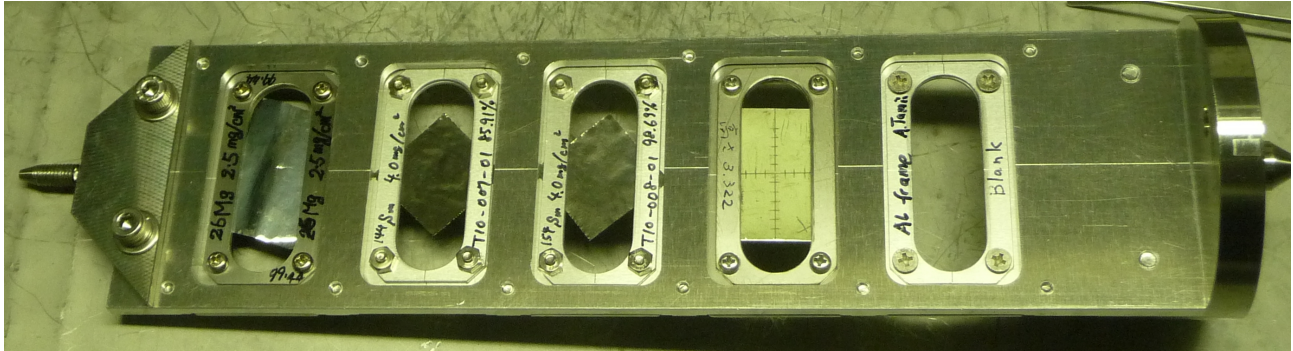


**Figure 11.6.:** Targetladder which was used during the experiment. Targets from left to right:  $^{26}\text{Mg}$ ,  $^{144}\text{Sm}$ ,  $^{154}\text{Sm}$ , ZnS and empty frame.

### 11.6.1 The under-focus mode

To obtain a good scattering angular resolution the so called under-focus mode has been used. The precise determination of the scattering angle in horizontal (dispersive) and vertical (non-dispersive) direction plays a crucial role since no entrance collimator has been used to avoid the production of additional background events. The total scattering angle at the focal plane is given by

$$\theta_{fP} = \sqrt{(\theta_t + \theta_{GR})^2 + \phi_t^2} \quad (11.1)$$

where  $\theta_t$  and  $\phi_t$  are the horizontal and the vertical scattering angles at the target position whereas  $\theta_{GR}$  is the angle of the Grand Raiden spectrometer. When applying the normal magnetic field settings (see normal-focus mode in figure 11.7) vertical and horizontal scattering angles of the scattered protons are focused at the focal plane. In order to prevent the loss of acceptance that would occur due to the small magnification factor of the Grand Raiden spectrometer, resulting in a bad vertical scattering angle resolution a vertical off-focus mode was applied. Therefore the field of the Q1 magnet has been decreased by 5%. The lower picture in figure 11.7 depicts the optical path of the protons.

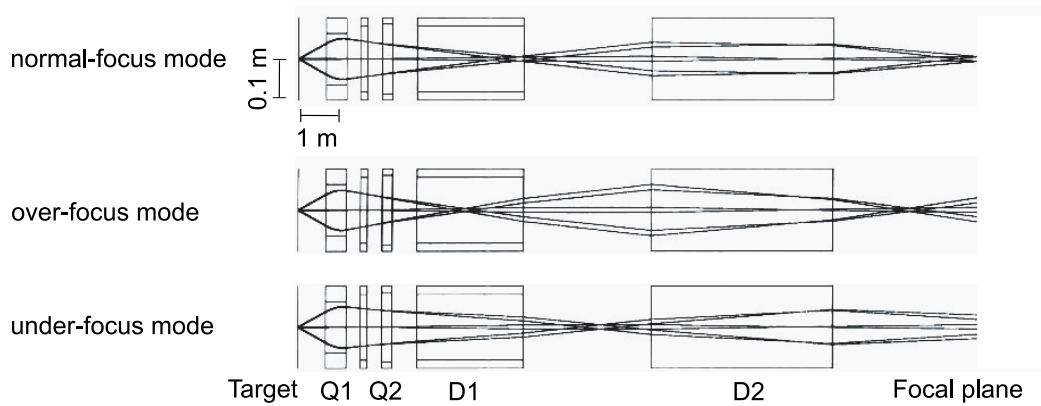


**Figure 11.7.:** Examples of vertical beam envelopes in the  $y$ - $z$  plane with three different focus modes of the Grand Raiden optics.

---

### 11.6.2 The Faraday cups

---

Three different kinds of Faraday cups have been used during the experiment to monitor the proton beam current and to measure the collected charge in the spectra. The  $0^\circ$  Faraday cup behind the focal plane detectors for measurements at extreme forward angles, the Q1-FC for the measurement at  $3^\circ$  and the scattering chamber Faraday cup (SC-FC) for the elastic scattering experiments at higher angles in the dispersive mode. To correct for little losses in the beam charge collection, the beam transmission from the target to the  $0^\circ$  FC was checked. The absolute efficiency for the charge measurement at the SC-FC has been already calibrated [Fuj08] with respect to the rates measured in the BLPs and so it can be used as a reference because the other Faraday cups can be corrected relative to it. The ratio of the total events in BLP to the collected charges was measured for each Faraday cup. If transmission losses occurred during the experiment, then the ratio of the  $0^\circ$  FC and the Q1-FC would become larger than that of the SCFC. This calibration procedure has been validated in [Mat10] and the resulting correction factors enter in the determination of the double differential cross sections.

---

### 11.6.3 The sieve-slit measurements

---

To reconstruct the scattering angles at the target position from the data obtained by the Focal Plane Detector system it is necessary to perform a calibration run for the complicated ion optics of the Grand Raiden spectrometer. This can be done by the so-called sieve slit method. A 5 mm thick brass plate (the 'sieve slit') with 25 holes was inserted at the beam line 638 mm downstream of the target position. Figure 11.8 shows a schematic overview of the brass plate. All holes are aligned in a  $5 \times 5$  matrix with a horizontal distance of 4.5 mm (corresponding to 7 mrad) and a vertical distance of 12 mm (corresponding to 19 mrad). For a better adjustment, the center hole had a diameter of 3 mm (4.7 mrad), while all the other holes were only 2 mm

(3.1 mrad) in diameter. As scattering target a 100 mg/cm<sup>2</sup> thick <sup>58</sup>Ni foil has been used. Elastic proton scattering was then performed at an Grand Raiden angle of 16°. At the focal plane the protons that were scattered through one of the slits could be detected and so in the offline analysis, the vertical position and the scattering angle at the focal plane could be directly related to their well-known geometrical position. To account for the dependence of the scattering angles on the horizontal position at the focal plane, the magnetic field was varied in discrete steps. So short measurements at +1.2%, +1.8%, +2.6%, +3.4% and +4.2% have been performed relative to the standard under-focus setting of the ion optics. These values correspond to excitation energies of 6, 10, 14, 18 and 22 MeV, respectively. So, the full excitation energy range investigated in this experiment could be covered. Each of the measurements has been done also at a vertical beam spot shift of ±1 mm in order to determine the influence of the beam position on the target. The sieve slit calibration of this experiment has already been discussed in [Mar11] and will be shown in section 12.1.3.

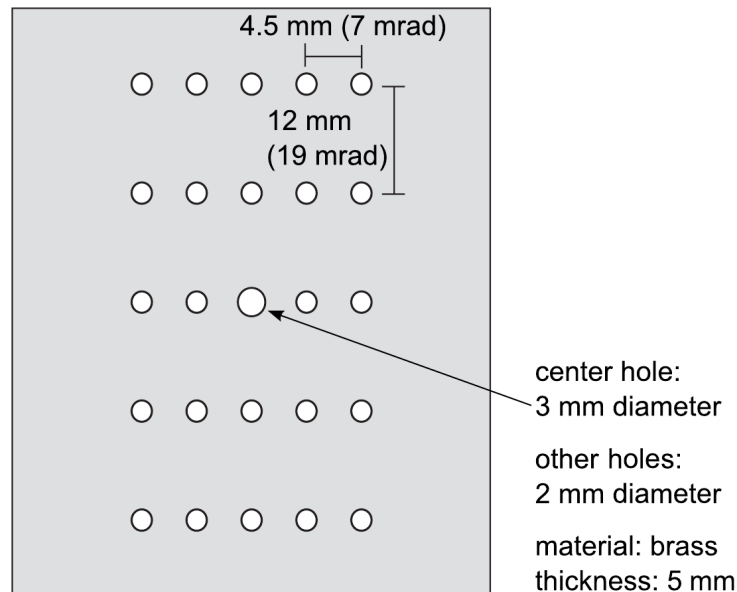


**Figure 11.8.:** Schematic view of the brass plate that has been used for the sieveslit measurements.





---

## 12 Data analysis for proton scattering

---

For the data analysis of the  $^{154}\text{Sm}$  data, the program code ANALYZER [Tam99] which was developed at the RCNP has been used. This software package is adapted for the online and offline analysis of data, taken at the GR spectrometer and LAS. It is written mainly in the program language C and makes use of the HBOOK and PAW(++) packages of the CERN libraries [CER].

---

### 12.1 Data reduction

---

The data reduction procedure has been performed step by step according to the table below and will be explained more detailed on the following pages:

- Drift time to distance conversion
- Efficiency determination of the VDCs
- Calibration of scattering angles
- Kinematical corrections and excitation energy calibration
- Higher order aberration corrections
- Subtraction of background
- Cross section determination
- Analysis of polarization transfer observables

Some parts of the data reduction procedure have already been discussed in [Mar11].

---

#### 12.1.1 Drift time to distance conversion

---

Vertical drift chambers (VDC) are used for measuring the scattered proton positions. This is necessary to obtain the trajectory of the particles for determining the angles and excitation energies with which particles go through the focal plane. In figure 12.1 a schematic view of a vertical drift chamber is presented. The typical VDC consists of two cathode foils and in between a layer of wires. Besides the sense wires or signal wires, most of the VDCs also have potential wires which are used to shape the electric field and to prevent possible cross talk between different channels. In general, when charged particles go through the detector they interact with gas molecules and ionize them. The electrons drift towards the anode plane with an almost constant drift velocity of  $\approx 5 \text{ cm}/\mu\text{m}$ . Consequently, the drift times are proportional

to the distance from the ionization point to the sense wire.

In this experimental setup the drift chambers work in the so-called common stop mode which means that a Time-to-Digital Converter (TDC) is used to measure the time difference between the wire signal and the corresponding delayed trigger signal from the plastic scintillator PS1. Taking into account the signals of multiple adjacent wires and performing a proper conversion of the TDC values into the corresponding drift length, the intersection point in each single VDC plane can be determined. For this purpose a 'white' spectrum with homogeneously distributed events was measured which is shown in the upper part of figure 12.2. The lower panel of this figure shows the drift length histogram which has a flat distribution. Figure 12.3 shows the proportionality between the TDC channels and the drift length. At large TDC channels, deviations from the linear behaviour can be observed which is due to the inhomogeneity of the electric field in the vicinity of the sense wires.

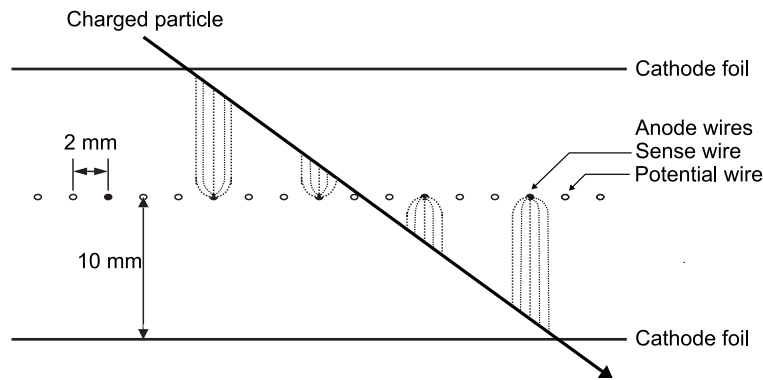


**Figure 12.1.:** Vertical drift chamber as a schematic view. Picture is taken from [Mar11].

To make sure that at least two or more signals are obtained from the sense wires, the VDCs are installed under an angles of  $45^\circ$ . Additionally, neighbouring events are combined to clusters. Clusters with only one single hit are discarded and also the wire with the shortest signal is omitted, since the non-uniformly electric field near the sense wires leads to unwanted uncertainties in the drift time to drift length conversion. A least-square fit from the drift length of the wire signals is used to calculate the intersection point of the proton trajectory at a single wire plane. Finally, with a combination of all wire planes it is possible to determine the trajectory and the scattering angle of the protons.

---

### 12.1.2 Efficiency determination of the VDCs

---

The efficiency of one single VDC plane is determined by the following equation, as an example for the X1 plane:

$$\epsilon_{X1} = \frac{N_{X1,X2,U1,U2}}{N_{X1,X2,U1,U2} + N_{\bar{X1},X2,U1,U2}}. \quad (12.1)$$

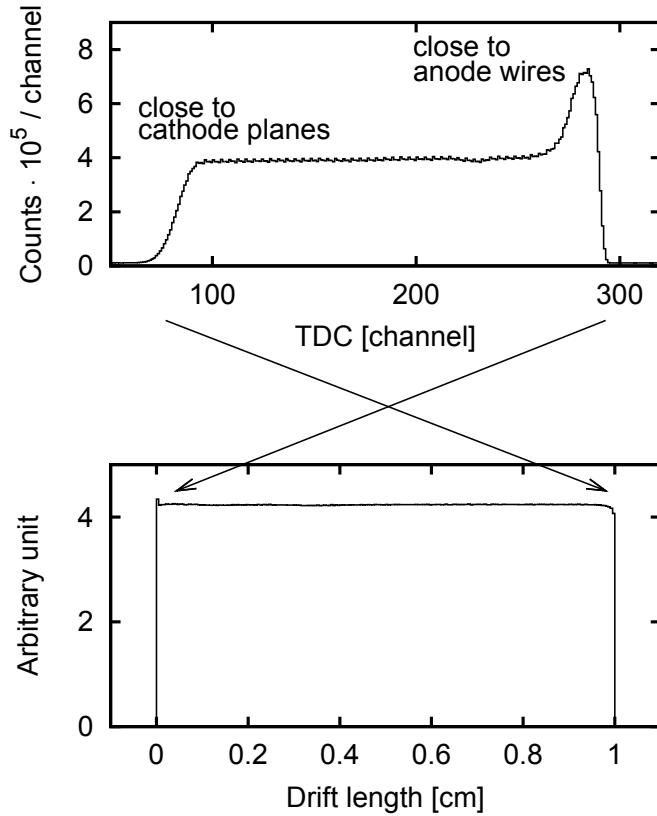


**Figure 12.2.:** Example of the track reconstruction. The upper panel shows a typical TDC spectrum. In the lower panel the corresponding drift length is shown.

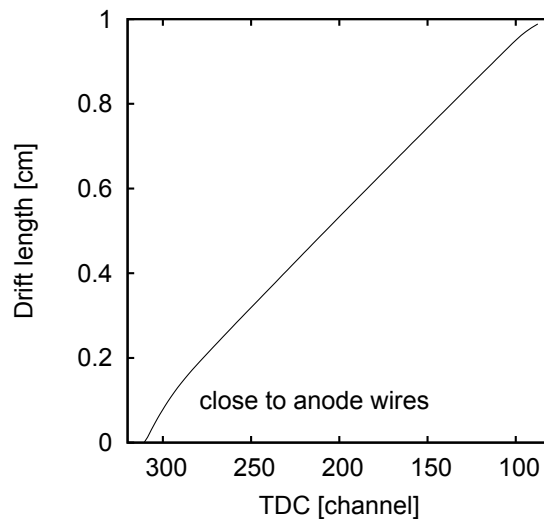


**Figure 12.3.:** Drift time to drift length conversion.

Here,  $N_{\overline{X1},X2,U1,U2}$  is the number of events, in which the cluster position can be determined for all planes and  $N_{X1,X2,U1,U2}$  for all but the X1 plane. The total efficiency  $\epsilon_{tot}$  is then determined by the product of all four efficiencies:

$$\epsilon_{tot} = \epsilon_{X1} \cdot \epsilon_{X2} \cdot \epsilon_{U1} \cdot \epsilon_{U2} \quad (12.2)$$

In this experiment the total detection efficiency of the VDCs has been determined to be 88%.

### 12.1.3 Sieve slit analysis

The scattering angles at the target position  $\theta_t$  and  $\phi_t$  can be extracted by performing a so called sieve slit analysis. As an input for such a calculation the interaction points and scattering angles at the focal plane are necessary. The horizontal scattering angle  $\theta_t$  at the target place is mainly dominated by the horizontal incident angle at the focal plane  $\theta_{fp}$ . In the vertical plane, the scattering angle  $\phi_t$  dominates the vertical position  $y_{fp}$  at the focal plane. The LAS spectrometer has been used for determining the vertical position at the target chamber  $y_{LAS}$  (see figure 12.4(b)) and hence, this quantity needs also to be considered. Additionally, both of the scattering angles depend on the horizontal position  $x_{fp}$  at the focal plane.

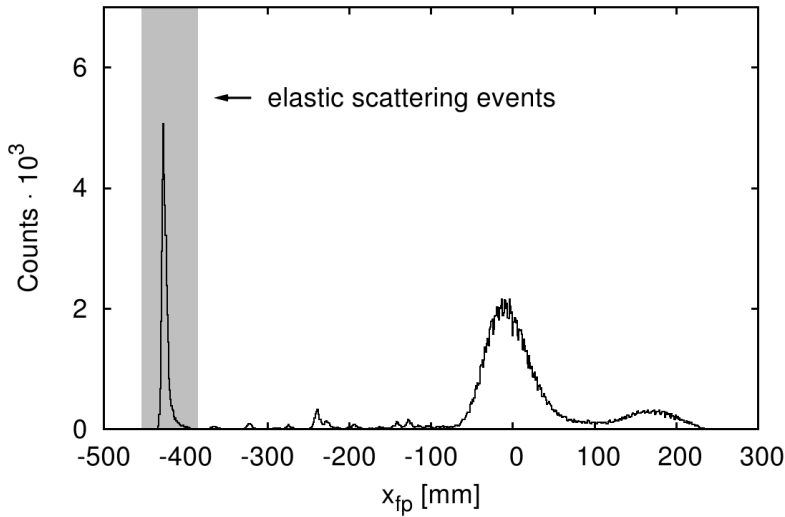
Figure 12.4(a) shows a spectrum of the elastically scattered events. The gate on  $x_{fp}$  which has been used for the sieve slit analysis is here illustrated in grey. The bump at around  $x_{fp}$  comes from elastically scattered events that pass through the thick brass plate with an energy loss of about 10 MeV. Figure 12.4(c) shows the  $\theta_{fp} - y_{fp}$  plane gated on the elastic events. In order to obtain the coordinates of the 25 spots in figure 12.4(c) the figure was sliced horizontally and vertically in five rectangles (see also the grey bars in figure 12.4(c)). Each of the vertical slices was then projected on the  $\theta_{fp}$  axis, whereas each horizontal slice was projected onto the  $y_{fp}$  axis. Assuming a circular shape of the hole images, gaussian fits for the  $\theta_{fp}$ - and  $y_{fp}$ -positions of the spots were applied. Afterwards the correlation between  $\theta_{fp}$  and  $\phi_{fp}$  was investigated by setting specific gates on  $\theta_{fp}$ . Figure 12.4(d) then shows a projection of the events onto the  $\phi_{fp}$  axis utilizing gaussian fits.

In the end a multi-dimensional least square fit routine using the GNU scientific library (GSL) [Gal03] was used to determine the vertical and the horizontal scattering angles.

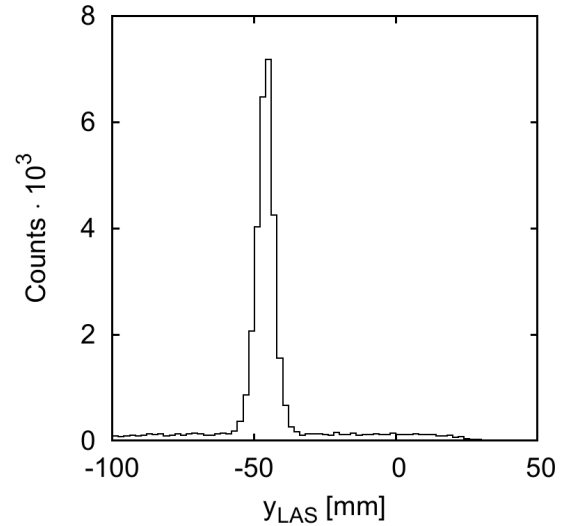
$$\theta_t(x_{fp}, \theta_{fp}) = \sum_{i=0}^1 \sum_{j=0}^1 a_{ij} \cdot x_{fp}^i \theta_{fp}^j \quad (12.3)$$

$$\phi_t(x_{fp}, \theta_{fp}, y_{fp}, \phi_{fp}, y_{LAS}) = \sum_{i=0}^1 \sum_{j=0}^1 \sum_{k=0}^1 \sum_{l=0}^1 b_{ijkl} \cdot x_{fp}^i \theta_{fp}^j y_{fp}^k \phi_{fp}^l + \sum_{m=0}^1 c_m \cdot x_{fp}^m y_{LAS} \quad (12.4)$$

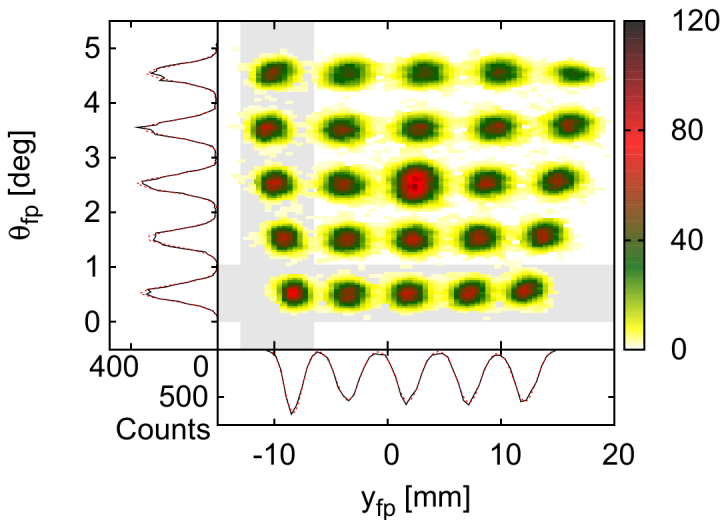
Equations 12.3 and 12.4 are implemented in the multidimensional fit and the resulting coefficients for this experiment are listed in table 12.1. The final reconstruction of the vertical and horizontal scattering angle can be seen in figure 12.1.3 where the left hand side shows the uncorrected images and the right hand side shows the images of the 25 holes after the complete sieve slit calibration.



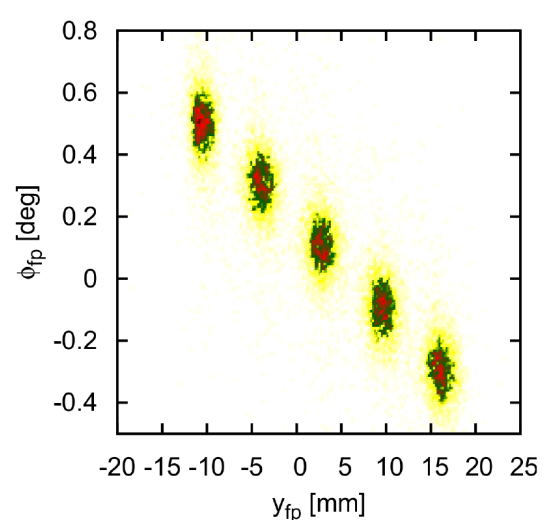
(a) Gate for elastic scattering events.



(b) Vertical position of the beam monitored in the LAS spectrometer.



(c) Horizontal scattering angle at the focal plane  $\theta_{fp}$  against  $y_{fp}$ .



(d) Vertical scattering angle at the focal plane  $\phi_{fp}$  against  $y_{fp}$ .

**Figure 12.4.:** Extraction of  $y_{LAS}$ ,  $\theta_{fp}$ ,  $y_{fp}$  and  $\phi_{fp}$  from the sieve slit analysis.

With the help of an optical position determination method the offset coefficients  $a_{00}$  and  $b_{0000}$  from table 12.1 have been determined at the beginning of the beam time.

#### 12.1.4 Higher order aberration corrections

The reaction kinematics for  $^{154}\text{Sm}$  were calculated with KINMAT [KIN] and afterwards fitted with gnuplot [GNU]. The following relation shows the results of the fit for elastically scattered protons with an energy of 295 MeV:

**Table 12.1.:** Table of coefficients for Eqs. (12.3) and (12.4) for the reconstruction of scattering angles. The numbers of  $i$ ,  $j$ ,  $k$  and  $l$  represent the exponent of  $x_{fp}$ ,  $\theta_{fp}$ ,  $y_{fp}$  and  $\phi_{fp}$ , respectively. All angles are given in radian and all distances in mm. The omitted coefficients are set to zero.

$i j$	coefficients $a_{ij}$
00	$3.380 \cdot 10^{-2}$
01	$-3.958 \cdot 10^{-1}$
10	$3.837 \cdot 10^{-5}$

$i j k l$	coefficients $b_{ijkl}$
0000	$-4.619 \cdot 10^{-2}$
0001	2.681
0010	$-1.529 \cdot 10^{-3}$
1000	$2.590 \cdot 10^{-5}$

$m$	coefficients $c_m$
0	$-1.012 \cdot 10^{-3} \cdot y_{LAS}$
1	$4.130 \cdot 10^{-7} \cdot y_{LAS}$

$$E(\theta) = -6.80 \cdot 10^{-4} \theta^2 \text{ MeV/deg}^2 + 295 \text{ MeV.} \quad (12.5)$$

Although a proper sieve slit calibration has been performed, there still remains an interconnection between  $\theta_{fp}$  and  $x_{fp}$  due to the ion-optical properties of the Grand Raiden spectrometer. To get rid of this dependency causing a bad energy resolution, several spectra of  $^{26}\text{Mg}$  with well-known discrete peaks were analyzed in the excitation energy region between 9 MeV and 13 MeV [Tam07]. The upper picture in figure 12.6 shows the  $x_{fp} - \theta_{fp}$  plane in which the discrete peaks show up as curved lines. In order to straighten these lines and improve the momentum information, a polynomial function

$$x_c = x_{fp} + \sum_{i=0}^1 \sum_{j=1}^4 d_{ij} \cdot x_{fp}^i \theta_{fp}^j \quad (12.6)$$

was fitted to each curved line. The corrections of equation 12.6 can be applied and the lower part of figure 12.6 shows the result. One clearly can see how the resolution in  $x_c$  improves. The coefficients for equation 12.6 are listed in table 12.2.

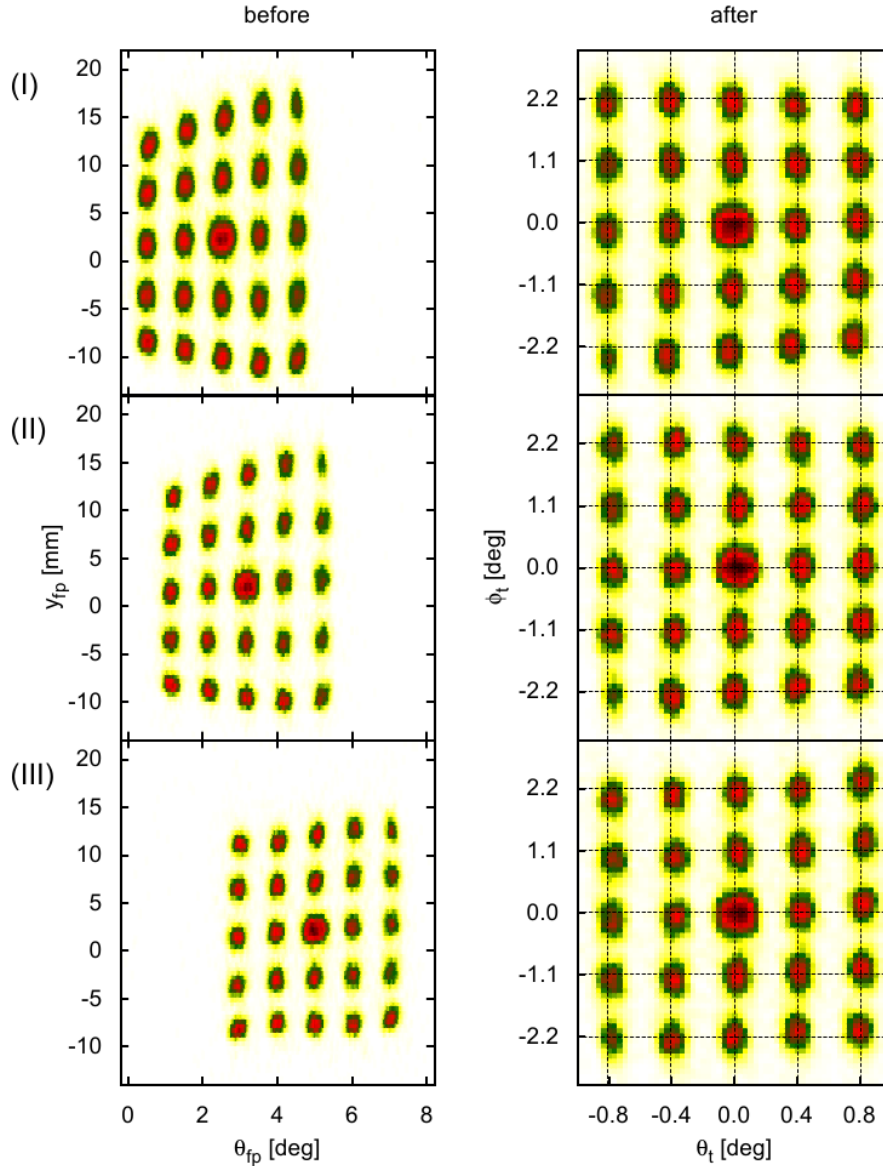


**Figure 12.5.:** Two-dimensional  $y - \theta$  histograms before and after corrections according to equations (12.3) and (12.4) and using the parameters of table. 12.1. The images (I), (II) and (III) correspond to kinetic energies of 6, 10 and 18 MeV, respectively. The crossings of dotted lines in the right part represent the actual holes in the sieve slit. Due to the calibration the center of the events should coincide with the crossing points.

---

### 12.1.5 Excitation energy calibration

---

For the energy calibration procedure six well-known transitions in the  $^{26}\text{Mg}$  excitation energy spectra were used. Their positions  $x_c$  were obtained by using gaussian fits and the corresponding excitation energy was taken from the Evaluated Nuclear Structure Data File (ENSDF) [ENS13]. Table 12.3 summarizes the data used for the excitation energy calibration which leads to the following linear relation:

**Table 12.2.:** Table of coefficients for equation (12.6) for the correction of  $x_{fp}$ . The numbers of  $i$  and  $j$  represent the exponent of  $x_{fp}$  and  $\theta_{fp}$ , respectively. All angles are given in radian and all distances in mm.

$i j$	coefficients $d_{ij}$
01	$-2.856 \cdot 10^2$
02	$-1.784 \cdot 10^3$
03	$4.607 \cdot 10^4$
04	$-1.960 \cdot 10^5$
11	$8.515 \cdot 10^{-1}$
12	$-4.269 \cdot 10^1$
13	$5.073 \cdot 10^2$
14	$-1.938 \cdot 10^3$

$$E_x(x_c) = 23.93 \cdot 10^{-3} \text{ MeV/mm} \cdot x_c + 17.14 \text{ MeV.} \quad (12.7)$$

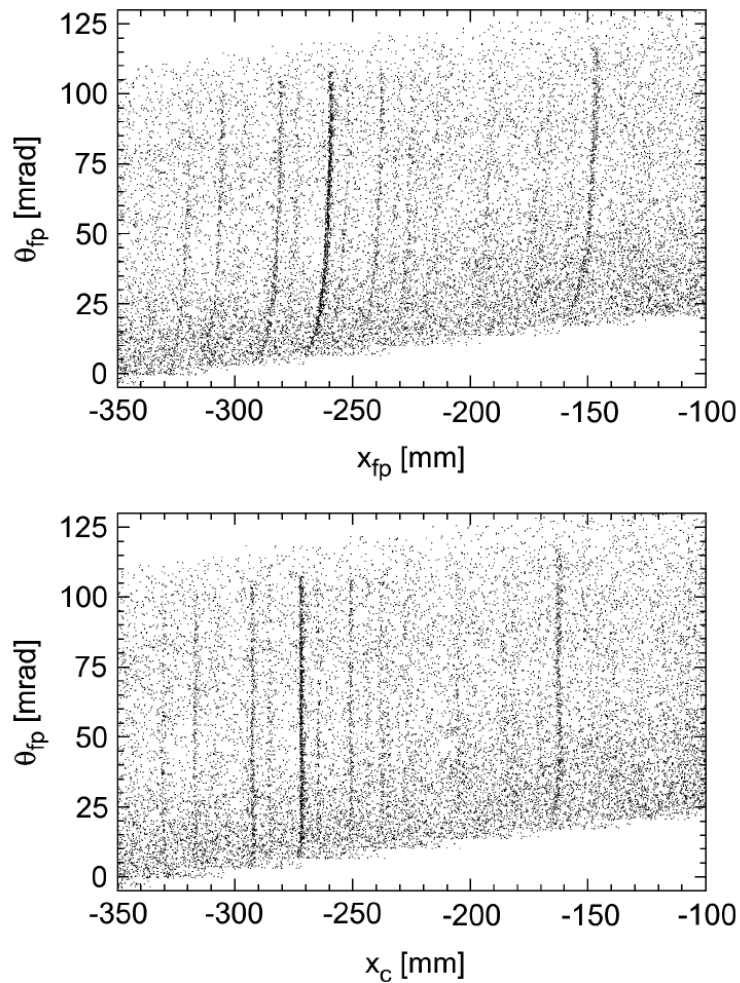


**Figure 12.6.:** Two-dimensional histograms of the  $x_{fp} - \theta_{fp}$  plane for the  $^{26}\text{Mg}(p, p')$  reaction before the software corrections (top) and after the straightening of the lines (bottom), with a fit to equation (12.6).



**Table 12.3.:** Transitions used for the energy calibration. All corrected horizontal positions are given in mm and all corresponding excitation energies taken from [ENS13] in keV.

$x_c$	$\Delta x_c$	$E_x$	$\Delta E_x$
-319.743	0.044	9238.7	0.5
-305.908	0.035	9560	3
-280.900	0.021	10148	2
-273.700	0.020	10319	2
-259.583	0.012	10645	2
-252.487	0.037	10805.9	0.4

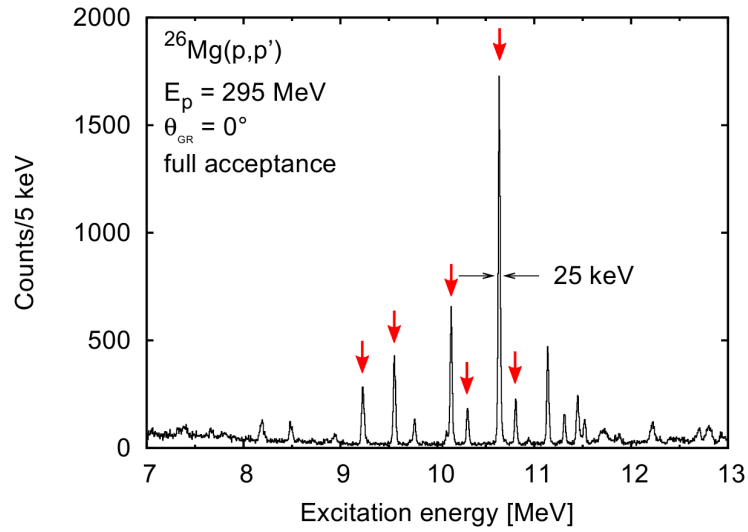


**Figure 12.7.:** Excitation energy calibration with the  $^{26}\text{Mg}(p, p')$  reaction. The peaks, which were chosen for a least square fit (see table 12.3), are indicated by red arrows. Here, the energy resolution was 25 keV (FWHM).

Figure 12.7 shows the energy calibrated spectrum of  $^{26}\text{Mg}$ . Since the beam energy or the resulting position at the focal plane might have some fluctuations during the different runs, the spectra are normalized in such way that the position of the highest peak at 10.646 MeV was fitted in each spectrum. Then energy shifts were defined that this strongest transition coincides for each  $^{26}\text{Mg}$  run.

### 12.1.6 Background subtraction

In this section the background subtraction will be described. The remaining instrumental background, that could not have been avoided by the successful beam tuning procedure mainly comes from multiple scattering processes of the protons on the target material. Under the realistic assumption, that background events follow a uniform distribution, they should show up in a flat distribution in the non-dispersive direction of the focal plane. Utilizing this knowledge, the true events are expected to be around  $y_{fp} = 0$  and can then be distinguished from

the background events. Of course, this requires a coordinate-transformation from  $y_{fp}$  in the non-dispersive plane, involving a least-square fit method. The corrected position  $y_c$  can now be described as a function of  $x_{fp}, y_{fp}, \theta_{fp}, \phi_{fp}$  and  $y_{LAS}$ :

$$y_c = y_{fp} + \sum_{i=0}^1 \sum_{j=0}^1 \sum_{k=0}^1 f_{ijk} \cdot x_{fp}^i \theta_{fp}^j \phi_{fp}^k + f_l \cdot y_{LAS}, \quad (12.8)$$

with the fitted coefficients  $f_{ijk}$  and  $f_l$ . Table 12.4 shows a complete list of the parameters used in this experiment.

**Table 12.4.:** Coefficients used in equation (12.8) for the correction of  $y_{fp}$ . The numbers of  $i, j$  and  $k$  represent the exponent of  $x_{fp}, \theta_{fp}$  and  $\phi_{fp}$ , respectively. All angles are given in radian and all distances in mm.

$i j k$	coefficients $f_{ijk}$
000	$2.645 \cdot 10^1$
001	$1.092 \cdot 10^3$
010	$-1.952 \cdot 10^1$
011	$2.088 \cdot 10^3$
100	$6.969 \cdot 10^{-3}$
101	$-7.908 \cdot 10^{-1}$
111	$-5.919$
$l$	coefficient $f_l$
0	$6.197 \cdot 10^{-1} \cdot y_{LAS}$

Figure 12.8 shows a comparison of the corrected  $y_{fp}$  on the right hand side with the uncorrected results on the left hand side. On the right hand side in the lower panel it is shown that the background events are really distributed flat and the true events can be discriminated. In this so-called 'conventional method' a narrow gate is set around  $y_c = 0$ . By applying the same narrow gate on the background events to the left and to the right (see also [Pol11]) and taking the average of the two shifted spectra the true events could be separated by subtracting the average of the background events from the 'true + background' events. This method has shown to not work satisfactorily [Tam07] especially when scattering angle cuts for the solid angle of the spectrometer are applied, since it very much depends on the choice of the background gates. Also an unwanted correlation between  $y_c$  and  $\phi_t$  remains.

In [Tam09] a new background subtraction method is presented, referred to as the 'extenden

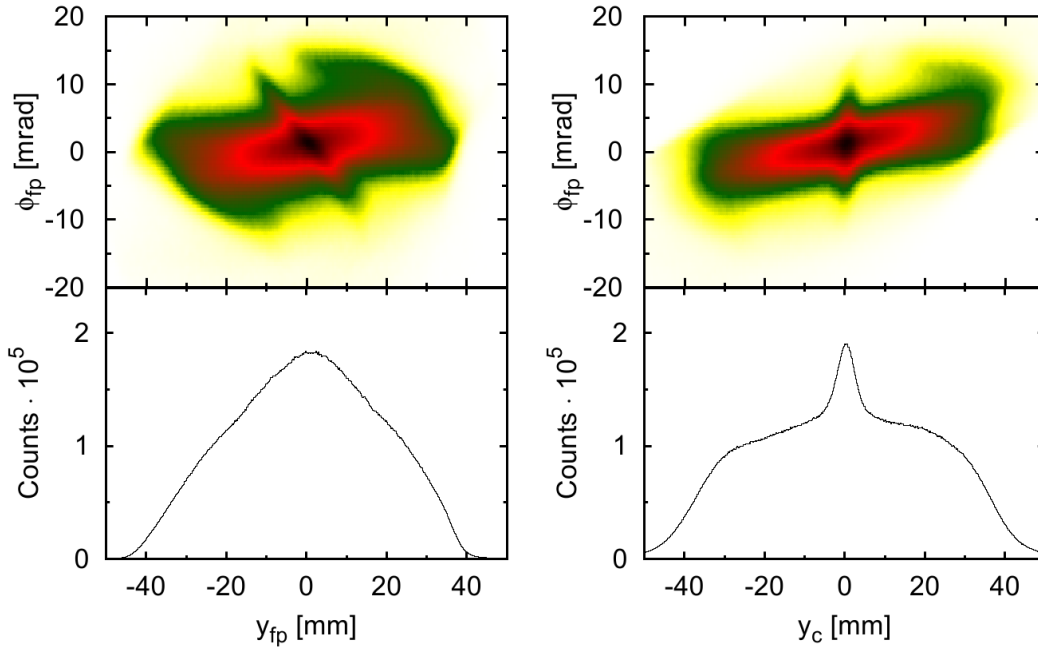


**Figure 12.8.:** Correlation between the vertical scattering angle  $\phi_{fp}$  and the vertical position in the 'conventional method' for the background subtraction. On the left hand side, the untransformed data is shown and on the right hand side the transformation in equation 12.8 has been utilized.

method'. With this method the dependence of  $y_c$  on the scattering angle  $\phi_t$  could be omitted but needs the implementation of a corrected scattering angle  $\phi_c$  which is now independent of  $y_c$ .

The method is based on the assumption that the background events are homogeneously distributed in the  $y_c - \phi_c$  plane (the vertical acceptance of the spectrometer). This requires another correction, which is performed with respect to  $\phi_c$  in a similar way as it has been done to  $y_{fp}$ :

$$\phi_c = \phi_{fp} + \sum_{i=0}^1 e_i \cdot y_{fp}^i, \quad (12.9)$$

The coefficients  $e_i$  are fitted parameters. The corrected vertical acceptance is now shown on the left hand side of figure 12.9. Here, the true events are distributed inside the black rectangle around  $y_c = 0$  and  $\phi_c = 0$ . Analogue to the background subtraction procedure in the 'conventional method' the data is shifted by a constant factor to the left and to the right (see the pictures in the middle and on the right hand side of figure 12.9). Then again, the 'true' dataset is obtained by subtracting the average of the shifted data from the 'true + background' events. In figure 12.10 the resulting excitation energy and background spectrum is presented for  $^{154}\text{Sm}$  at  $0^\circ$  using the full acceptance of the Grand Raiden spectrometer.

Finally the background subtracted spectrum for the full acceptance of the Grand Raiden spectrometer is shown in figure 12.11 for the  $0^\circ$  data set. One clearly observes the two bumps of the

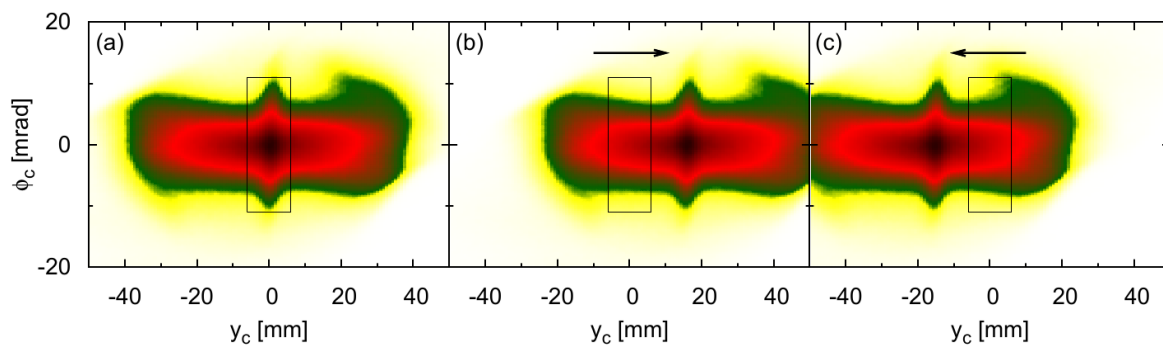


**Figure 12.9.:** Background subtraction with the 'extended method'. The data set on the left hand side (a) was artificially shifted to the right (b) and to the left (c). The background spectra are obtained by applying the gates indicated with the black rectangles.

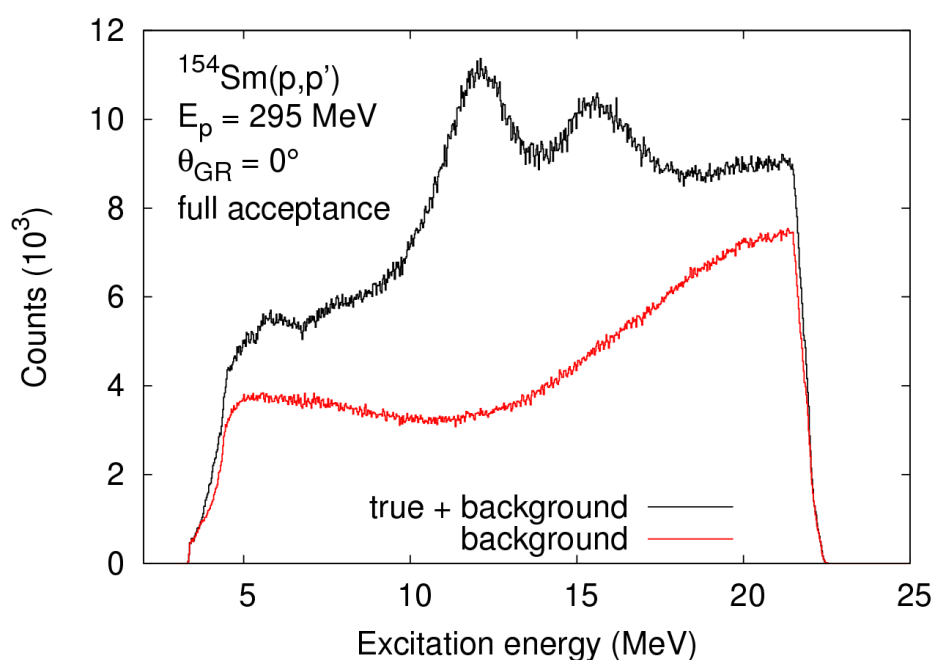


**Figure 12.10.:** Excitation energy spectrum (black) and background spectrum (red) of the  $^{154}\text{Sm}(p,p')$  reaction at  $E_p = 295$  MeV, and  $\theta_{\text{GR}}=0^\circ$ , using the full acceptance of the GR.

GDR at excitation energies of 12.1 MeV and 15.7 MeV. What can also be seen is some structure in the lower excitation energy range between 6 and 9 MeV, that will also be analyzed in the following chapter.

---

### 12.1.7 Double differential cross sections

---

From the inelastic proton scattering spectra, double differential cross sections could have been extracted using the relation:

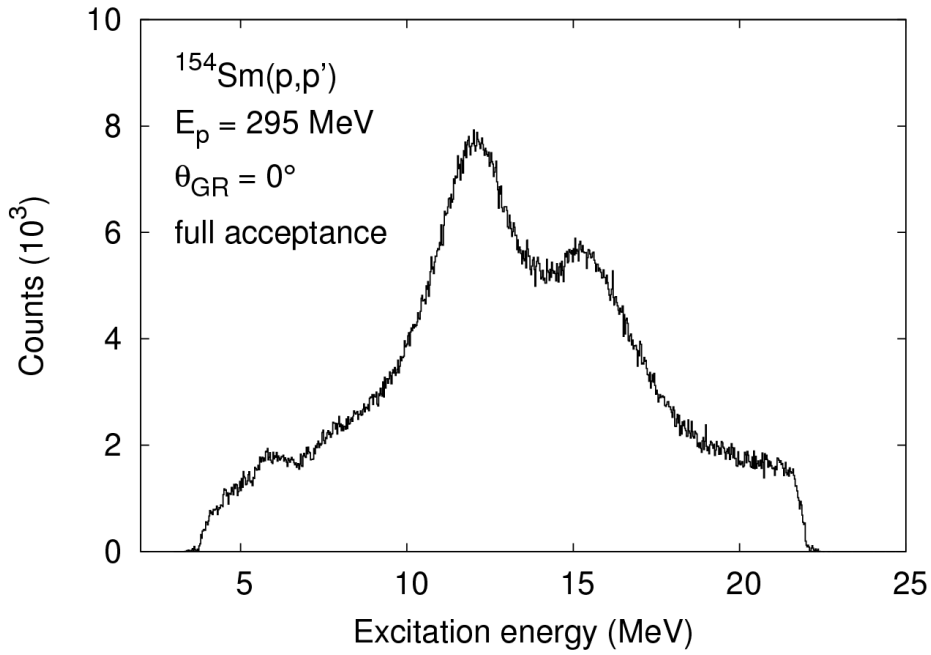


**Figure 12.11.:** Background-subtracted spectrum  $^{154}\text{Sm}(p,p')$  reaction at  $E_p = 295$  MeV, and  $\theta_{\text{GR}}=0^\circ$ , using the full acceptance of the GR.

$$\frac{d^2\sigma}{d\Omega dE} = N_{\text{Counts}} \frac{1}{\Omega_{\text{Lab}}} \frac{1}{L\epsilon} \frac{e}{Qc_{\text{rel}}} \frac{A}{N_A t \eta} J. \quad (12.10)$$

The experimental parameters entering into equation (12.10) are summarized in table 12.5.

**Table 12.5.:** Variables entering into equation (12.10), and their values.

quantity	description	value	unit
$N_{\text{Counts}}$	Number of counts in the specific energy bin		(Counts/MeV)
$\Omega_{\text{Lab}}$	solid angle in the laboratory frame		(sr)
$L$	DAQ live time ratio		
$\epsilon$	detector efficiency		
$e$	elementary charge	$1.602 \cdot 10^{-19}$	(C)
$Q$	collected charge		(C)
$c_{\text{rel}}$	relative charge correction for the FC		
$A$	target atomic weight of the target	154	(g/mol)
$N_A$	Avogadro number	$6.023 \cdot 10^{23}$	(1/mol)
$t$	target thickness	4.0	(mg/cm <sup>2</sup> )
$\eta$	target enrichment	98.69	(%)
$J$	Jacobian transformation from lab to center of mass system		

Applying the software corrections discussed in this chapter, the final energy resolution of the spectra varied between 30 keV and 40 keV. Likewise, spectra of differential cross sections for the  $3^\circ$  setting of the GR spectrometer are determined. Spectra of the differential cross sections at

finite angles of 3° are presented in figure 12.12. Clearly, a continuous drop of the two peaks of the GDR can be observed, indicating a dipole character.

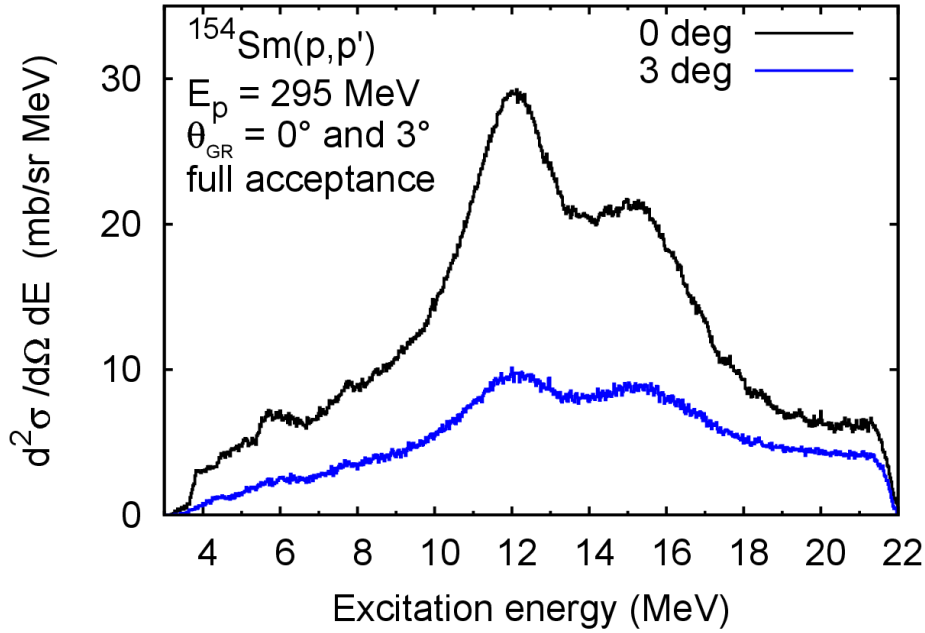


**Figure 12.12.:** Background subtracted spectra for the  $^{154}\text{Sm}(p,p')$  reaction for the  $0^\circ$  and for the  $3^\circ$  setting, respectively.

The statistical and systematic uncertainties are calculated with the equations

$$\Delta \left. \frac{d^2\sigma}{d\Omega dE} \right|_{\text{stat}} = \frac{1}{\sqrt{N_{\text{Counts}}}} \frac{d^2\sigma}{d\Omega dE}, \quad (12.11)$$

$$\Delta \left. \frac{d^2\sigma}{d\Omega dE} \right|_{\text{sys}} = \sqrt{\left(\frac{\Delta\epsilon}{\epsilon}\right)^2 + \left(\frac{\Delta L}{L}\right)^2 + \left(\frac{\Delta t}{t}\right)^2 + \left(\frac{\Delta\Omega}{\Omega}\right)^2 + \left(\frac{\Delta Q}{Q}\right)^2} \frac{d^2\sigma}{d\Omega dE}. \quad (12.12)$$

Major contributions to the systematic inaccuracies originate from the determination of the solid angle (6%) where the uncertainty has been estimated in the sieve-slit calibration procedure. Furthermore, the contribution of the target inhomogeneity ( $\approx 3\%$ ) has been obtained in a weighting analysis [Tam13], while the other experimental quantities can be determined more precisely (i.e. uncertainties lower than 1%). Accordingly, the systematic uncertainties are not exceeding 10%.

---

## 12.2 Polarization transfer analysis

---

---

## 12.2.1 Method for extracting PT observables: The Estimator Method

---

There are at least three methods which are suitable for experiments with a focal plane polarimeter system to extract the PT observables. The sector method which has been used in [Tam99], the Cosine-Fit (also tested method) in [Tam99] and the Estimator method [Bes79]. In this analysis the Estimator method has been used for extracting the PT observables. This method has been chosen, because it is very efficient due to being close to the maximum use of the data. The statistical treatment is well defined and clear and all the sums in the definition of the estimators are additive.

In contrast to previous measurements where two different setups were used to measure with longitudinal polarized beam and sideways polarized beam and combine the results to obtain the quantities  $D_{SS}$  and  $D_{LL}$ , the two separate measurements were performed with the same setup, but again with different beam polarizations. In this work, the polarization transfer coefficients  $D_{NN}$  and  $D_{LL}$  were used to obtain the total spin transfer  $\Sigma$ . The data measured with a normal polarized beam was used to extract a value for the estimator  $\epsilon_n$  and the data measured with a longitudinal polarized beam was used to determine the estimator  $\epsilon_s$ .

At zero degree the relations below are valid:

$$p'_N = p_N D_{NN} \quad (12.13)$$

$$p'_S = p_S D_{SS} \quad (12.14)$$

$$p'_L = p_L D_{LL} \quad (12.15)$$

At finite angles a factor of  $\frac{1}{1+p\langle A_y \rangle}$  has to be included. The polarizations after the second scattering process can be written as the following where the subscripts  $t$  and  $b$  denote the polarizations of the true and the background events respectively

$$p_S^{''t} = p_S D_{SS} \cos \theta_P + p_L D_{LL} \sin \theta_P \quad (12.16)$$

$$p_S^{''b} = p_S \cos \theta_P + p_L \sin \theta_P \quad (12.17)$$

$$p_N^{''t} = p_N^{'t} = p_N D_{NN} \quad (12.18)$$

$$p_N^{''b} = p_N^{'b} = p_N \quad (12.19)$$

For the background events, the assumption holds, that background events have no depolarization and so  $D_{SS} = D_{NN} = 1$  at zero degree measurements.

According to [Bes79] the estimators  $\epsilon_s$  and  $\epsilon_n$  can be obtained from experimental data using

the following equations where again  $t$  and  $b$  stands for true events and background events respectively.

$$\epsilon_s^t = p_s''^t \langle A_y \rangle_s \quad (12.20)$$

$$\epsilon_s^b = p_s''^b \langle A_y \rangle_s \quad (12.21)$$

$$\epsilon_s^{t+b} = \frac{S\epsilon_s^t + N\epsilon_s^b}{S + N} \quad (12.22)$$

$$\epsilon_n^t = p_n''^t \langle A_y \rangle_n \quad (12.23)$$

$$\epsilon_n^b = p_n''^b \langle A_y \rangle_n \quad (12.24)$$

$$\epsilon_n^{t+b} = \frac{S\epsilon_n^t + N\epsilon_n^b}{S + N} \quad (12.25)$$

For these two datasets the signal to noise ratio  $S/N$  is different. The quantities  $p_{s,n}''^b \langle A_y \rangle_{s,n}$  could be extracted in special high statistical background runs.

$$D_{LL}^{mix} \equiv \frac{S + N}{S} \frac{\epsilon_s^{t+b}}{\epsilon_s^b} - \frac{N}{S} = \frac{D_{LL} + c_L(D_{SS} = D_{NN})}{1 + c_L} \quad (12.26)$$

with

$$c_L \equiv \frac{p_S}{p_L} \tan \theta_P^{-1} \quad (12.27)$$

In the latter equation the ratio  $\frac{p_S}{p_L}$  can be extracted from the beam line polarimeter data. The normal polarization transfer coefficient  $D_{NN}$  can now be expressed as

$$D_{NN} = \frac{p_N''^t}{p_N''^b} = \frac{\epsilon_n^t}{\epsilon_n^b} \quad (12.28)$$

Finally one obtains for the polarization transfer observables:

$$D_{NN} = \frac{S + N}{S} \frac{\epsilon_n^{t+b}}{\epsilon_n^b} - \frac{N}{S} \quad (12.29)$$

and

$$D_{LL} = (1 + c_L) D_{LL}^{mix} - c_L D_{NN}. \quad (12.30)$$



---

## 12.3 Results of the polarization transfer analysis

---

The polarization transfer analysis as it has been explained in section 12.2 has been performed and the polarization transfer coefficients  $D_{NN}$  and  $D_{LL}$  could be determined. With the relation 10.57 the total spin transfer  $\Sigma$  can be calculated that allows to decompose the spectrum into a spinflip part and a non-spinflip part.

---

### 12.3.1 Results for $^{26}\text{Mg}$

---

Since  $^{26}\text{Mg}$  has some well known  $1^+$  states which have pure spinflip character and  $^{26}\text{Mg}$  data runs have been performed after each  $^{154}\text{Sm}$  data run, it is well suited for checking the polarization transfer analysis method. The uppermost panel in figure 12.13 shows the spectrum of  $^{26}\text{Mg}$  in the excitation energy range between 6 and 14 MeV with some clear peaks coming from dipole excitations. The corresponding  $D_{NN}$  and  $D_{LL}$  polarisation transfer observables are shown in the panels below. The bottom panel of figure 12.13 displays the total spin transfer  $\Sigma$ . In the observed energy range,  $1^-$  states and  $1^+$  states can be correctly assigned and the results are consistent with older measurements [Tam07].

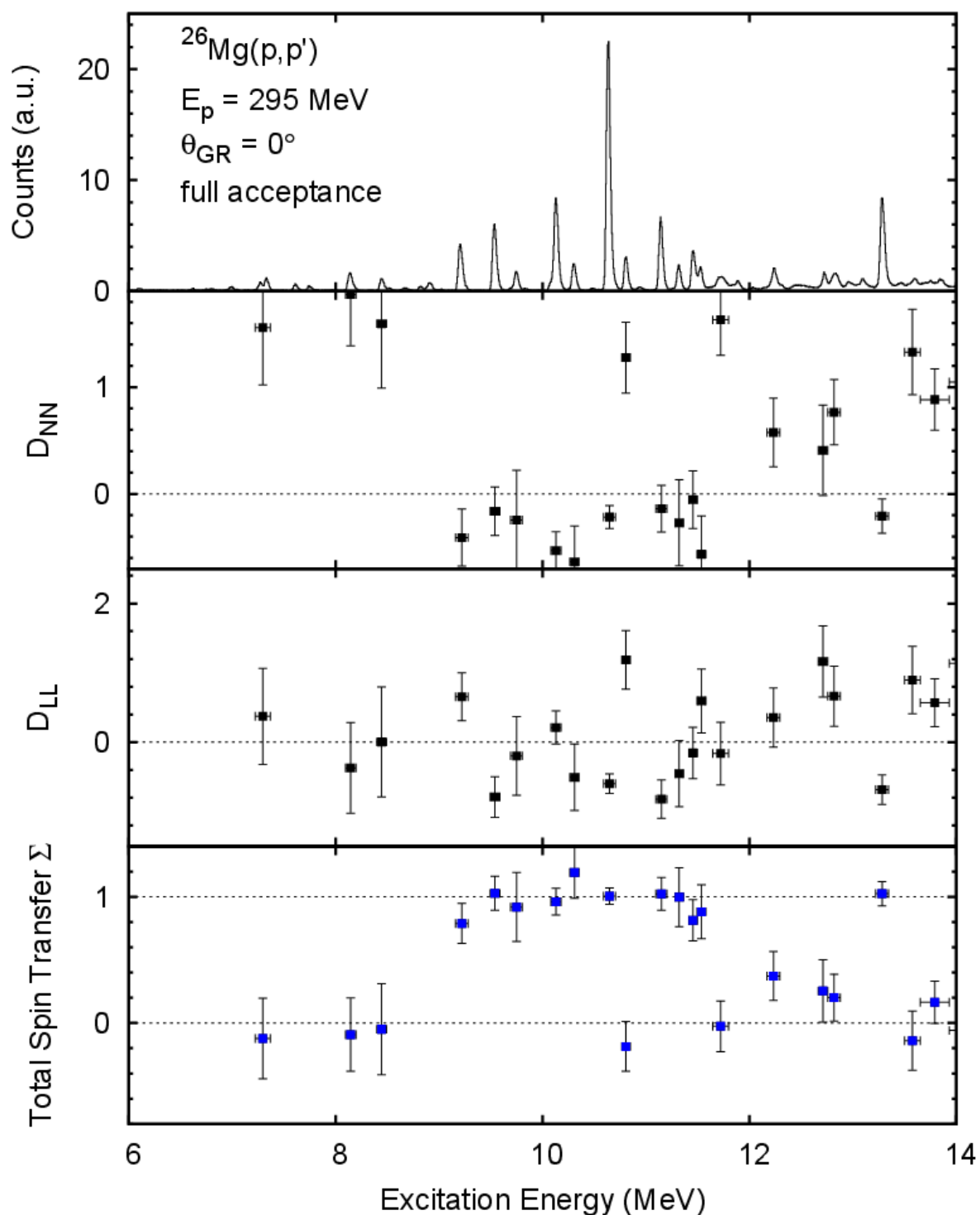


**Figure 12.13.:** Polarization transfer observables for  $^{26}\text{Mg}$

### 12.3.2 Results for $^{154}\text{Sm}$

Since the analysis of the polarization transfer observables worked well for the case of  $^{26}\text{Mg}$ , exactly the same procedure has been applied to the  $^{154}\text{Sm}(\vec{p}, \vec{p}')$  reaction. The results can be seen in figure 12.14. The four subfigures present from top to bottom the double differential

cross section, the extracted polarization transfer observables  $D_{NN}$  and  $D_{LL}$ , and the total spin transfer  $\sigma$  with a bin size of 400 keV throughout the whole excitation energy region. Data in the full acceptance of the Grand Raiden spectrometer (i.e.  $|\theta_t| \leq 1.0^\circ$  and  $|\phi_t| \leq 2.5^\circ$ ) have been used in the present analysis. Due to the non-spinflip nature of the GDR the total spin transfer

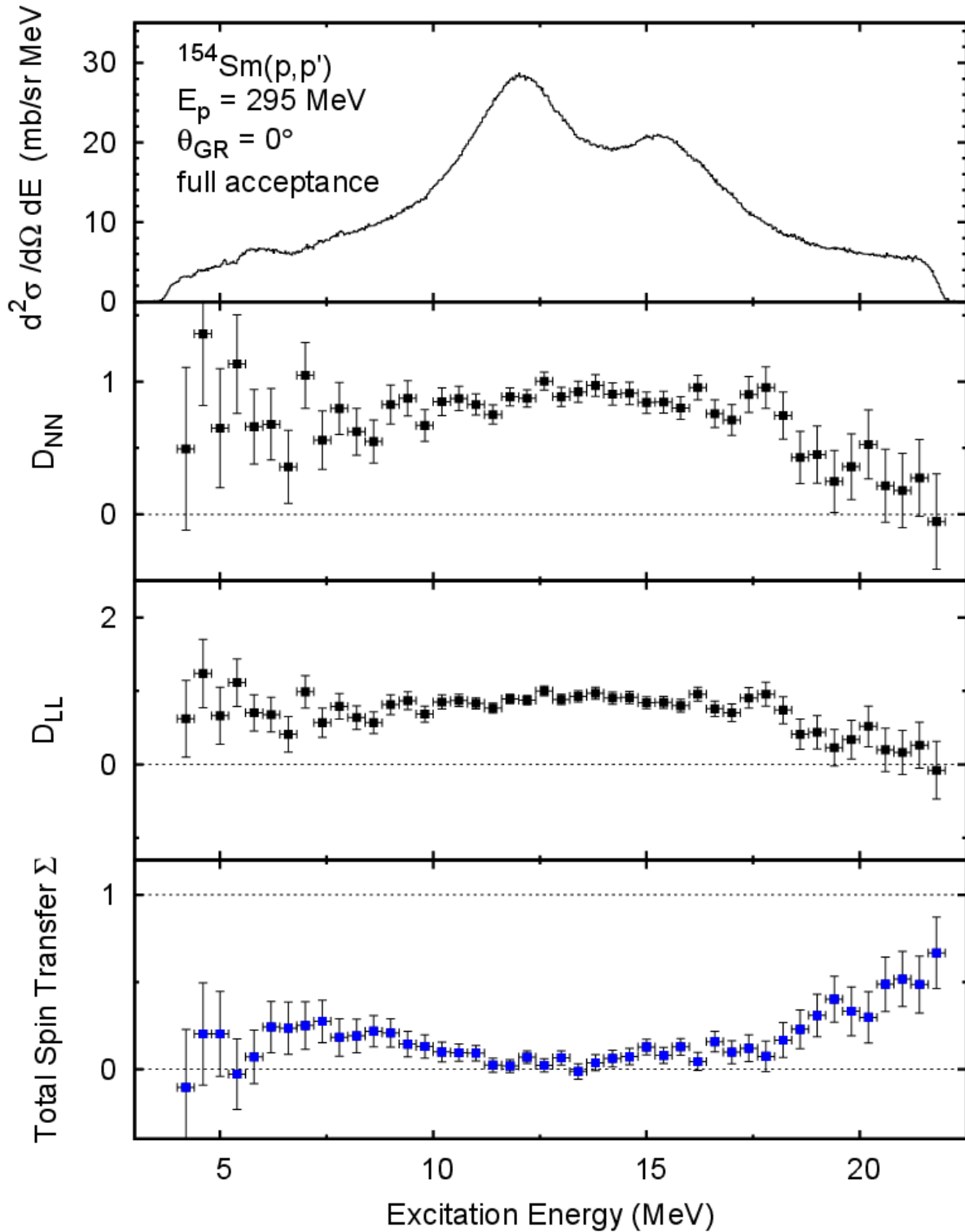
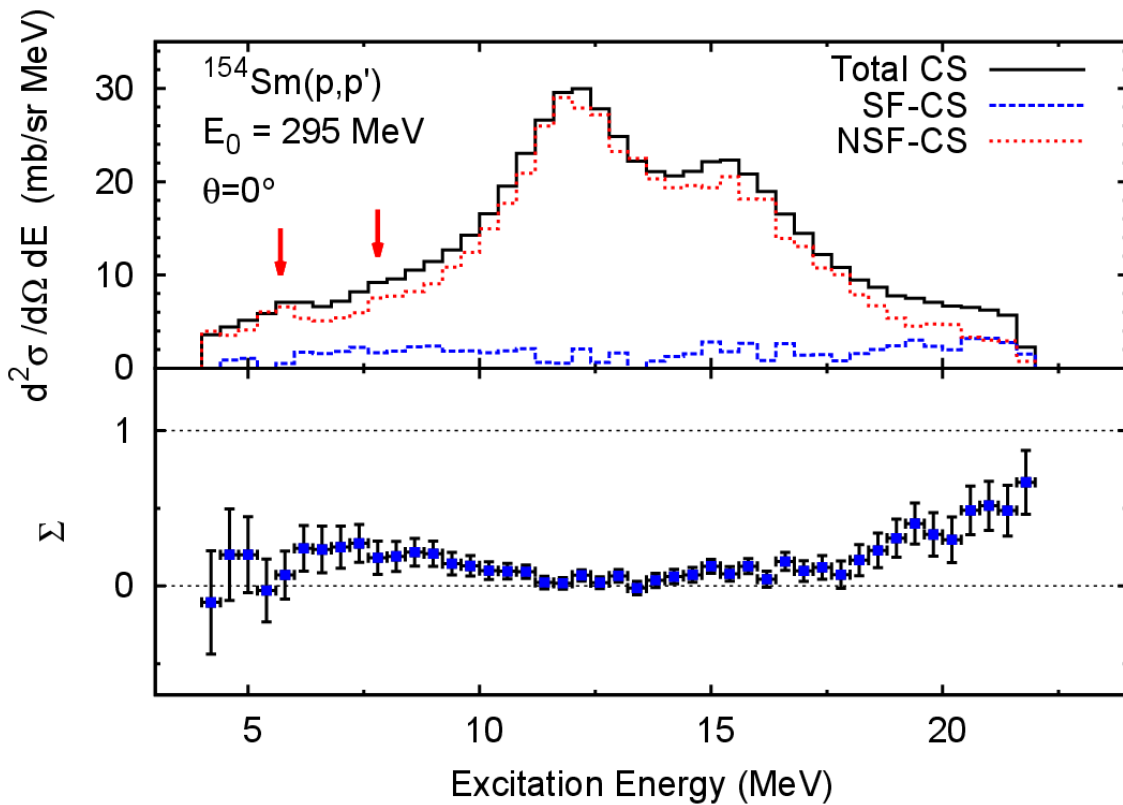


Figure 12.14.: Polarization transfer observables for  $^{154}\text{Sm}$

in this region is consistent with zero. In the low excitation energy region between 4 MeV and 12 MeV, a significant amount of spinflip-M1 response could be detected. At higher excitation energies (i.e. above 17 MeV) the spinflip strength goes up, indicating, that there might be spinflip strength from quasi-free scattering processes [Bak97] and/or spin-dipole strength.

Utilizing equation (10.58) the total cross section can be decomposed in a spinflip cross section and a non-spinflip cross section. The result can be seen in figure 12.15. Here, the total cross section and the spinflip and non-spinflip parts are displayed in the upper panel, while the lower part shows the corresponding total spin transfer  $\Sigma$ . The two red arrows indicate two little bumps in the non-spinflip cross section that will be analyzed in further detail in the following section. The concentration of spinflip cross section between 6 and 12 MeV has been assigned as spinflip-M1 resonance and will be analyzed in section 12.6.



**Figure 12.15.:** Upper panel: The solid line shows the total cross section in bins of 400 keV. The dashed line in blue corresponds to the spinflip cross section and the dashed line in red shows the non-spinflip cross section obtained by using polarization transfer coefficients. Lower panel: The experimentally obtained total spin transfer  $\Sigma$ .

## 12.4 Electric dipole response in $^{154}\text{Sm}$

## 12.4.1 Photoabsorption Cross section

Since the selectivity of the experiment favors  $\lambda = 1$ , radiation with  $\lambda > 1$  only gives minor contributions to the experimental cross section. So the spinflip- $M1$  part of the cross section which has been identified using the method of the polarization transfer observables could be subtracted from the total cross section and the remaining part is of almost pure  $E1$  character. With this assumption the photoabsorption cross section  $\sigma_{abs}$  can be extracted by utilizing equation 10.25 with the help of the equivalent photon method, which has been described in section 10.6.3. In case of  $E1$  excitation, equation 10.25 transforms to

$$\left. \frac{d^2\sigma}{d\Omega dE_\gamma} \right|_{E1}(E_\gamma) = \frac{1}{E_\gamma} \frac{dN_{E1}}{d\Omega}(E_\gamma, \Omega) \sigma_{abs}^{E1}(E_\gamma). \quad (12.31)$$

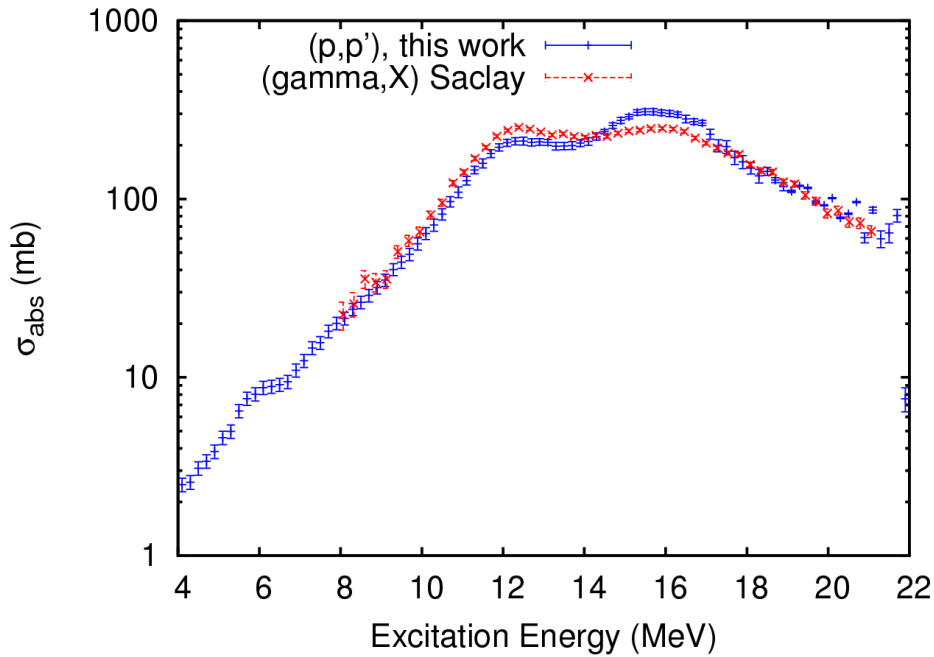


**Figure 12.16.:** Experimentally obtained photoabsorption cross section  $\sigma_{abs}$  in comparison with  $\gamma(x)$  data measured in Saclay [Car74]

Figure 12.16 shows the photoabsorption cross section obtained in the present experiment. As a comparison, the  $\gamma(x)$  data, measured in Saclay [Car74] plotted. Figure 12.17 shows the photoabsorption cross section  $\sigma_{abs}$  deduced from this experiment in the lower excitation energy region. For a better visibility, the GDR fitted GDR-Lorentzians (the  $K=0$  and the  $K=1$  component) have been subtracted in order to obtain this data set. The remaining part is a structure, consisting of two bumps with their centroids at 5.9 MeV and 7.8 MeV, respectively.

This resonance-like structure is assigned as the Pygmy Dipole Resonance (PDR) in the deformed nucleus  $^{154}\text{Sm}$ .

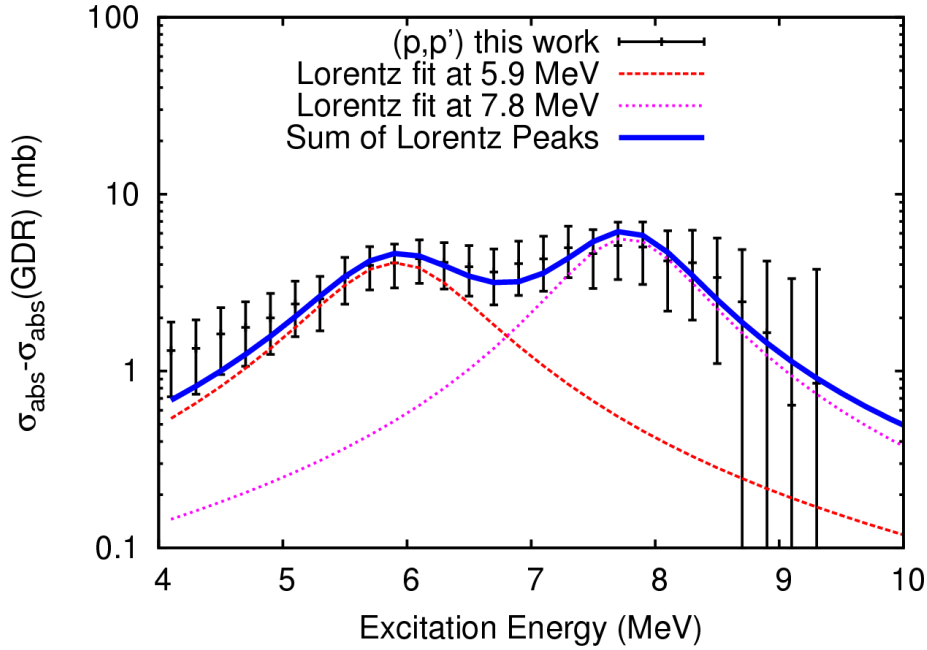


**Figure 12.17.:** Photoabsorption cross section  $\sigma_{abs}$  deduced from this experiment in the lower energy region. For a better visibility, the GDR fitted GDR-Lorentzians (the  $K=0$  and the  $K=1$  component) have been subtracted in order to obtain this data set.

#### 12.4.2 $B(E1)$ strength distribution

Using equations (10.22) and (10.28) from section 10.6, the photoabsorption cross section can be converted into the  $B(E1)$  strength distribution which is depicted in figure 12.18. For the first time, the  $B(E1)$  strength distribution is obtained for the heavy deformed nucleus  $^{154}\text{Sm}$  at energies below the neutron emission threshold  $S_n$ . Obviously some strength which does not belong to the GDR can be found here. The two bumps at 5.9 MeV and 7.8 MeV, that have already been discussed in the previous section are assigned as the PDR. An integration of the  $B(E1)$  strength between 4 and 22 MeV shows that the Thomas-Reiche-Kuhn sum rule is overexhausted by 15%. The integrated PDR strength is about 0.9% of the total  $B(E1)$  strength. In terms of the fraction of the energy-weighted sum rule the PDR shows in combination of the two peaks only 0.5%, because it resides at lower energies.

#### 12.4.3 Deformation splitting

Since the energy ratio of the two bumps in the PDR (equation (12.32), with  $E(1_{low}^-)=5.9$  MeV and  $E(1_{high}^-)=7.8$  MeV) is about the same as in the GDR (equation (12.33), with

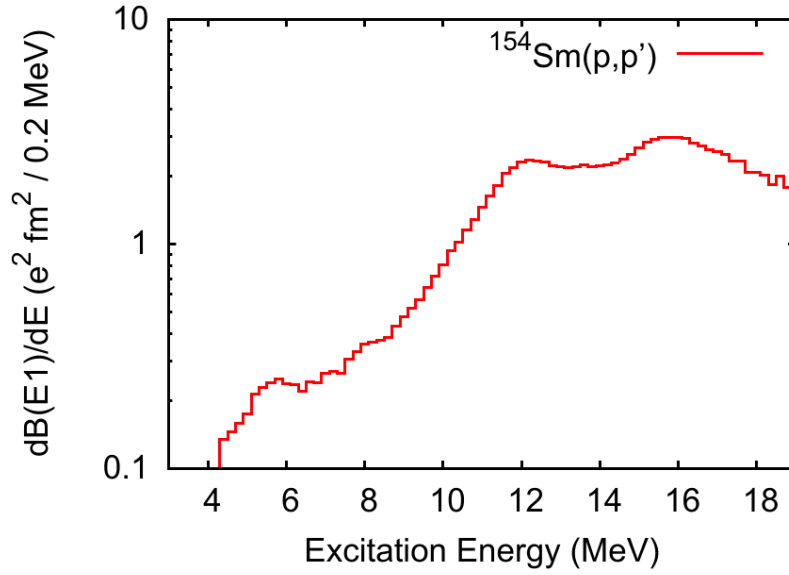


**Figure 12.18.:**  $B(E1)$  strength distribution, obtained in this experiment.

$E(1_{K=0}^-) = 12.1$  MeV and  $E(1_{K=1}^-) = 15.7$  MeV), where a splitting of the resonance structure with respect to their  $K$  quantum number occurs, it is possible that the pygmy resonance might also show a splitting in  $K$ .

$$\text{PDR: } \frac{E(1_{high}^-) - E(1_{low}^-)}{E(1_{high}^-) + E(1_{low}^-)} = \frac{1.9}{13.7} \cong 13.9\% \quad (12.32)$$

$$\text{GDR: } \frac{E(1_{K=1}^-) - E(1_{K=0}^-)}{E(1_{K=1}^-) + E(1_{K=0}^-)} = \frac{3.6}{27.8} \cong 12.9\% \quad (12.33)$$

This would lead to a macroscopic picture of a deformed proton-neutron saturated core, oscillating against a neutron skin, also along two different axes. Figure 12.19 shows a sketch about how the situation might look like. Of course this interpretation is not yet settled and needs to be validated in terms of transition densities. Therefore measurements at finite momentum transfer  $q$  are required.

---

## 12.5 Discussion of angular distributions

---

Besides the  $0^\circ$  setting also a measurement at a finite angle setting of  $\theta_{GR} = 3^\circ$  has been performed. Combining these two measurements, it was possible to define 12 angular cuts at scattering angles between  $0^\circ$  and  $4.1^\circ$ . In figure 12.20 the obtained spectra for the angles  $0.7^\circ$ ,  $1.4^\circ$ ,  $1.6^\circ$ ,  $2.0^\circ$ ,  $2.3^\circ$ ,  $3.1^\circ$  and  $4.1^\circ$  are presented.

Then, absolute differential cross sections could be obtained as a function of the scattering angle  $\theta$ . Figure 12.21 shows the angular distributions for different cuts in the excitation energy spectrum. The first peak of the GDR ( $E_{\text{centroid}} = 12.1$  MeV) significantly drops to larger

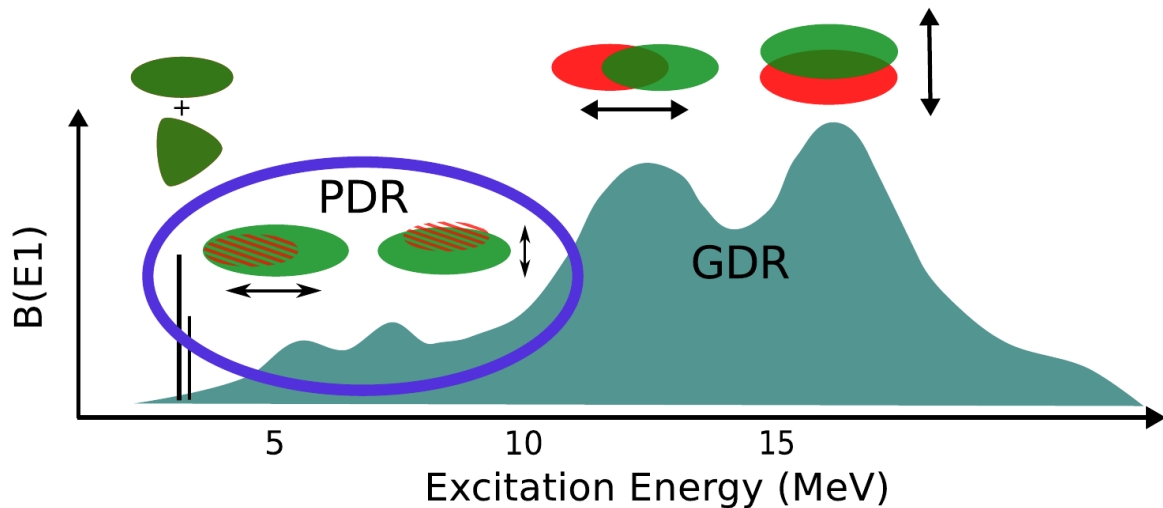


**Figure 12.19.:** Sketch of the  $B(E1)$  response in heavy deformed nuclei. Showing a double hump, with about the same energy ratio as the two peaks of the GDR, the PDR might also show a deformation splitting where a deformed isospin saturated core oscillates against a deformed neutron skin.

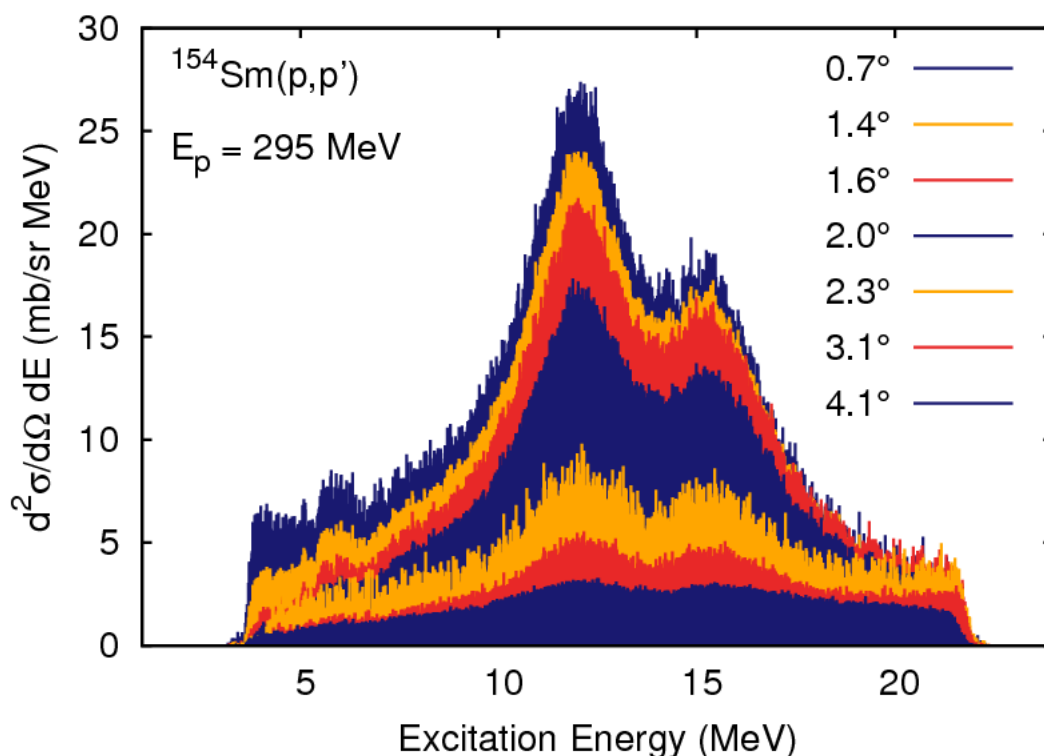


**Figure 12.20.:** Different angle cuts obtained from the finite angle measurements, using the  $0^\circ$  and the  $3^\circ$  setting in combination.

angles, which indicates the pure  $E1$  character. The angular distribution of this peak can be seen in blue in figure 12.21. Here the cross section drops one order of magnitude over the complete angular range. Since nuclear contributions become significant for large scattering



angle  $\theta$ , the second peak of the GDR (15.7 MeV and purple in figure 12.21) is flatter because of that angular distribution which is different to the GDR1 peak. Although the two PDR peaks differ significantly in absolute values from the GDR, their angular dependence shows the same behavior. Therefore one expects not much background for example from other multipoles. The green data set has been extracted at 20 MeV where the GDR has already vanished. As expected, the evolution as a function of the scattering angle is flat. This knowledge can be very useful for a multipole decomposition analysis (MDA). It can be used as an empirical background correction when defining large energy bins.

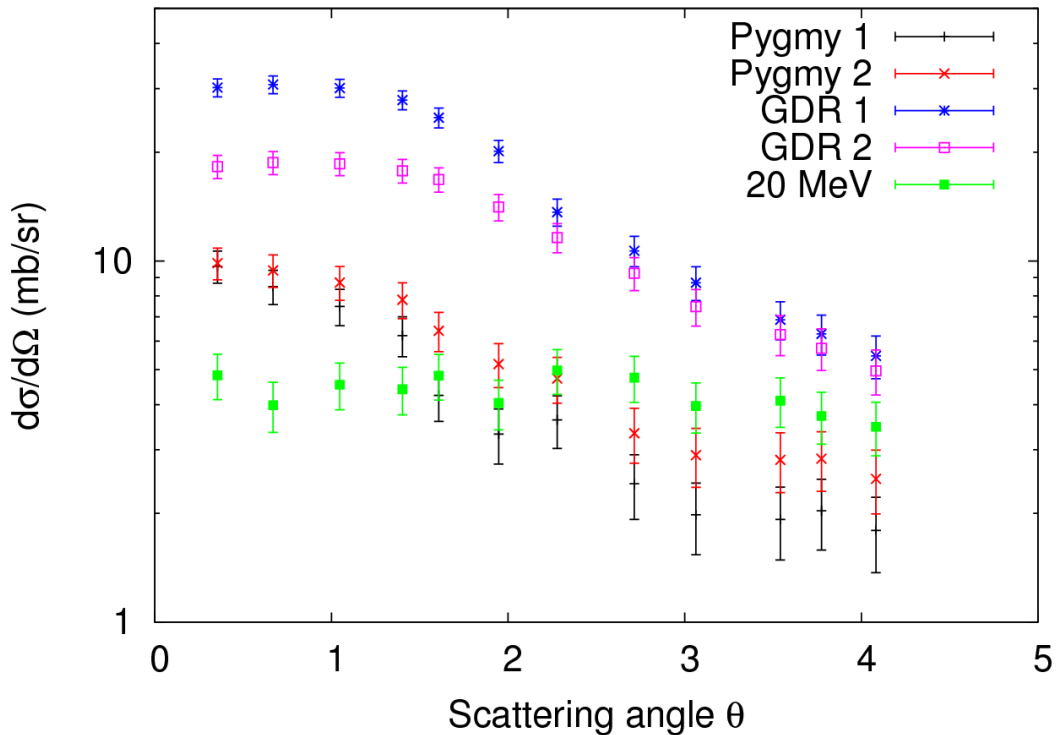


**Figure 12.21.:** Experimental angular distributions at different excitation energies. Energy bins with a width of 200 keV have been used.

## 12.6 Determination of the spinflip-M1 strength distribution with the unit-cross section method

In order to determine the spinflip-M1 transition strength distribution from the spinflip cross section, the ratio of equations 10.38 and 10.39 from section 10.7 has to be taken which results in the following equation:

$$B(M1)_{IV} = \frac{3}{8\pi} (g_s^{IV})^2 \cdot B(M1_{\sigma\tau}) \mu_N^2. \quad (12.34)$$

Utilizing equation 10.40 one obtains

$$B(M1)_{IV} = \frac{3}{8\pi} (g_s^{IV})^2 \cdot \frac{\left(\frac{d\sigma}{d\Omega}\right)_{pp'}^{M1}(0^\circ)}{F_{M1} \hat{\sigma}_{M1}(A)} \mu_N^2. \quad (12.35)$$

The kinematical factor  $F_{M1}$  usually is determined with theoretical angular distributions from a DWBA calculation. Since no big deviations from 1 are expected throughout the observed excitation energy range, it has been approximated with unity. The unit-cross section  $\hat{\sigma}_{M1}(A)$  can be calculated via the unit-cross section of the Gamow-Teller transition  $\hat{\sigma}_{GT^-}(A)$ . This requires the ratio from equations 10.40 and 10.42 and also equations 10.39 and 10.41 have to be taken into account. The Clebsch-Gordan coefficients  $C_{M1,10}^2 = \frac{T_0}{T_0+1}$  and  $C_{GT^-}^2 = \frac{2T_0-1}{2T_0+1}$  are taken from reference [Fuj11]. With  $T_0 = 15$  for  $^{154}\text{Sm}$  and the ratio

$$\frac{\left(\frac{d\sigma}{d\Omega}\right)_{pp'}^{GT} F_{M1}}{\left(\frac{d\sigma}{d\Omega}\right)_{pp'}^{M1} F_{M1}} = 2 \quad (12.36)$$

the unit-cross section  $\hat{\sigma}_{M1}(A)$  can be calculated:

$$\hat{\sigma}_{M1}(A) = \frac{1}{2} \frac{T_0 + 1}{T_0} \hat{\sigma}_{GT^-}(A). \quad (12.37)$$

In reference [Sas09] it is discussed that  $\hat{\sigma}_{GT^-}(A)$  for 300 MeV proton scattering can be obtained from the phenomenological description

$$\hat{\sigma}_{GT^-}(A) = N_{90} e^{-x(A^{-1/3} - 90^{-1/3})} \quad (12.38)$$

with  $N_{90} = (3.4 \pm 0.2)$  mb/sr and  $x = 0.40 \pm 0.05$ . Finally the spinflip-M1 strength distribution can be determined and it is shown in the upper part of figure 12.22. As a reference, the spinflip-M1 distribution from [Wör94] is shown which indicates a double hump structure. The lower bump at roughly 6 MeV is seen in the present (p,p') experiment but less strength is observed, concluding that parts of the cross section from [Wör94] was originally of E1 nature. A fairly good agreement can be seen between between 7 and 9 MeV and even more strength has been seen in the present experiment at higher energy but with large uncertainties.

The lower part of figure 12.22 shows the running sum of spinflip-M1 strength between 4 MeV and 12 MeV. The total strength is  $13.2 \pm 2.7 \mu_N^2$  which is in a good agreement to the work of Wörtche [Wör94] ( $10.5 \pm 2.0 \mu_N^2$ ).

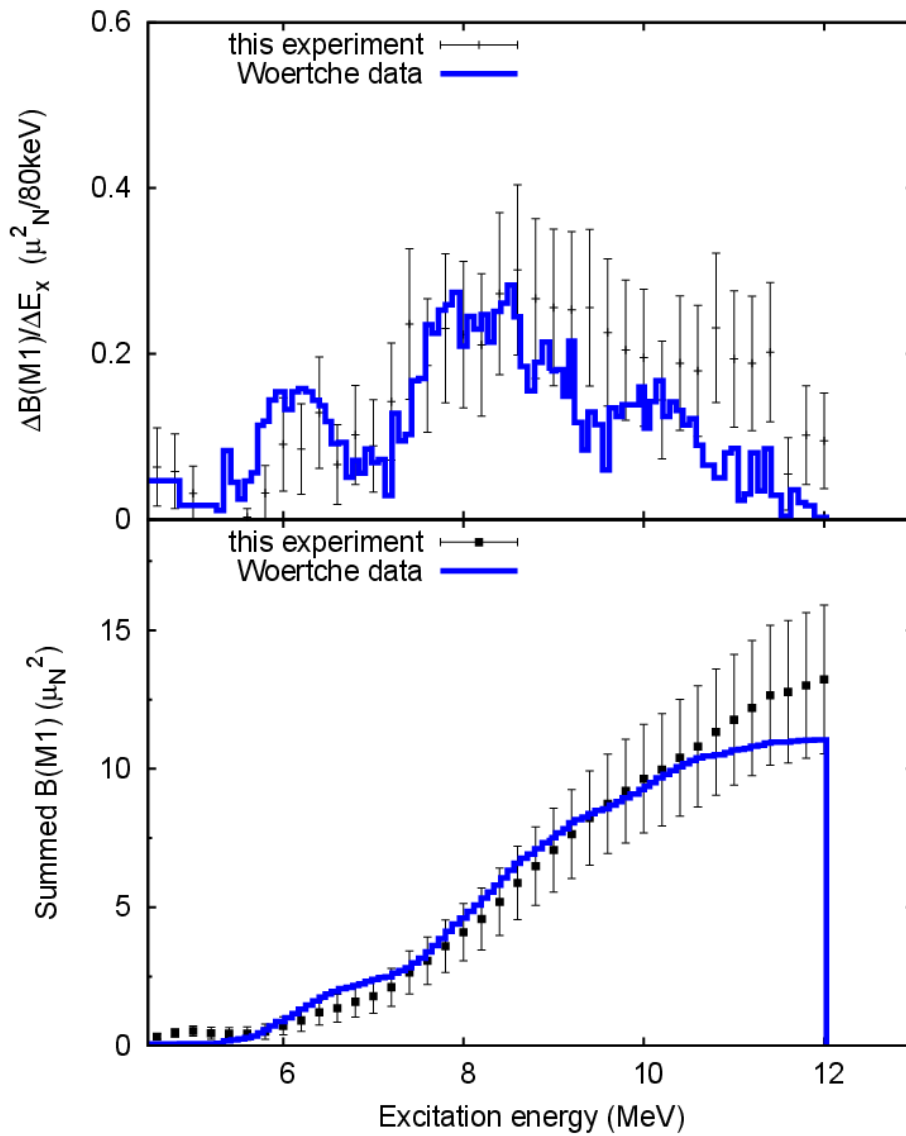


**Figure 12.22.:** Spinflip-M1 strength distribution obtained with the unit-cross section method. The upper graph shows the spinflip-M1 strength distribution in comparison to the data obtained in [Wör94]. In the lower panel, the running sum for both experiments is shown.



---

## 13 Conclusion and Outlook

---

To summarize, in part II of this PhD thesis, the data analysis of a high resolution polarized proton scattering experiment on the heavy deformed nucleus  $^{154}\text{Sm}$  has been presented. The experiment has been performed at the RCNP in Osaka, Japan, using a 295 MeV beam of polarized protons, scattering off a self-supporting metallic  $^{154}\text{Sm}$  foil. With the advanced dispersion matching techniques, excellent beam conditions were achieved, resulting in a very high energy resolution of  $\Delta E = 30 - 40$  keV. Utilizing the polarization transfer analysis, the experimental cross section could be separated into spinflip and non-spinflip parts. Also measurements at finite scattering angles have been performed at  $\theta_{GR} = 0^\circ$  and  $\theta_{GR} = 3^\circ$  which made it possible to extract angular distributions for different modes of excitation. In the case of electric dipole response, the photoabsorption cross section was calculated and compared to former  $(\gamma, n)$  measurements, showing a good agreement. Also the B(E1) strength distribution has been investigated, where for the first time in  $^{154}\text{Sm}$  the pygmy dipole resonance was observed. It appeared in a double hump structure with peaks in the excitation energy of 5.9 MeV and 7.8 MeV have been observed. A possible explanation in terms of a deformation splitting of the PDR was given. Also the spinflip-M1 strength distribution has been determined with the help of the unit-cross section method. A broad distribution between 5 and 12 MeV has been seen, resulting in a total spinflip-M1 sum strength of  $13.1 \pm 2.7 \mu_N^2$ .

As an outlook in the future the following aspects should be worth investigating:

- The PDR has now been seen in the spherical nucleus  $^{144}\text{Sm}$  and the prolate deformed  $^{154}\text{Sm}$ . It would be interesting to examine the role of the deformation for the PDR in the whole isotopic chain.
- A multipole decomposition analysis (MDA) as it has been already performed in [Pol11, Mar13] as an independent tool for the  $E1$  and  $M1$  separation of the cross section would be ideal to compare to the results from the polarization transfer analysis. Therefore theoretical angular distributions are calculated in the framework of the quasi-particle phonon Model (QPM) [Sol92]. It is a phenomenological microscopic nuclear model where couplings to complex degrees of freedom are considered. With the help of this theoretical model, various collective excitations in heavy nuclei have been successfully described. Nice examples for the low-lying quadrupole strength in vibrational nuclei can be seen in [Wal11] and for the case of the pygmy resonance in  $^{208}\text{Pb}$  the article [Pol12] can be recommended. Since  $^{154}\text{Sm}$  is a heavy deformed nucleus, some difficulties in the theoretical description occur. The problems start already on the mean field level. In a spherical symmetric Woods Saxon potential all single-particle energies of a given orbit are degenerate, which results in analytical solutions of the wave functions. In the case of deformation,

---

this degeneracy is usually broken. The number of energy levels increases dramatically and a lot of particle-hole transitions are possible. Also the configuration space is much bigger than in the spherical case. The QPM framework needs further development to account for the complexity of the deformation. An extension of the QPM to real deformed calculations would be preferable and comparison to this experiment in terms of a multipole decomposition analysis is foreseen for the near future.

- Up to now, only dipole contribution to the total cross section have been taken into consideration (e.g. Pygmy-E1, GDR-E1, spinflip-M1). Recent  $(\alpha, \alpha')$  studies [Tam14] show a non vanishing percentage of E0 and E2 parts coming from the giant monopole resonance (GMR) and the giant quadrupole resonance (GQR), respectively. It would be useful to estimate the percentage of the E0 and E2 strength that is still hiding in the double differential cross section.
- As a future perspective for investigating the nature of the double hump structure of the PDR in heavy deformed nuclei the CAGRA [CAG14] collaboration is planning  $(p, p'\gamma)$  measurements at finite  $q$ . A new beam line has been constructed at the RCNP facility where Grand Raiden angles from  $4^\circ$  to  $20^\circ$  can be addressed with much higher beam intensities than before.

---

## A Derivation of $\rho^2(E0)$ transition strength as a function of potential stiffness

---

Starting with the definition of the E0 operator

$$\rho_{if}^2 \cdot e^2 R^4 = \left( \frac{3}{4\pi} \cdot eR^2 \right)^2 \left| \left\langle f \left| \sum_{\mu} \alpha_{2\mu}^* \alpha_{2\mu} \right| i \right\rangle \right|^2 \quad (\text{A.1})$$

while the quadrupole operator follows the relation

$$\hat{Q}_{2\mu} = \frac{3}{4\pi} eZR^2 \alpha_{2\mu}, \quad (\text{A.2})$$

the B(E2) transition strength can be expressed as

$$B(E2; i \rightarrow f) = \frac{1}{2I_i + 1} \left| \left\langle f \left\| Q_2 \right\| i \right\rangle \right|^2 \quad (\text{A.3})$$

The collective Hamiltonian in a more general notation is:

$$H_{coll} = -\frac{\hbar^2}{2B_2} \sum_{\mu} (-1)^{\mu} \frac{\partial^2}{\partial \alpha_{2\mu} \partial \alpha_{2\mu}} + V(\alpha_2). \quad (\text{A.4})$$

Following the commutator rules, this equation can be rewritten as

$$\left[ H_{coll}, \sum_{\mu} \alpha_{2\mu}^* \alpha_{2\mu} \right] = -\frac{\hbar^2}{B_2} \sum_{\mu} \left( \frac{\partial}{\partial \alpha_{2\mu}} \cdot \alpha_{2\mu} + \alpha_{2\mu} \cdot \frac{\partial}{\partial \alpha_{2\mu}} \right) \quad (\text{A.5})$$

Commutator rules expand the previous equation to the double commutator equation

$$\left[ \left[ H_{coll}, \sum_{\mu} \alpha_{2\mu}^* \alpha_{2\mu} \right], \sum_{\nu} \alpha_{2\nu}^* \alpha_{2\nu} \right] = -4 \frac{\hbar^2}{B_2} \sum_{\mu} \alpha_{2\mu}^* \alpha_{2\mu}. \quad (\text{A.6})$$

Plugging in the ground state in the Schrödinger equation, one obtains:

$$\left\langle 0_1^+ \left| \left[ \left[ H_{coll}, \sum_{\mu} \alpha_{2\mu}^* \alpha_{2\mu} \right], \sum_{\nu} \alpha_{2\nu}^* \alpha_{2\nu} \right] \right| 0_1^+ \right\rangle \quad (\text{A.7})$$


---

$$\begin{aligned}
&= -2 \sum_{i=2,\dots} (E(0_i^+) - E(0_1^+)) \left| \left\langle 0_1^+ \left| \sum_{\mu} \alpha_{2\mu}^* \alpha_{2\mu} \right| 0_i^+ \right\rangle \right|^2 \\
&= -2 \sum_{i=2,\dots} (E(0_i^+) - E(0_1^+)) \cdot \rho^2(0_i^+ \rightarrow 0_1^+) e^2 R^4 \cdot \left( \frac{3}{4\pi} Z e R^2 \right)^{-2}
\end{aligned}$$

Further calculation lead to

$$\begin{aligned}
&\left\langle 0_1^+ \left| \sum_{\mu} \alpha_{2\mu}^* \alpha_{2\mu} \right| 0_1^+ \right\rangle = \left( \frac{3}{4\pi} Z e R^2 \right)^{-2} \left\langle 0_1^+ \left| \sum_{\mu} Q_{2\mu}^{\dagger} Q_{2\mu} \right| 0_1^+ \right\rangle \quad (\text{A.8}) \\
&= \left( \frac{3}{4\pi} Z e R^2 \right)^{-2} \sum_{i=1,\dots} \sum_{\mu} \left\langle 0_1^+ \left| Q_{2\mu}^{\dagger} \right| 2_i^{+,\mu} \right\rangle \left\langle 2_i^{+,\mu} \left| Q_{2\mu} \right| 0_1^+ \right\rangle \\
&= \left( \frac{3}{4\pi} Z e R^2 \right)^{-2} \sum_i \left| \left\langle 0_1^+ \left\| \left\| Q_2 \right\| \right\| 2_i^+ \right\rangle \right|^2 \\
&= \left( \frac{3}{4\pi} Z e R^2 \right)^{-2} \sum_i B(E2; 0_1^+ \rightarrow 2_i^+)
\end{aligned}$$

Averaging equation A.6 over the ground state and substituting equation A.7 and equation A.8 one obtains:

$$\begin{aligned}
&\sum_{i=2,3,\dots} (E(0_i^+) - E(0_1^+)) \rho^2(0_i^+ \rightarrow 0_1^+) e^2 R^4 \quad (\text{A.9}) \\
&= 2 \frac{\hbar^2}{B_2} \sum_{i=1,2,\dots} B(E2; 0_1^+ \rightarrow 2_i^+)
\end{aligned}$$

The main contribution to the sum on the left hand side in equation A.10 gives the  $0_2^+$  state. The main contribution to the sum on the right hand side gives the  $2_1^+$  state.

In this approximation:

$$(E(0_2^+) - E(0_1^+)) \cdot \rho^2(0_2^+ \rightarrow 0_1^+) e^2 R^4 = 2 \frac{\hbar^2}{B_2} B(E2; 0_1^+ \rightarrow 2_1^+). \quad (\text{A.10})$$

In the case of the well deformed axially symmetric nuclei:

$$E(0_2^+) - E(0_1^+) = \hbar \sqrt{\frac{C_0}{B_2}} \quad (\text{A.11})$$

where  $C_0$  is a stiffness coefficient for  $\beta$ -oscillations.

$$B(E2; 0_1^+ \rightarrow 2_1^+) = \left( \frac{3}{4\pi} Z e R^2 \right)^2 \beta_0^2 \quad (\text{A.12})$$



where  $\beta_0$  is the ground state deformation. Substituting equation A.11 and A.12 into A.10 we obtain:

$$\hbar \sqrt{\frac{C_2}{B_2}} \rho^2 (E0; 0_2^+ \rightarrow 0_1^+) e^2 R^4 = 2 \frac{\hbar^2}{B_2} \left( \frac{3}{4\pi} Z e R^2 \right)^2 \beta_0^2 \quad (\text{A.13})$$

or

$$\rho^2 (E0; 0_2^+ \rightarrow 0_1^+) e^2 R^4 = 2 \frac{\hbar}{\sqrt{B_2 C_0}} \left( \frac{3}{4\pi} Z e R^2 \right)^2 \beta_0^2. \quad (\text{A.14})$$

However, for deformed nuclei

$$\begin{aligned} \frac{1}{2} \frac{\hbar}{\sqrt{B_2 C_0}} \left( \frac{3}{4\pi} Z e R^2 \right)^2 &= B (E2; 0_2^+ \rightarrow 2_1^+) \\ &= B (E2; 0_1^+ \rightarrow 2_\beta^+) \end{aligned} \quad (\text{A.15})$$

where  $2_\beta^+$  is the rotational state built on top of the  $0_2^+$  state. Substituting A.15 into A.14 we obtain a relation of Rasmussen [Ras60]:

$$\rho^2 (E0; 0_2^+ \rightarrow 0_1^+) e^2 R^4 = 4B (E2; 0_2^+ \rightarrow 2_1^+) \cdot \beta_0^2. \quad (\text{A.16})$$

Thus, the relation A.10 is more general than the relation A.16. The last relation is of course only applicable in the case of well deformed nuclei.

To eliminate  $B_2$  from equation A.10 we can use the relation

$$(E(2_1^+) - E(0_1^+)) B (E2; 0_1^+ \rightarrow 2_1^+) = \frac{\hbar^2}{B_2} \left( \frac{3}{4\pi} Z e R^2 \right)^2 \quad (\text{A.17})$$

which can be derived in a similar way. Substituting equation A.17 into equation A.10 we obtain finally a relation:

$$\rho^2 (E0; 0_2^+ \rightarrow 0_1^+) = 2 \left( \frac{E(2_1^+) - E(0_1^+)}{E(0_2^+) - E(0_1^+)} \right) \frac{(B(E2; 0_1^+ \rightarrow 2_1^+))^2}{\left( \frac{3Z}{4\pi} \right)^2 (e^2 R^4)^2}. \quad (\text{A.18})$$

This is an expression of the  $\rho^2(E0)$  transition strength only depending on experimental nuclear structure observables. Using the relation between  $B(E2; 0_1^+ \rightarrow 2_1^+)$  and  $\langle 0_1^+ | \beta^2 | 0_1^+ \rangle$ :

$$B(E2; 0_1^+ \rightarrow 2_1^+) = \left( \frac{3Z}{4\pi} eR^2 \right)^2 \langle 0_1^+ | \beta^2 | 0_1^+ \rangle \quad (\text{A.19})$$

one obtains from equation A.18:

$$\rho^2(E0; 0_2^+ \rightarrow 0_1^+) = 2 \left( \frac{E(2_1^+) - E(0_1^+)}{E(0_2^+) - E(0_1^+)} \right) \left( \frac{3Z}{4\pi} \right)^2 \langle 0_1^+ | \beta^2 | 0_1^+ \rangle^2. \quad (\text{A.20})$$

The most important observation from equation A.20 is that when the stiffness of the potential in  $\beta$  increases, the ratio  $\left( \frac{E(2_1^+) - E(0_1^+)}{E(0_2^+) - E(0_1^+)} \right)$  decreases. As a result  $\rho^2(E0; 0_2^+ \rightarrow 0_1^+)$  should also decrease.

---

## B List of $\rho^2(E0)$ transition strengths compared in figure 6.5

---

In figure 6.5 various experimental  $\rho^2(E0)$  have been compared. The values are taken from [Kib05]. In table B.1 they are listed with the corresponding  $r_\beta$  and  $R_{4/2}$  values. Since the  $\beta$  band is not necessarily built on top of the  $0_2^+$  state, the transition type is also given.

**Table B.1.:** List of  $\rho^2(E0)$  values compared in figure 6.5.

Nucleus	$\rho^2(E0)$	$r_\beta$	$R_{4/2}$	transition type
$^{150}\text{Nd}$	$38 \pm 25$	0.09	2.90	$0_1^+ \rightarrow 0_2^+$
$^{152}\text{Sm}$	$51 \pm 5$	0.14	3.01	$0_2^+ \rightarrow 0_1^+$
$^{154}\text{Gd}$	$89 \pm 17$	0.2	3.01	$0_2^+ \rightarrow 0_1^+$
$^{156}\text{Gd}$	$42 \pm 20$	0.33	3.24	$0_2^+ \rightarrow 0_1^+$
$^{158}\text{Gd}$	$35 \pm 12$	0.41	3.29	$0_3^+ \rightarrow 0_1^+$
$^{166}\text{Er}$	$2.2 \pm 0.8$	0.39	3.29	$0_2^+ \rightarrow 0_1^+$
$^{170}\text{Yb}$	$24 \pm 5$	0.42	3.29	$0_3^+ \rightarrow 0_1^+$



---

## Bibliography

---

- [Amo00] Adv. Nucl. Phys. **25** (2000) 275.
- [And01] W. Andrejtscheff, C. Kohstall, P. von Brentano, C. Fransen, U. Kneissl, N. Pietralla, and H. Pitz, Phys. Lett. B **506** (2001) 239.
- [Are00] H. Arenhövel, F. Ritz, and T. Wilbois, Phys. Rev. C **61** (2000) 034002.
- [Bag76] C. Baglin, Nuclear Data Sheets **18** (1976) 223 .
- [Bäh] C. Bähr, *Computercode phashi*, unpublished.
- [Bak97] F. T. Baker, L. Bimbot, C. Djalali, C. Glashauser, H. Lenske, W. G. Love, M. Morlet, E. Tomasi-Gustafsson, J. V. de Wiele, J. Wambach, and A. Willis, Phys. Rep. **289** (1997) 235.
- [Bal47] G. C. Baldwin and G. S. Klaiber, Phys. Rev. **71** (1947) 3.
- [Bas12] S. Bassauer, *Weiterentwicklung der Online-Datenanalyse sowie der Ladungs- und Stromauslese am LINTOTT-Spektrometer*, Bachelor thesis, TU Darmstadt (2012).
- [Bel70] D. A. Bell, C. E. Avelado, M. G. Davidson, and J. P. Davidson, Can. J. Phys **48** (1970) 2542.
- [Ber75] B. L. Berman and S. C. Fultz, Rev. Mod. Phys. **47** (1975) 713.
- [Ber85] C. A. Bertulani and G. Baur, Nucl. Phys. A **442** (1985) 739.
- [Ber88] C. A. Bertulani and G. Baur, Phys. Rep. **163** (1988) 299.
- [Ber93] C. Bertulani and A. Nathan, Nuclear Physics A **554** (1993) 158 .
- [Bes79] D. Besset, B. Favier, L. Greeniaus, R. Hess, C. Lechanoine, D. Rapin, and D. Werren, Nuclear Instruments and Methods **166** (1979) 515 .
- [Boh52] A. Bohr, Mat. Fys. Medd. K. Dan. Vidensk. Selsk. **26** (1952).
- [Boh75] A. Bohr and B. Mottelson, *Nuclear Structure*, Benjamin, Reading (1975).
- [Bon06] D. Bonatsos, D. Lenis, N. Pietralla, and P. A. Terziev, Phys. Rev. C **74** (2006) 044306.
- [Bon09] J. Bonnet, A. Krugmann, J. Beller, N. Pietralla, and R. V. Jolos, Phys. Rev. C **79** (2009) 034307.
- [Bra] N. Braun, *Line shape fitting program*, unpublished.

- 
- [Bre04] P. von Brentano, V. Werner, R. F. Casten, C. Scholl, E. A. McCutchan, R. Krücken, and J. Jolie, *Phys. Rev. Lett.* **93** (2004) 152502.
- [bri] *Online conversion coefficient calculator*, <http://bricc.anu.edu.au/>, accessed: 27.05.2014.
- [Bur02a] O. Burda, *Design of a shielding for the new focal plane detector system of the energy-loss spectrometer at the S-DALINAC*, Diploma thesis, Karazin Kharkiv National University, Ukraine (2002).
- [Bür02b] T. Bürvenich, D. G. Madland, J. A. Maruhn, and P.-G. Reinhard, *Phys. Rev. C* **65** (2002) 044308.
- [Bur08] O. Burda, *Nature of Mixed-Symmetry  $2^+$  States in  $^{94}\text{Mo}$  from High-Resolution Electron and Proton Scattering and Line Shape of the First Excited  $1/2^+$  State in  $^9\text{Be}$* , Ph.D. thesis, TU Darmstadt, Darmstadt (2008).
- [CAG14] *Website of the cagra collaboration*, <http://www.phy.anl.gov/gammasphere/CAGRA/> (2014), accessed: 13.06.2014.
- [Car74] P. Carlos, H. Beil, R. Bergère, A. Leprêtre, A. D. Miniac, and A. Veyssière, *Nuclear Physics A* **225** (1974) 171 .
- [Cas00] R. Casten, *Nuclear structure from a simple perspective*, volume 23, Oxford University Press (2000).
- [Cas01] R. F. Casten and N. V. Zamfir, *Phys. Rev. Lett.* **87** (2001) 052503.
- [CER] *PAW++ program package (CERN libraries)*,  
<http://cern.ch/paw/>,  
<http://cern.ch/cernlib/>.
- [Che10] M. Chernykh, H. Feldmeier, T. Neff, P. von Neumann-Cosel, and A. Richter, *Phys. Rev. Lett.* **105** (2010) 022501.
- [Cla03] R. M. Clark, M. Cromaz, M. A. Deleplanque, M. Descovich, R. M. Diamond, P. Fallon, R. B. Firestone, I. Y. Lee, A. O. Macchiavelli, H. Mahmud, E. Rodriguez-Vieitez, F. S. Stephens, and D. Ward, *Phys. Rev. C* **68** (2003) 037301.
- [Cla04] R. M. Clark, M. Cromaz, M. A. Deleplanque, M. Descovich, R. M. Diamond, P. Fallon, I. Y. Lee, A. O. Macchiavelli, H. Mahmud, E. Rodriguez-Vieitez, F. S. Stephens, and D. Ward, *Phys. Rev. C* **69** (2004) 064322.
- [Cos92] C. D. Coster, K. Heyde, and A. Richter, *Nuclear Physics A* **542** (1992) 375 .

- 
- [Die95] H. Diesener, Doctoral thesis D17, TU Darmstadt (1995).
- [Die01] H. Diesener, U. Helm, P. von Neumann-Cosel, A. Richter, G. Schrieder, A. Stascheck, A. Stiller, and J. Carter, *Nuclear Physics A* **696** (2001) 272 .
- [Don66] W. Donner and W. Greiner, *Zeitschrift für Physik* **197** (1966) 440, ISSN 0044-3328.
- [Dre] C. Dreher, *Computercode drepha*, unpublished.
- [Dre74] B. Dreher, J. Friedrich, K. Merle, H. Rothhaas, and G. Lührs, *Nuclear Physics A* **235** (1974) 219 .
- [Dus05] K. Dusling and N. Pietralla, *Phys. Rev. C* **72** (2005) 011303.
- [Dus06] K. Dusling, N. Pietralla, G. Rainovski, T. Ahn, B. Bochev, A. Costin, T. Koike, T. C. Li, A. Linnemann, S. Pontillo, and C. Vaman, *Phys. Rev. C* **73** (2006) 014317.
- [End11] J. Enders, T. Bahlo, P. Bangert, R. Barday, M. Brunken, C. Eckardt, R. Eichhorn, M. Espig, M. Freudenberger, A. Göök, C. Ingengaag, J. Lindemann, P. von Neumann-Cosel, A. Oberstedt, S. Oberstedt, Y. Poltoratska, A. Richter, M. Roth, F. Schneider, M. Wagner, A. Weber, and B. Zwicker, *Journal of Physics: Conference Series* **295** (2011) 012152.
- [ENS13] *Evaluated nuclear structure data file*, <http://www.nndc.bnl.gov/ensdf> (2013), accessed: 01.02.2013.
- [Epe13] E. Epelbaum, arXiv:1302.3241 [nucl-th] (2013).
- [Foh78] J. Foh, R. Frey, R. Scheneider, D. Schüll, A. Schwierczinski, H. Theissen, and O. Titze, *Nuclear Instruments and Methods* **153** (1978) 43 .
- [Fra85] M. A. Franey and W. G. Love, *Phys. Rev. C* **31** (1985) 488.
- [Fre89] D. Frekers, D. Bohle, A. Richter, R. Abegg, R. Azuma, A. Celler, C. Chan, T. Drake, K. Jackson, J. King, C. Miller, R. Schubank, J. Watson, and S. Yen, *Physics Letters B* **218** (1989) 439 .
- [Fre90] D. Frekers, H. Wörtche, A. Richter, R. Abegg, R. Azuma, A. Celler, C. Chan, T. Drake, R. Helmer, K. Jackson, J. King, C. Miller, R. Schubank, M. Vetterli, and S. Yen, *Physics Letters B* **244** (1990) 178 .
- [Fri11] Y. Fritzsche, *Aufbau und Inbetriebnahme einer Quelle polarisierter Elektronen am supraleitenden Darmstädter Elektronenlinearbeschleuniger S-DALINAC*, Ph.D. thesis, TU Darmstadt, Ilmenau (2011).
- [Fuj99] M. Fujiwara, H. Akimune, I. Daito, H. Fujimura, Y. Fujita, K. Hatanaka, H. Ikegami, I. Katayama, K. Nagayama, N. Matsuoka, S. Morinobu, T. Noro, M. Yoshimura, H. Sakaguchi, Y. Sakemi, A. Tamii, and M. Yosoi, *Nucl. Inst. Meth. A* **422** (1999) 484.

- 
- [Fuj08] N. Fujita, H. Sakaguchi, Y. Maeda, A. Nonaka, H. Okamura, A. Tamii, J. Zenihiro, H. Matsubara, D. Ishikawa, T. Terashima, and Y. Yasuda, *RCNP annual report* (2008).
- [Fuj11] Y. Fujita, B. Rubio, and W. Gelletly, *Progress in Particle and Nuclear Physics* **66** (2011) 549 .
- [Gal03] M. Galassi, J. Davies, J. Theiler, B. Gough, B. Jungman, M. Booth, and F. Rossi, *GNU Scientific Library Reference Manual*, 2nd ed., Network Theory Ltd., Bristol (2003).
- [Gia14] F. Giacoppo, F. Bello Garrote, T. Eriksen, A. Gorgen, M. Guttormsen *et al.* (2014).
- [GNU] Gnuplot, version 4.4 patchlevel 0 (2010),  
<http://www.gnuplot.info/>.
- [Gor98] S. Goriely, *Phys. Lett. B* **436** (1998) 10.
- [Grä78] H.-D. Gräf, H. Miska, E. Spamer, O. Titze, and T. Walcher, *Nuclear Instruments and Methods* **153** (1978) 9 .
- [Har01] M. N. Harakeh and A. van der Woude, *Giant Resonances*, Oxford studies in nuclear physics (2001).
- [Hat97] K. Hatanaka, K. Takahisa, H. Tamura, M. Sato, and I. Miura, *Nuclear Instruments and Methods in Physics Research Section A: Accelerators, Spectrometers, Detectors and Associated Equipment* **384** (1997) 575 .
- [Hel92] M. Hellström, B. Fogelberg, H. Mach, D. Jerrestam, and L. Spanier, *Phys. Rev. C* **46** (1992) 860.
- [Hey83] K. Heyde, P. V. Isacker, M. Waroquier, J. Wood, and R. Meyer, *Physics Reports* **102** (1983) 291 .
- [Hey10] K. Heyde, P. von Neumann-Cosel, and A. Richter, *Rev. Mod. Phys.* **82** (2010) 2365.
- [Hil98] R. Hilton, W. Höhenberger, and P. Ring, *The European Physical Journal A - Hadrons and Nuclei* **1** (1998) 257.
- [Hof02] F. Hofmann, P. von Neumann-Cosel, F. Neumeyer, C. Rangacharyulu, B. Reitz, A. Richter, G. Schrieder, D. I. Sober, L. W. Fagg, and B. A. Brown, *Phys. Rev. C* **65** (2002) 024311.
- [Iac00] F. Iachello, *Phys. Rev. Lett.* **85** (2000) 3580.
- [Iac01] F. Iachello, *Phys. Rev. Lett.* **87** (2001) 052502.
- [Iac03] F. Iachello, *Phys. Rev. Lett.* **91** (2003) 132502.



- 
- [IKP14] *Ikp main website*, <http://www.ikp.tu-darmstadt.de/dasinstitut/index.de.jsp> (2014), accessed: 18.05.2014.
- [Jola] R. Jolos, private communication.
- [Jolb] R. Jolos, private communication.
- [Jol09] R. V. Jolos and P. von Brentano, *Phys. Rev. C* **79** (2009) 044310.
- [Kaw02] T. Kawabata, *Polarization transfer in the  $^{16}\text{O}(p,p')$  reaction at forward angles and structure of the spin-dipole resonance*, Ph.D. thesis, Kyoto University, Japan (2002).
- [Ker59] A. K. Kerman, H. McManus, and R. M. Thaler, *Annu. Phys.* **8** (1959) 551.
- [Kib05] T. Kibédi and R. Spear, *Atomic Data and Nuclear Data Tables* **89** (2005) 77 .
- [KIN] Computer program KINMAT, iThemba Laboratory for Accelerator Based Sciences, Faure, South Africa, unpublished.
- [Kru] A. M. Krumbholz, Doctoral thesis D17, TU Darmstadt, in preparation.
- [Kru08] A. Krugmann, *Untersuchung von E0-Übergängen in Kernen am Phasenübergang zwischen sphärischer und deformierter Kerngestalt*, Master thesis, TU Darmstadt (2008).
- [Kru11] A. Krugmann, Z. P. Li, J. Meng, N. Pietralla, and D. Vretenar, *Journal of Physics G: Nuclear and Particle Physics* **38** (2011) 065102.
- [Lar11] A. C. Larsen, M. Guttormsen, M. Krtička, E. Běták, A. Bürger, A. Gørgen, H. T. Nyhus, J. Rekstad, A. Schiller, S. Siem, H. K. Toft, G. M. Tveten, A. V. Voinov, and K. Wikan, *Phys. Rev. C* **83** (2011) 034315.
- [Len05] A. W. Lenhardt, *Entwicklung eines Si-Mikrostreifendetektors für das  $169^\circ$ -Spektrometer am S-DALINAC*, Ph.D. thesis, TU Darmstadt, Aachen (2005).
- [Len06] A. Lenhardt, U. Bonnes, O. Burda, P. von Neumann-Cosel, M. Platz, A. Richter, and S. Watzlawik, *Nuclear Instruments and Methods in Physics Research Section A: Accelerators, Spectrometers, Detectors and Associated Equipment* **562** (2006) 320 .
- [Li09] Z. P. Li, T. Nikšić, D. Vretenar, J. Meng, G. A. Lalazissis, and P. Ring, *Phys. Rev. C* **79** (2009) 054301.
- [Lip50] B. A. Lippmann and J. Schwinger, *Phys. Rev.* **79** (1950) 469.
- [Lov81] W. G. Love and M. A. Franey, *Phys. Rev. C* **24** (1981) 1073.
- [Mar11] D. Martin, *Investigation of the reaction  $^{144}\text{Sm}(p,p')$  under extreme forward angles*, Bachelor thesis, TU Darmstadt (2011).

- 
- [Mar13] D. Martin, *Gamma Strength Function of  $^{96}\text{Mo}$ : A Test of the Axel-Brink Hypothesis*, Master thesis, TU Darmstadt (2013).
- [Mat91] N. Matsuoka, K. Hatanaka, S. Morinobu, T. Noro, A. Okihana, and K. Sagara, *RCNP annual report* (1991).
- [Mat10] H. Matsubara, *Isoscalar and isovector spin-M1 transitions from the even-even,  $N = Z$  nuclei across the sd-shell region*, Ph.D. thesis, Osaka University (2010).
- [Mat14] M. Mathy, *M1 Stärke in  $^{48}\text{Ca}$  aus inelastischer Protonenstreuung*, Bachelor thesis, TU Darmstadt (2014).
- [McC05] E. A. McCutchan, N. V. Zamfir, and R. F. Casten, *Phys. Rev. C* **71** (2005) 034309.
- [Mo69] L. W. Mo and Y. S. Tsai, *Rev. Mod. Phys.* **41** (1969) 205.
- [Mos82] J. M. Moss, *Phys. Rev. C* **26** (1982) 727.
- [NC97] P. von Neumann-Cosel, C. Rangacharyulu, A. Richter, G. Schrieder, A. Stascheck, and S. Strauch, *Phys. Rev. Lett.* **78** (1997) 2924.
- [NC99] P. von Neumann-Cosel, F. Neumeyer, S. Nishizaki, V. Y. Ponomarev, C. Rangacharyulu, B. Reitz, A. Richter, G. Schrieder, D. I. Sober, T. Waindzoeh, and J. Wambach, *Phys. Rev. Lett.* **82** (1999) 1105.
- [NC02] P. von Neumann-Cosel, A. Richter, G. Schrieder, A. Shevchenko, A. Stiller, and H. Arenhövel, *Phys. Rev. Lett.* **88** (2002) 202304.
- [Neu97a] F. Neumeyer, Doctoral thesis D17, TU Darmstadt (1997).
- [Neu97b] F. Neumeyer, *Untersuchungen magnetischer Kernanregungen in  $^{48}\text{Ca}$  und  $^{90}\text{Zr}$  mit hochauflösender Elektronenstreuung unter  $180^\circ$  am S-DALINAC*, Ph.D. thesis, TU Darmstadt, Darmstadt (1997).
- [Nik09] T. Nikšić, Z. P. Li, D. Vretenar, L. Próchniak, J. Meng, and P. Ring, *Phys. Rev. C* **79** (2009) 034303.
- [Nor90] T. Noro, Y. Mizuno, H. Togawa, S. Hirata, N. Matsuoka, O. Kamigaito, F. Hiei, Y. Sakemi, H. Akimune, and T. Takahashi, *RCNP annual report* (1990).
- [Ohl02] G. G. Ohlsen, *Rep. Prog. Phys.* **35** (2002) 717.
- [Pie04] N. Pietralla and O. M. Gorbachenko, *Phys. Rev. C* **70** (2004) 011304.
- [Pie10] J. Piekarewicz, *J. Phys. G: Nucl. Part. Phys.* **37** (2010) 064038.

- 
- [Pol11] I. Poltoratska, *Complete electric dipole response in  $^{208}\text{Pb}$  from high-resolution polarized proton scattering at  $0^\circ$* , Doctoral thesis D17, TU Darmstadt (2011).
- [Pol12] I. Poltoratska, P. von Neumann-Cosel, A. Tamii, T. Adachi, C. A. Bertulani, J. Carter, M. Dozono, H. Fujita, K. Fujita, Y. Fujita, K. Hatanaka, M. Itoh, T. Kawabata, Y. Kalmykov, A. M. Krumbholz, E. Litvinova, H. Matsubara, K. Nakanishi, R. Neveling, H. Okamura, H. J. Ong, B. Özel-Tashenov, V. Yu. Ponomarev, A. Richter, B. Rubio, H. Sakaguchi, Y. Sakemi, Y. Sasamoto, Y. Shimbara, Y. Shimizu, F. D. Smit, T. Suzuki, Y. Tameshige, J. Wambach, M. Yosoi, and J. Zenihiro, *Phys. Rev. C* **85** (2012) 041304(R).
- [Pon] V. Yu. Ponomarev, *Computer code for the extraction of electron scattering form factors from transition densities*, unpublished.
- [Ras60] J. O. Rasmussen, *Nuclear Physics* **19** (1960) 85 .
- [Ray07] J. Raynal, Computing code DWBA07, NEA Data Service NEA1209/08 (2007).
- [RCN14] *Rcnp main website*, <https://www.rcnp.osaka-u.ac.jp> (2014), accessed: 18.05.2014.
- [Rei02] B. Reitz, A. M. V. Berg, D. Frekers, F. Hofmann, M. de Huu, Y. Kalmykov, H. Lenske, P. von Neumann-Cosel, V. Y. Ponomarev, S. Rakers, A. Richter, G. Schrieder, K. Schweda, J. Wambach, and H. J. Wörtche, *Physics Letters B* **532** (2002) 179.
- [Rei10] P.-G. Reinhard and W. Nazarewicz, *Phys. Rev. C* **81** (2010) 051303(R).
- [Ric96] A. Richter, EPAC 96: European Particle Accelerator Conference <5, 1996, Sitges, Barcelona>: [Proceedings]. Vol. 1. Hrsg.: S. Myers (u.a.) - Bristol, Philadelphia: Inst. of Physics Publ., 1996. S. 110-114, Inst. of Physics Publ, Bristol, Philadelphia, ersch. ebenf. als: Technische Universität Darmstadt, Institut für Kernphysik: IKDA; 96/17.
- [Rin80] P. Ring and P. Schuck, *The Nuclear many-body problem*, Springer, New York (1980).
- [Rye06] N. Ryezayeva, *Search for the  $p_{1/2}$ - Resonance in  $^7\text{He}$  with the  $^7\text{Li}(d,^2\text{He})$  Reaction and Measurement of the Deuteron Electrodisintegration under 180-deg at the S-DALINAC*, Ph.D. thesis, TU Darmstadt (2006).
- [Sak97] H. Sakai, T. Wakasa, H. Okamura, T. Nonaka, T. Ohnishi, K. Yako, K. Sekiguchi, S. Fujita, Y. Satou, H. Otsu, T. Uesaka, S. Ishida, N. Sakamoto, M. B. Greenfield, and K. Hatanaka, *Proceedings of the International Symposium on New Facet of Spin Giant Resonances in Nuclei*, Tokyo, Japan, 1997, edited by H. Sakai, H. Okamura, T. Wakasa (World Scientific, Singapore 1998) (1997) 29.

- 
- [San91a] R. Sandor, *Shape transition in the Nd-isotopes: an electron scattering study.*, Doctoral thesis, Vrije Universiteit te Amsterdam (1991).
- [San91b] R. K. J. Sandor, H. P. Blok, U. Garg, M. Girod, M. N. Harakeh, C. W. de Jager, and H. de Vries, *Phys. Rev. C* **43** (1991) R2040.
- [Sar96] P. Sarriguren, E. Moya de Guerra, and R. Nojarov, *Phys. Rev. C* **54** (1996) 690.
- [Sas09] M. Sasano, H. Sakai, K. Yako, T. Wakasa, S. Asaji, K. Fujita, Y. Fujita, M. B. Greenfield, Y. Hagihara, K. Hatanaka, T. Kawabata, H. Kuboki, Y. Maeda, H. Okamura, T. Saito, Y. Sakemi, K. Sekiguchi, Y. Shimizu, Y. Takahashi, Y. Tameshige, and A. Tamii, *Phys. Rev. C* **79** (2009) 024602.
- [Sat83] G. Satchler, *Direct nuclear reactions*, Oxford University Press, New York (1983).
- [Sav10] D. Savran, K. Lindenberg, J. Glorius *et al.*, *Nuclear Instruments and Methods in Physics Research Section A: Accelerators, Spectrometers, Detectors and Associated Equipment* **613** (2010) 232 .
- [Sav13] D. Savran, T. Aumann, and A. Zilges, *Prog. Part. Nucl. Phys.* **70** (2013) 210.
- [Sch78] D. Schüll, J. Foh, H.-D. Gräf, H. Miska, R. Schneider, E. Spamer, H. Theissen, O. Titze, and T. Walcher, *Nuclear Instruments and Methods* **153** (1978) 29 .
- [Sch00] A. Schiller, L. Bergholt, M. Guttormsen, E. Melby, J. Rekstad, and S. Siem, *Nuclear Instruments and Methods in Physics Research Section A: Accelerators, Spectrometers, Detectors and Associated Equipment* **447** (2000) 498 , ISSN 0168-9002.
- [Shi09] N. Shirikova, R. Jolos, N. Pietralla, A. Sushkov, and V. Voronov, *The European Physical Journal A* **41** (2009) 393.
- [Sma14] J. Smallcombe, P. Davies, C. Barton, D. Jenkins, L. Andersson, P. Butler, D. Cox, R.-D. Herzberg, A. Mistry, E. Parr, T. Grahn, P. Greenlees, K. Hauschild, A. Herzan, U. Jakobsson, P. Jones, R. Julin, S. Juutinen, S. Ketelhut, M. Leino, A. Lopez-Martens, P. Nieminen, J. Pakarinen, P. Papadakis, P. Peura, P. Rahkila, S. Rinta-Antila, P. Ruotsalainen, M. Sandzelius, J. Saren, C. Scholey, J. Sorri, and J. Uusitalo, *Physics Letters B* **732** (2014) 161 .
- [Sol92] V. G. Soloviev, *Theory of Atomic Nuclei: Quasiparticles and Phonons*, Inst. of Phys. Publ., Bristol (1992).
- [Son11] K. Sonnabend, D. Savran, J. Beller, M. Büssing, A. Constantinescu, M. Elvers, J. Endres, M. Fritzsche, J. Glorius, J. Hasper, J. Isaak, B. Löher, S. Müller, N. Pietralla, C. Romig, A. Sauerwein, L. Schnorrenberger, C. Wälzlein, A. Zilges, and M. Zweidinger, *Nuclear*

- [Spe81] J. Speth and A. van der Woude, Reports on Progress in Physics **44** (1981) 719.
- [Str00] S. Strauch, P. von Neumann-Cosel, C. Rangacharyulu, A. Richter, G. Schrieder, K. Schweda, and J. Wambach, Phys. Rev. Lett. **85** (2000) 2913.
- [Suz00] T. Suzuki, Prog. Theor. Phys. **321** (2000) 859.
- [Tak02] H. Takeda, *Modification of nucleon-nucleon interactions in nuclear medium and neutron densities extracted via proton elastic scattering at intermediate energies*, Ph.D. thesis, Kyoto University (2002).
- [Tam99] A. Tamii, *Polarization transfer observables from proton inelastic scattering from  $^{12}\text{C}$  at zero degrees*, Ph.D. thesis, Kyoto University (1999).
- [Tam07] A. Tamii, T. Adachi, J. Carter, M. Dozono, H. Fujita, Y. Fujita, K. Hatanaka, H. Hashimoto, T. Kaneda, M. Itoh, T. Kawabata, H. Matsubara, K. Nakanishi, P. von Neumann-Cosel, H. Okamura, A. Perez, I. Poltoratska, V. Yu. Ponomarev, L. Popescu, A. Richter, B. Rubio, H. Sakaguchi, Y. Sakemi, Y. Sasamoto, Y. Shimbara, Y. Shimizu, F. D. Smit, Y. Tameshige, M. Yosoi, J. Zenihiro, and K. Zimmer, Nucl. Inst. Meth. A **788** (2007) 53.
- [Tam09] A. Tamii, Y. Fujita, H. Matsubara, T. Adachi, J. Carter, M. Dozono, H. Fujita, K. Fujita, H. Hashimoto, K. Hatanaka, T. Itahashi, M. Itoh, T. Kawabata, K. Nakanishi, S. Ni-nomiya, A. Perez-Cerdan, L. Popescu, B. Rubio, T. Saito, H. Sakaguchi, Y. Sakemi, Y. Sasamoto, Y. Shimbara, Y. Shimizu, F. Smit, Y. Tameshige, M. Yosoi, and J. Zenihiro, Nucl. Inst. Meth. A **605** (2009) 326.
- [Tam11] A. Tamii, I. Poltoratska, P. von Neumann-Cosel, Y. Fujita, T. Adachi, C. A. Bertulani, J. Carter, M. Dozono, H. Fujita, K. Fujita, K. Hatanaka, D. Ishikawa, M. Itoh, T. Kawabata, Y. Kalmykov, A. M. Krumbholz, E. Litvinova, H. Matsubara, K. Nakanishi, R. Neveling, H. Okamura, H. J. Ong, B. Özel-Tashenov, V. Yu. Ponomarev, A. Richter, B. Rubio, H. Sakaguchi, Y. Sakemi, Y. Sasamoto, Y. Shimbara, Y. Shimizu, F. D. Smit, T. Suzuki, Y. Tameshige, J. Wambach, R. Yamada, M. Yosoi, and J. Zenihiro, Phys. Rev. Lett. **107** (2011) 062502.
- [Tam13] A. Tamii, *priv. communication* (2013).
- [Tam14] A. Tamii, *priv. communication* (2014).
- [Tan91] M. Tanaka et al., *RCNP annual report* (1991).

- 
- [Tor14] T. G. Tornyi, M. Guttormsen, T. K. Eriksen, A. Gorgen, F. Giacoppo, T. W. Hagen, A. Krasznahorkay, A. C. Larsen, T. Renstrom, S. J. Rose, S. Siem, and G. M. Tveten, *Phys. Rev. C* **89** (2014) 044323.
- [Tua68] S. Tuan, L. Wright, and D. Onley, *Nuclear Instruments and Methods* **60** (1968) 70 .
- [Ube71] H. Uberall, *Electron Scattering from Complex Nuclei, Part A+B* (1971).
- [Vre] D. Vretenar, private communication.
- [Vri87] H. D. Vries, C. D. Jager, and C. D. Vries, *Atomic Data and Nuclear Data Tables* **36** (1987) 495 .
- [Wal78] T. Walcher, R. Frey, H.-D. Graf, E. Spamer, and H. Theissen, *Nuclear Instruments and Methods* **153** (1978) 17 .
- [Wal11] C. Walz, H. Fujita, A. Krugmann, P. von Neumann-Cosel, N. Pietralla, V. Y. Ponomarev, A. Scheikh-Obeid, and J. Wambach, *Phys. Rev. Lett.* **106** (2011).
- [Wig71] E. P. Wigner, *Group theory and its application to the quantum mechanics of atomic spectra / [by] Eugene P. Wigner ; translated from the German by J. J. Griffin*, Academic Press New York, expanded and improved ed. edition (1971).
- [Wim09] K. Wimmer, R. Krucken, V. Bildstein, K. Eppinger, R. Gernhauser, D. Habs, C. Hinke, T. Kroll, R. Lutter, H. Maier, P. Maierbeck, T. Morgan, O. Schaile, W. Schwerdtfeger, S. Schwertel, and P. G. Thirolf, *AIP Conference Proceedings* **1090** (2009) 539.
- [Win79] A. Winther and K. Alder, *Nucl. Phys. A* **319** (1979) 518.
- [Wol56] L. Wolfenstein, *Annu. Rev. Nucl. Sci.* **6** (1956) 43.
- [Woo99] J. Wood, E. Zganjar, C. De Coster, and K. Heyde, *Nuclear Physics A* **651** (1999) 323.
- [Wor94] H. Wortche, *Untersuchung der M1-Starkeverteilung in den schweren deformierten Kernen  $^{150}\text{Nd}$ ,  $^{154}\text{Sm}$ ,  $^{156}\text{Gd}$ ,  $^{232}\text{Th}$  und  $^{238}\text{U}$  mit unpolarisierter und polarisierter Protonenstreuung*, Doctoral thesis D17, TH Darmstadt (1994).
- [Yen54] D. R. Yennie, D. G. Ravenhall, and R. N. Wilson, *Phys. Rev.* **95** (1954) 500.
- [Yos95] M. Yosoi, H. Akimune, I. Daito, H. Fujiwara, S. Hirata, T. Inomata, O. Kamigaito, M. Kawabata, T. Noro, H. Sakaguchi, Y. Sakemi, T. Takahashi, A. Tamii, S. Toyama, A. Yamagoshi, and M. Yoshimura, *AIP Conf. Proc.* **343** (1995) 157.
- [Zaw90] D. Zawischa, M. Macfarlane, and J. Speth, *Phys. Rev. C* **42** (1990) 1461.
- [Zil91] A. Zilges, P. von Brentano, H. Friedrichs, R. Heil, U. Kneissl, S. Lindenstruth, H. Pitz, and C. Wesselborg, *Zeitschrift fur Physik A Hadrons and Nuclei* **340** (1991) 155.

---

## Danksagung

---

An dieser Stelle möchte ich ein herzliches Dankeschön an all diejenigen aussprechen, die mich bei der Anfertigung dieser Arbeit unterstützt haben und mir mit Rat und Tat beiseite standen.

Zuallererst danke ich Herrn Professor Dr. Dr. h.c. Norbert Pietralla für die Aufnahme in seiner Arbeitsgruppe und die Bereitstellung eines solch interessanten Forschungsthemas. Er hat den Fortschritt meiner Arbeit stets mit sehr großem Interesse verfolgt und seine Tür stand jederzeit offen für Ratschläge, Diskussionen und Fragen. Außerdem bin ich ihm dankbar für die Möglichkeit, Forschungsergebnisse auf interessanten Tagungen, Konferenzen und Workshops im In- und Ausland zu präsentieren. Die Gelegenheit und das Vertrauen, den *6<sup>th</sup> International Workshop on Shape-Phase Transitions and Critical-Point Phenomena in Nuclei* im Frühjahr 2012, an dem rund 100 Wissenschaftler teilnahmen, zu einem großen Teil selbst zu organisieren, hat mir sehr viel bedeutet. Hierbei habe ich sowohl fachlich sehr viel gelernt, als auch viele wertvolle Kontakte mit anderen Wissenschaftlern geknüpft von denen ich heute noch zehren kann und die mir in Zukunft sicher noch einiges ermöglichen.

Ein sehr großer Dank gebührt auch Herrn Professor Dr. Peter von Neumann-Cosel. Er ermöglichte mir die Arbeit an hochinteressanten Experimenten zur Protonenstreuung in Japan und Südafrika und unterstützte mich mit unglaublichem Zeitaufwand bei den Experimenten zur Elektronenstreuung am S-DALINAC und nicht zuletzt bei der Anfertigung dieser Arbeit. Auch über die unzähligen Diskussionen über alle Arten von physikalischen Fragestellungen bin ich ihm sehr dankbar.

I am deeply grateful to Professor Atsushi Tamii for the amazing help he offered during the experiments and also afterwards during the analysis procedure. He was always available for fruitful discussions.

Dankbar bin ich auch an die Kollegen vom Institut für die großartige Hilfe bei den Experimenten und insbesondere Herrn Florian Hug und seinem Team für die Bereitstellung eines exzellenten Elektronenstrahls für die Experimente.

A big 'thank you' goes to the accelerator group at RCNP in Osaka, who created excellent experimental conditions and also to all helpers who participated in the E350 experiment.

I am indebted to Vladimir Ponomarev for providing theoretical support for all kinds of experiments that I have done.

Da ich während meiner gesamten Zeit als Doktorand in verschiedenen Büros gesessen habe, gilt mein Dank all den netten, hilfsbereiten Kollegen für eine tolle Zeit, unzählige Diskussionen über physikalische und nichtphysikalische Themen. Besonders hervorheben möchte ich in diesem Zusammenhang Simela Aslanidou, Sergej Bassauer, Jonny Birkhan, Anna Maria Krumbholz, Dirk Martin, Maxim Singer und Iryna Zweidinger.

---

Neben den Arbeitskollegen im Büro möchte ich mich aber auch für die besondere Hilfe bei allen anderen administrativen, finanziellen und technischen Angelegenheiten bedanken. Hier sind besonders zu erwähnen: Marco Brunken, Ursula von Dungen, Maria Helm, Uli Krebs, Catja Noll de Lopez, Oliver Möller, Carina Seeger, Giovanna Umberti.

Ein großer Dank geht auch an die Mitarbeiter der elektrischen und mechanischen Werkstatt unter der Leitung von Herrn Bonnes bzw. Herrn Häckl und Herrn Oppermann, deren kompetente und schnelle Hilfe mich oftmals gerettet haben.

Außerdem danke ich allen Mitgliedern der Arbeitsgruppe Pietralla, sowie der Spektrometergruppe für die allseits nette Arbeitsatmosphäre.

Für den sportlichen Ausgleich am Kickertisch, vor allem in den letzten Wochen der heißen Phase, danke ich Tobias Klaus und Ilja Homm.

Neben der Arbeit war es immer wieder wertvoll und wichtig gute Freunde zu haben. Darüber bin ich sehr glücklich und daher möchte ich all meinen Freunden hiermit meinen Dank aussprechen, die immer für mich da waren, wenn es mal nicht so wollte wie es sollte, aber natürlich auch wenn alles gut war.

Meiner Familie, insbesondere meinen Eltern, meiner Schwester und vor allem meiner Frau Kathi und meinen beiden Katern Teddy und Pauli bin ich zu allergrößtem Dank verpflichtet. Ihr habt mich moralisch unterstützt, mich immer wieder aufgefangen wenn ich am Boden war, habt Geduld und Verständnis gezeigt und habt euch mit mir gefreut wenn alles gut lief und seid einfach die allerbesten! Vielen Dank!!!

Diese Arbeit wurde gefördert durch die DFG im Rahmen des Sonderforschungsbereichs 634 und durch das Vorhaben NE 679/3-1.



---

## Lebenslauf von Andreas Krugmann

---

### Persönliches

---

Geburtsdatum 15.08.1983  
Geburtsort Heppenheim an der Bergstraße  
Eltern Rainer Krugmann und Christine Krugmann (geb. Plickat)  
Familienstand verheiratet mit Katharina Krugmann

---

### Bildungsweg

---

1990 - 1994 Konrad-Adenauer-Grundschule in Heppenheim  
1994 - 2003 Starkenburg Gymnasium Heppenheim  
2003 - 2004 Zivildienst am ZSP Bergstraße  
2004 - 2007 TU Darmstadt, Bachelorstudium  
2007 - 2008 TU Darmstadt, Masterstudium  
seit Oktober 2008 Wissenschaftlicher Mitarbeiter am Institut für Kernphysik  
der TU Darmstadt



---

## Eigene Publikationen

---

Im folgenden werden alle Publikationen aufgelistet, die im Rahmen dieser Dissertation entstanden sind und/oder an denen ich mitgewirkt habe. Sie sind in chronologisch sortiert, beginnend mit der neuesten Publikation.

- [1] A. Scheikh Obeid, S. Aslanidou, J. Birkhan, **A. Krugmann**, P. von Neumann-Cosel, N. Pietralla, I. Poltoratska, and V. Yu. Ponomarev, *Phys. Rev. C* **89** (2014), 037301.
- [2] N. Pietralla and **A. Krugmann**, Meeting reports. *Nucl. Phys. News* **23** (2013), 33–34.
- [3] A. Scheikh Obeid, O. Burda, M. Chernykh, **Krugmann, A.**, P. von Neumann-Cosel, N. Pietralla, I. Poltoratska, V. Yu. Ponomarev, and C. Walz, *Phys. Rev. C* **87** (2013), 014337.
- [4] **A. Krugmann**, D. Martin, P. von Neumann-Cosel, N. Pietralla, I. Poltoratska, A. Tamii, *EPJ Web of Conferences* **38** (2012), 11001.
- [5] N. Pietralla, C. Walz, V. Yu. Ponomarev, H. Fujita, **A. Krugmann**, P. von Neumann-Cosel, A. Scheikh-Obeid, and J. Wambach, *Journal of Physics: Conference Series* **366** (2012), 012037.
- [6] **A. Krugmann**, Z. P. Li, J. Meng, N. Pietralla, and D. Vretenar, *Journal of Physics G: Nuclear and Particle Physics* **38** (2011), 065102.
- [7] C. Walz, H. Fujita, **Krugmann, A.**, P. von Neumann-Cosel, N. Pietralla, V. Yu. Ponomarev, A. Scheikh-Obeid, and J. Wambach, *Phys. Rev. Lett.* **106** (2011), 062501.
- [8] A. M. Heilmann, P. von Neumann-Cosel, A. Tamil, T. Adachi, C. Bertulani, J. Carter, H. Fujita, Y. Fujita, K. Hatanaka, K. Hirota, O. H. Jin, T. Kawabata, **A. Krugmann**, H. Matsubara, E. Litvinova, R. Neveling, H. Okamura, B. Ozel-Tashenov, I. Poltoratska, V. Yu. Ponomarev, A. Richter, H. Sakaguchi, Y. Sakemi, Y. Sasamoto, Y. Shimizu, Y. Shimbara, F. D. Smit, T. Suzuki, Y. Tameshige, Y. Yasuda, M. Yosoi, and J. Zenihiro, *Journal of Physics: Conference Series* **312** (2011), 092029.
- [9] **A. Krugmann**, J. Bonnet, N. Pietralla, and R. V. Jolos, *Journal of Physics: Conference Series* **205** (2010), 012037.
- [10] A. Scheikh Obeid, O. Burda, M. Chernykh, **A. Krugmann**, P. von Neumann-Cosel, N. Pietralla, I. Poltoratska, V. Ponomarev, and C. Walz, *Journal of Physics: Conference Series* **205** (2010), 012040.

- 
- [11] J. Bonnet, **A. Krugmann**, J. Beller, N. Pietralla, and R. Jolos, *Phys. Rev. C* **79** (2009), 034307.
- [12] A. Scheikh-Obeid, O. Burda, M. Chernykh, **A. Krugmann**, O. Möller, P. von Neumann-Cosel, and N. Pietralla, *AIP Conference Proceedings* **1090** (2009), 607.
- [13] N. Pietralla, A. Costin, J. Bonnet, J. Beller, **A. Krugmann**, O. Möller, H. Ai, R. F. Casten, A. Heinz, E. A. McCutchan, J. Qian, V. Werner, G. Rainovski, and K. Dusling, *AIP Conference Proceedings* **1090** (2009), 524.

---

## **Eigenständigkeitserklärung**

---

Hiermit versichere ich, die vorliegende Dissertation ohne Hilfe Dritter nur mit den angegebenen Quellen und Hilfsmitteln angefertigt zu haben. Alle Stellen, die aus Quellen entnommen wurden, sind als solche kenntlich gemacht. Diese Arbeit hat in gleicher oder ähnlicher Form noch keiner Prüfungsbehörde vorgelegen.

Darmstadt, den 17. Juni 2014